
Doctoral Dissertations


Student Theses and Dissertations

Fall 2015

Selective laser sintering of bioactive glass scaffolds and their biological assessment for bone repair

Krishna C. R. Kolan

Follow this and additional works at: https://scholarsmine.mst.edu/doctoral_dissertations

 Part of the [Biomedical Engineering and Bioengineering Commons](#), and the [Mechanical Engineering Commons](#)

Department: Mechanical and Aerospace Engineering

Recommended Citation

Kolan, Krishna C. R., "Selective laser sintering of bioactive glass scaffolds and their biological assessment for bone repair" (2015). *Doctoral Dissertations*. 2451.

https://scholarsmine.mst.edu/doctoral_dissertations/2451

This thesis is brought to you by Scholars' Mine, a service of the Missouri S&T Library and Learning Resources. This work is protected by U. S. Copyright Law. Unauthorized use including reproduction for redistribution requires the permission of the copyright holder. For more information, please contact scholarsmine@mst.edu.

SELECTIVE LASER SINTERING OF BIOACTIVE GLASS SCAFFOLDS AND
THEIR BIOLOGICAL ASSESSMENT FOR BONE REPAIR

by

KRISHNA CHAITANYA REDDY KOLAN

A DISSERTATION

Presented to the Faculty of the Graduate School of the
MISSOURI UNIVERSITY OF SCIENCE AND TECHNOLOGY

In Partial Fulfillment of the Requirements for the Degree

DOCTOR OF PHILOSOPHY

in

MECHANICAL ENGINEERING

2015

Approved

Ming C. Leu, Advisor

Gregory E. Hilmas, Co-Advisor

K. Chandrashekhara

Yue-Wern Huang

PUBLICATION DISSERTATION OPTION

This dissertation has been prepared in the format of peer reviewed journals for eventual publication.

The first paper, “Effect of Material, Process Parameters, and Simulated Body Fluids on Mechanical Properties of 13-93 Bioactive Glass Scaffolds by Laser Sintering,” was published in the *Journal of the Mechanical Behavior of Biomedical Materials*, and consumes pages 16 to 50.

The second paper, “Effect of Porosity and Pore Geometry of Laser Sintered Bioactive Glass Scaffolds on Mechanical Properties,” was written for publication in the *Journal of the Mechanical Behavior of Biomedical Materials*, and consumes pages 51 to 76.

The third paper, “In Vitro Assessment of Laser Sintered Bioactive Glass Scaffolds with Different Pore Geometries,” was published in the *Rapid Prototyping Journal*, and consumes pages 77 to 100.

The balance of this dissertation follows the standard dissertation format. The work presented in Section 2 which consumes pages 101 to 114 will be used as a part of future publication.

ABSTRACT

Bone scaffold fabrication using powder-bed based additive manufacturing techniques, like the selective laser sintering (SLS) process, provides control over pore interconnectivity, pore geometry, and the overall shape of the scaffold, which aids in repairing different regions of the bone. The main objectives of this dissertation were to develop bioactive glass (BG) scaffolds using the SLS process and evaluate the scaffolds for their effectiveness in bone repair both *in vitro* and *in vivo*. 13-93 glass, a silicate based BG, and 13-93B3 glass, a borate based BG, are designed to accelerate the body's natural ability to heal itself and are used in this research. After the initial feasibility study, the material and process parameters were optimized to improve the compressive strength from ~20 MPa to ~41 MPa, for a 13-93 BG scaffold with a porosity of ~50%.

Pore geometry of the scaffold plays a crucial role as it not only affects the mechanical properties and subsequent degradation but also the bone cell proliferation. Scaffolds with a porosity of ~50% and five different pore geometries, namely, cubic, spherical, X, diamond, and gyroid, were fabricated and assessed *in vitro* for a possible preferential cell proliferation. The MTT labeling experiments indicated that the scaffolds with diamond and gyroid pore geometries have higher curvature-driven MLO-A5 cell proliferation. Finally, scaffolds with diamond and cubic pore geometries were evaluated *in vivo* using a rat calvarial defect model for 6 weeks. Though the results indicated no significant difference in the amount of new bone formation with respect to the defect region, the maturation of the fibrous tissue to bone appeared to be quicker in the scaffolds with diamond architecture.

ACKNOWLEDGMENTS

Firstly, I would like to thank my advisor, Dr. Ming C. Leu, for providing me with the opportunity to work on this project. I am grateful to him for his patience and guidance throughout my graduate study. I truly admire his hard work and enthusiasm towards research which inspired me to pursue a career as a researcher. Further, I thank the National Science Foundation (NSF), Office of Naval Research (ONR), University of Missouri Interdisciplinary Intercampus Research Program, and Intelligent Systems Center (ISC) at Missouri S&T for providing financial support at various stages of my graduate study.

I would like to thank Dr. Gregory E. Hilmas for his helpful discussions and constructive suggestions during my graduate study. Special thanks to Dr. Roger F. Brown and Dr. Yue-Wern Huang for their assistance and guidance during the *in vitro* and *in vivo* work. I would also like to thank Dr. K. Chandrashekhara for helpful suggestions and serving on my committee.

I would like to acknowledge all current and past graduate students from VRAM laboratory, and especially, Amir Ghazanfari and Praneeth Isanaka for our productive discussions and all the help over the years. I also thank Wei Xiao and Shankar Pakkuru for their help during the animal experiments.

A special thanks to my friends Sharat, Ramakrishna, Santosh, and Karteek for their support and encouragement all these years. Finally, I would like to dedicate this work to my parents, Bal Reddy and Sharada, my brother, Rashmith and my sister, Sravya, for their emotional support and unconditional love and sacrifices.

TABLE OF CONTENTS

PUBLICATION DISSERTATION OPTION	iii
ABSTRACT.....	iv
ACKNOWLEDGMENTS	v
LIST OF ILLUSTRATIONS.....	x
LIST OF TABLES.....	xiii
 SECTION	
1. INTRODUCTION	1
1.1. MOTIVATION AND BACKGROUND.....	1
1.2. BIOACTIVE GLASSES FOR BONE REPAIR.....	3
1.3. ROLE OF ADDITIVE MANUFACTURING.....	4
1.4. SELECTIVE LASER SINTERING PROCESS.....	7
1.5. FEASIBILITY STUDY	8
1.6. PURPOSE OF DISSERTATION.....	10
REFERENCES	12
 PAPER	
I. EFFECT OF MATERIAL, PROCESS PARAMETERS, AND SIMULATED BODY FLUIDS ON MECHANICAL PROPERTIES OF 13-93 BIOACTIVE GLASS POROUS CONSTRUCTS MADE BY SELECTIVE LASER SINTERING	16
ABSTRACT	16
1. INTRODUCTION	18
2. MATERIALS AND METHODS.....	22
2.1. PREPARATION OF POWDER.....	22
2.2. SELECTIVE LASER SINTERING.....	23

2.3.	FABRICATION AND POST-PROCESSING	24
2.4.	IN VITRO ASSESSMENT	25
3.	RESULTS	27
3.1.	FEEDSTOCK CHARACTERIZATION FOR THE SLS PROCESS	27
3.2.	EFFECT OF PARTICLE SIZE AND BINDER CONTENT	27
3.3.	EFFECT OF HEATING RATES	29
3.4.	EFFECT OF SLS PARAMETERS	29
3.5.	SBF TESTS	31
4.	DISCUSSION	33
5.	CONCLUSIONS.....	40
	ACKNOWLEDGEMENTS	40
	REFERENCES.....	47
II.	EFFECT OF POROSITY AND PORE GEOMETRY OF LASER SINTERED BIOACTIVE GLASS SCAFFOLDS ON MECHANICAL PROPERTIES.....	51
	ABSTRACT	51
1.	INTRODUCTION	52
2.	MATERIALS AND METHODS	55
2.1.	FABRICATION OF SCAFFOLDS.....	55
2.2.	POST-PROCESSING AND PHYSICAL ASSESSMENT OF SCAFFOLDS.....	55
2.3.	SBF TESTS	56
3.	RESULTS	57
3.1.	EFFECT OF FABRICATION AND SINTERING ON POROSITY.....	57
3.2.	EFFECT OF POROSITY AND PORE GEOMETRY ON MECHANICAL STRENGTH.....	58

3.3. EFFECT OF SBF IMMERSION ON MECHANICAL STRENGTH	59
4. DISCUSSION	60
5. CONCLUSIONS.....	68
ACKNOWLEDGEMENTS	68
REFERENCES.....	74
III. <i>IN VITRO</i> ASSESSMENT OF LASER SINTERED BIOACTIVE GLASS SCAFFOLDS WITH DIFFERENT PORE GEOMETRIES	
ABSTRACT	77
1. INTRODUCTION	79
2. MATERIALS AND METHODS	82
2.1. FABRICATION OF SCAFFOLDS.....	82
2.2. CELL PROLIFERATION TESTS	83
2.3. STATISTICAL ANALYSIS	84
3. RESULTS AND DISCUSSION	85
3.1. DESIGN AND FABRICATION OF 13-93 AND 13-93B3 SCAFFOLDS..	85
3.2. CELL PROLIFERATION ON 13-93 SCAFFOLDS	85
3.3. CELL PROLIFERATION ON 13-93B3 SCAFFOLDS.....	87
3.4. EFFECT OF PORE GEOMETRY ON CELL PROLIFERATION	89
4. CONCLUSIONS.....	93
REFERENCES.....	98
SECTION	
2. <i>IN VIVO</i> EVALUATION OF LASER SINTERED BORATE BIOACTIVE GLASS SCAFFOLDS WITH CUBIC AND DIAMOND PORE GEOMETRIES ..	
2.1. INTRODUCTION.....	101
2.2. EXPERIMENTS	103

2.2.1. Scaffold Preparation.	103
2.2.2. Animals and Surgical Procedure.	104
2.2.3. Histological Processing.	106
2.2.4. Histomorphometric Analysis.	107
2.2.5. Statistical Analysis.	107
2.3. RESULTS AND DISCUSSION.....	107
2.3.1. New Bone Formation.....	107
2.3.2. Fibrous Tissue Formation.	111
2.4. CONCLUSIONS.....	112
REFERENCES.....	113
3. CONCLUSIONS.....	115
4. RECOMMENDATIONS FOR FUTURE WORK.....	117
VITA.....	119

LIST OF ILLUSTRATIONS

Figure	Page
1.1. The principle of Selective Laser Sintering (SLS) and the DTM 2000 machine.....	8
1.2. (a) SEM image of the 13-93 bioactive glass particles after ball milling with the stearic acid binder, (b) Green part fabricated with the established SLS process parameters, (c) MTT labeling of MLO-A5 cells on the scaffolds.	9
 PAPER I	
1. (a) CAD models of porous and hollow scaffold, (b) Fabricated ‘green’ scaffolds: porous, hollow and solid (from left to right).	41
2. Particle size distributions for powders with different binder contents.	42
3. (a) TGA curves of powders with different amounts of stearic acid binder by weight percentage, (b) Sintered porous scaffolds made with B22, B18, B15 and B12 powders (from left to right).	42
4. Variation of compressive strength for different heating rates during: (a) de-binding and (b) sintering for the parts made with B22 powder.	42
5. Effect of laser power and beam speed on the compressive strength of parts fabricated at the energy density of 1 cal/cm ²	43
6. Variation of compressive strength of the samples immersed in the SBF.	43
7. (a) surface morphology of SLS scaffold after immersion in SBF for 3 weeks, (b) magnified image showing surface cracks and ‘cauliflower’ like morphology, (c) high magnification image showing needle-like HA crystal formations.	44
8. XRD patterns: (a) reference hydroxyapatite (JCPDS 72-1243), (b) scaffold after 3 weeks of immersion in the SBF, (c) as-sintered scaffold representing a typical amorphous pattern of a silicate based 13-93 glass.	44
9. SEM images showing the effect of de-binding heating rates on microstructures of 13-93 bioactive scaffolds: (a) 0.5°C/min, (b) 1°C/min, and (c) 1.5°C/min.	45
10. Degree of SA melting under the laser beam at different <i>EDs</i> . Higher <i>ED</i> resulted in increased outer contour dimensions and greater depths in melt pool.	45

11. Effect of SLS parameters on the sharpness of features: (a) Fabricated green parts measuring 1 cm x 1 cm x 1 mm in dimensions. The numbers on the parts indicate the laser beam speed (*BS*) in mm/s, (b) Porous parts with the same design but fabricated at different energy densities. 46
12. SEM images of the fractured surfaces: (a & b) green part fabricated at $P = 3W$, $ED = 1 \text{ cal/cm}^2$ and the corresponding sintered part, (c & d) green part fabricated at $P = 5W$, $ED = 1 \text{ cal/cm}^2$ and the corresponding sintered part. 46

PAPER II

1. (a) CAD models of the repeatable units of five architectures: (i) cubic, (ii) spherical, (iii) X, (iv) diamond, and (v) gyroid; (b) 13-93B3 scaffolds with different architectures after sintering; (c) Diamond architecture scaffolds at four different porosities..... 70
2. Compressive strengths for 13-93B3 scaffolds with five different pore geometries and at different porosities. Vertical and horizontal error bars represent the SD of the measured compressive strength and porosities, respectively. 71
3. A comparison of the reduction in compressive strengths of scaffolds with different pore geometries and porosities after immersion in SBF for 7 days. 71
4. SEM images of a scaffold after immersion in SBF for 7 days: (a) outer surface morphology, (b) fracture surface of the scaffold indicating the reacted glass (RG) on the outer surface and unconverted glass (G), (c) higher magnification image of RG showing HA-like rounded crystal formations on the surface of the scaffold..... 72
5. Normalized cross-sectional area vs. Z value graphs for the unit cells at different porosities. 72
6. Compressive strength (MPa) vs. Porosity fraction of scaffolds with different pore geometries fitted with exponential functions (all with R^2 value of 0.98 and above). 73
7. Percentage reduction in compressive strength of a scaffold vs. ratio of total surface area (SA) offered by the scaffold in its cubic volume space. 73

PAPER III

1. (a) CAD models of the repeatable units of five architectures: (i) cubic, (ii) spherical, (iii) X, (iv) diamond, and (v) gyroid; (b) 13-93B3 scaffolds produced from the five different architectures, after sintering. 94

2.	(a) Schematic of the static cell seeding on the scaffold with at least two rows of repeating units. The cell seeded scaffolds were later transferred to a 12-well cell culture plate, (b) Optical images showing the MTT labeling of MLO-A5 cells on the scaffolds (L-R: cubic, spherical, X, gyroid and diamond) after cell culture intervals of 4 days (top row) and 6 days (bottom row).	95
3.	The absorbance values representing the measurement of cell growth plotted for all the scaffolds after 2, 4, and 6 days of incubation. Diamond and gyroid architectures show better overall cell proliferation compared to the other architectures.	95
4.	Comparison of the absorbance values for 13-93 and 13-93B3 scaffolds after 4 and 6 days of incubation. The graphs indicate the reduced number of metabolically active cells on the 13-93B3 scaffolds compared to the 13-93 scaffolds.	96
5.	(a) The surface of the strut exhibiting layered fabrication in the SLS process, (b) a typical surface of the SLS scaffold, (c) schematic showing the proliferation of cells on the rough surface during the initial incubation period.	96
6.	The variation of the perimeter through the length of the unit cell.	97
7.	The curvature plots of the perimeter ratio vs. z-value graphs for different architectures and the summation of the absolute values of the curvature.	97

SECTION

2.1.	Cubic and Diamond scaffold types (top and side views) and their CAD models	104
2.2.	(a) Optical image of the specimen cut from the harvested specimen, (b) after von Kossa staining of the specimen, (c) after H&E staining of the specimen; also shown in inset are the magnified images of the (i) new bone formed within the scaffold, and (ii) at the boundary of the defect region; N – new bone, O – original bone, G – glass, F – fibrous tissue which is about to mature. Percentage of new bone growth w.r.t. the defect area in cubic and diamond scaffold types is shown in the graph.	109
2.3.	H&E stained sections of (a) Diamond scaffold, and (b) Cubic scaffold. The inset figures show almost matured fibrous tissue (about to become bone) in the defect area implanted with a diamond scaffold.	112

LIST OF TABLES

Table	Page
PAPER I	
1. Powder characterization.....	41
2. Effect of particle size and binder content on compressive strength of the parts fabricated at 3W laser power and an energy density of 1 cal/cm ²	41
PAPER II	
1. Compositions (in wt.%) of 13-93 and 13-93B3 glasses compared to 45S5 glass.....	69
2. Differences in porosities: designed in CAD vs. measured after sintering.	69
3. Pore sizes of the sintered scaffolds at various porosities.....	70
PAPER III	
1. Compositions (in wt.%) of 13-93 and 13-93B3 glasses compared to 45S5 glass.....	94
SECTION	
2.1. Compositions (in wt.%) of 13-93 and 13-93B3 glasses in comparison to 45S5 glass.	102
2.2. Experimental plan showing scaffold placement in rat calvarial defect.	105
2.3. New bone area (in %) with respect to defect area measured from H&E stained sections for cubic and diamond scaffolds.....	110

1. INTRODUCTION

1.1. MOTIVATION AND BACKGROUND

The skeletal system in any vertebrate, including humans, provides the framework and protects the body by enclosing vital organs such as heart, brain, etc. and even formation of blood cells in the marrow. Therefore, health of bones is critical for human longevity. Bones are traditionally classified into long bones, short bones, flat bones, and irregular bones representing the entire human body. Long bones such as femur and humerus are considered load bearing bones and are more likely candidates for instances such as fracture. It is statistically reported that the growth of bone tissue peaks when we reach the age of thirty, approximately, and then bone mass deteriorates as we continuously age because of several reasons including a sedentary life style [1]. For an average healthy person, bone has a natural tendency to heal by itself, adapting its mass, shape, and to the mechanical requirements of the defect site. But, surgery becomes unavoidable in the case of a major accident.

A typical load bearing bone (femur or humerus) has an outer cortical (compact) bone and inner trabecular (spongy) bone. The cortical bone is responsible for providing the required strength, protection and shape to the skeleton whereas the trabecular bone acts as a reservoir and transports the required nutrients, and helps in formation of bone marrow, red blood cells, etc. The compressive strength of a human cortical bone ranges from 130 – 200 MPa and that of trabecular bone ranges from 2 – 12 MPa [2]. Therefore, to stabilize bone fracture and accelerate healing, metallic implants were the natural choice because of their mechanical properties. The disadvantages of using metallic implants, such as infections, damage to good bone, and accumulation of metals in tissues

led to the research of alternative materials. The discovery of Bioglass by Prof. Hench led to the development of several bioactive glasses as a replacement for metals [3]. The main intention of the research, and producing such glasses, was to develop a material which not only bonds with the surrounding tissue when implanted, but also actively aids in new tissue growth.

There are few synthetic bioactive bone grafts currently available in the market in the form of flexible strips and paste. However, they are limited to non-load bearing bone repairs [4]. Manufacturing a bioactive graft which has mechanical properties comparable to a load bearing bone, an anatomically accurate shape with required porosity, pore interconnectivity and pore geometry is a challenging task. Several traditional manufacturing methods, such as polymer foam replication, sol-gel casting, etc., are used to fabricate scaffolds for bone repair applications [5-9]. Additive manufacturing (AM) technologies utilize a layer-by-layer manufacturing approach which provides flexibility to fabricate complex shapes and thus have an edge over the traditional methods in terms of controlling the shape, porosity and pore size of the scaffolds. AM techniques can also be used to tailor-make synthetic grafts with specific geometric requirements for a particular bone defect site. Though there are some AM machines which can manufacture grafts out of titanium and titanium based alloys, there are no commercial machines which can directly fabricate ceramic parts. The goal of this research is to adapt the existing AM technique known as the selective laser sintering (SLS) process, otherwise utilized for polymer part fabrication, to develop bioactive glass scaffolds for bone repair. A couple of recently announced media reports (at the time of writing this dissertation), Micron 3DP and Massachusetts Institute of Technology's Mediated Matter Group independently

showed 3D printing of glass, seemingly at elevated temperatures, though technical details are yet to be reported.

1.2. BIOACTIVE GLASSES FOR BONE REPAIR

In the past, biomaterials were only bio-inert and lacked the ability to initiate an active response from the surrounding tissue to bond with the scaffold and to simultaneously support tissue regeneration and gene activation [3]. The discovery of 45S5 glass, popularly known as Bioglass®, by Prof. Hench in 1969 has spurred an active research interest in the field of bioactive glasses in the past four decades [3]. When exposed to body fluids, the bioactive glasses convert to hydroxyapatite (HA), which is the main mineral constituent of bone, thereby integrating with the surrounding bone tissue. Their mechanical properties, including compressive strength and elastic modulus, are comparable to those of human bone, making them potential candidates for tissue engineering.

Amorphous bioactive glasses offer excellent bioactive characteristics and form HA when exposed to body fluid for several hours to even days, depending on the glass composition [10]. However, one important concern of using bioactive glass is the scaffolds' degradation rate post implantation. The mechanical properties of the scaffolds will be maintained if the rate of new tissue regeneration complements the rate of degradation. A silicate-based glass converts to HA, but the rate of degradation tends to slow drastically after a threshold, leaving unconverted glass in the host body. Several other elements like zinc, boron, copper, and strontium, etc. are also used to dope the bioactive glasses to initiate different responses with the surrounding tissue to that effect [11]. For example, doping a bioactive glass with strontium has been shown to enhance

osteoblast cell growth, and differentiation, thereby having positive effects in bone repair [12]. Also, addition of such elements could influence the rate of degradation of the bioactive glasses. Borate-based glasses degrade much faster (in few hours) in comparison to silicate-based glasses (several months) and are found to bond with both soft and hard tissues [13]. The release of boron ions could have a toxic effect on cell growth during *in vitro* conditions; however, research has found no such effect when implanted *in vivo* and when dynamic culture conditions are used *in vitro* [14-16]. However, the focus of this research is not to develop new glasses but to utilize the existing bioactive glasses and develop approaches to manufacture implants in such a way that they can be utilized to treat load-bearing and non-load-bearing bone defects. Both, silicate and borate bioactive glasses have been used in this research for the investigations.

1.3. ROLE OF ADDITIVE MANUFACTURING

The adoption of additive manufacturing (AM) technology has been advancing at a rapid pace in recent years, especially in the field of biomedical science and engineering, as it offers better control over pore size, pore interconnectivity, and shape and geometry of the implant. For the purpose of manufacturing biomedical implants, AM processes can be broadly classified into (a) photo-curable liquid resin based (e.g., laser stereolithography (STL)), (b) powder bed based (e.g., electron beam melting (EBM) and selective laser sintering (SLS)), and (c) extrusion based (e.g., freeze-form extrusion fabrication (FEF), fused deposition modeling (FDM) and Robocasting). STL, SLS and FDM are generally used to fabricate parts from polymer materials including PCL, PLGA, and PLA which have relatively low degradation rates (one year and longer) [17-22]. The EBM process uses an electron beam in a vacuum chamber to melt the particles and

produce metallic implants with titanium (Ti) or Ti-based alloys [23, 24]. Though Ti based implants are not brittle like bioceramics, they are only biocompatible and not bioresorbable. Research is still being carried out to directly manufacture parts with ceramics or glasses using AM processes due to several process and material related limitations [25, 26]. Therefore, it can be stated that none of the existing AM processes have been used to successfully manufacture bioactive implants directly without having to go through post-processing steps, and only indirect approaches have been adopted to manufacture bioceramic parts.

In the extrusion based AM processes, ceramic material is formed into pastes/inks by means of adding water and other additives which is then extruded from a nozzle in a controlled fashion like a filament and then deposited over a platform. Some of the extrusion-based processes which were investigated to fabricate bioceramic parts for biomedical applications include Robocasting, Direct Ink Writing, and Freeze-form Extrusion Fabrication using bioceramics like HA, β -TCP, and BG. Though the basic concept of fabrication remains the same, there are minor differences in the fabrication of parts using these processes. In Robocasting, deposition of the paste is carried out on a heated plate to dry the paste so as to deposit the next layer [27]. In DIW, a specialized ink is prepared with the bioceramic particles and the ink is deposited on a substrate which is immersed in heated non-wetting oil so that the deposited filaments would have sufficient mechanical integrity before post-processing in a furnace [28-30]. In the FEF process, the entire machine is enclosed in a freezing environment so that the deposited filament is solidified before deposition of the next layer [31]. The parts made by extrusion-based processes tend to have higher densities (~95%) in comparison to parts made with powder

bed based AM processes (~75-80%) [32]. Therefore, extrusion based AM processes provide superior mechanical properties to the scaffolds comparable to cortical bone (~130 MPa), and hence they are preferred over the powder bed based processes and could potentially be useful to repair load-bearing bones. However, fabricating porous constructs with complex pore geometries is a challenging task for extrusion based AM processes.

Powder-bed based AM processes used to manufacture bioceramic scaffolds include the SLS process (DTM Sinterstation, 3D Systems Ltd.) and 3D printing (Z Corp 3D Printer, ZPrinting) [33]. In ZPrinting, consolidation occurs when an ink-jet like printing head moves across a powder bed selectively depositing a liquid binding material based on the cross-sectional area. A Z Corp 3D printer was used to fabricate β -tricalcium phosphate (TCP) scaffolds by a couple of research groups but the mechanical properties achieved were in the range of ~2 to 5 MPa, which is the lower limit of the compressive strength of trabecular bone [34, 35]. Though porous scaffolds can be manufactured in such a manner, difficulties have existed in fabricating complex shaped implants with finer pore resolution, in the range of ~100 to ~500 μm . In the SLS process, consolidation of powder particles occurs when a laser beam selectively heats the powder bed to melt the polymeric particles. Both the processes were used to fabricate porous scaffolds in the early 2000's, albeit with a different approach. A polymeric mold was first fabricated and then filled with HA particles followed by polymer burnout and sintering the HA particles [36, 37]. Other approaches to fabricate porous scaffolds using the SLS process include mixing a polymeric binder in relatively large quantities (~50% by volume) to fabricate glass-ceramic implants, and later burning out the binder to create uncontrolled porosity in the scaffolds [38]. Though the SLS process has been used to fabricate biopolymer

scaffolds, manufacturing bioactive glass scaffolds remains largely unexplored. Some of the challenges involved in fabricating scaffolds using a bioactive glass include the crystallization of the glass upon laser interaction, the kind of binder to be used, and difficulties in controlling the porosity, and pore sizes, of the scaffolds. The initial feasibility studies indicated that although glass cannot be fabricated directly without using a binder, the amorphous nature of the glass will not be affected when using low energy density during the consolidation of the particles on the powder bed [39].

1.4. SELECTIVE LASER SINTERING PROCESS

The working principle of SLS is use of a computer controlled laser beam to scan and melt a thermoplastic powder in the cross-sectional area based on a single layer of a computer-aided design (CAD) model. After one layer is finished, according to the computer generated slice pattern from a CAD model, the second layer begins, thereby fabricating a three dimensional part. A schematic diagram showing the inside chamber of the SLS machine is shown in Figure 1.1. Several limitations have been reported by researchers over the years while using ceramics instead of polymers during the fabrication process [39]. Therefore, an indirect fabrication method was employed in this study to establish a feasible set of SLS parameters conducive to fabricating scaffolds from bioactive glasses. In this method, a polymeric binder is mixed with the 13-93 glass powder to help fuse the powder particles during fabrication. Several process parameters including laser power, beam speed, beam spacing, particle size, layer thickness, powder bed and part bed temperatures, are investigated at this stage for efficient fabrication of scaffolds. The fabricated scaffolds are then post processed to burn out the binder and then sinter the 13-93 glass particles to obtain the eventual scaffold.

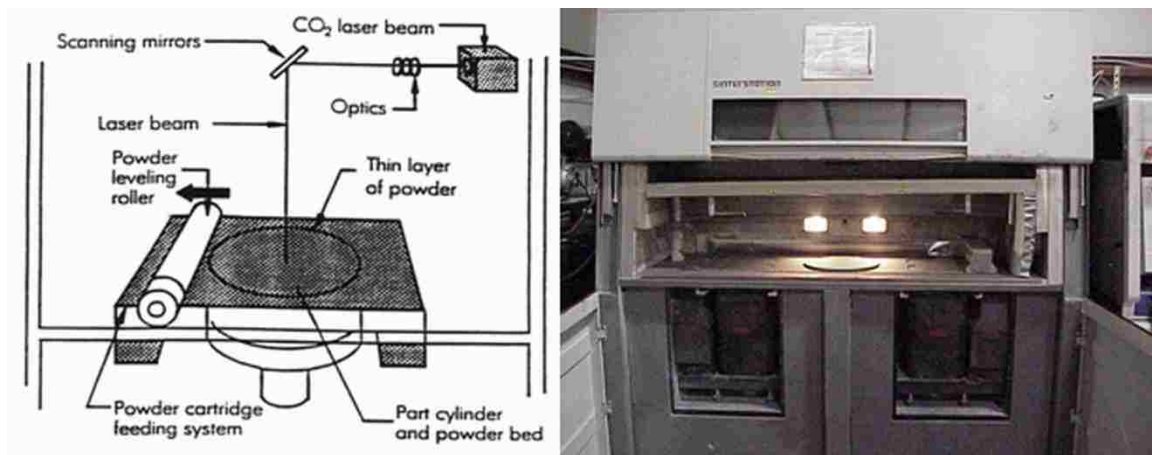


Figure 1.1. The principle of Selective Laser Sintering (SLS) and the DTM 2000 machine.

1.5. FEASIBILITY STUDY

The feasibility of fabricating a synthetic bone scaffold with designed porosity using 13-93 bioactive glass was investigated. Stearic acid, a waxy solid and fatty acid in the form of flakes, was mixed with the bioactive glass powder to aid during the fabrication process as a binder. Figure 1.2.(a) shows an SEM image of the bioactive glass particles covered by the smaller stearic acid particles. Process parameters like the laser power, scan speed, scan spacing, energy density, powder bed temperature, and layer thickness were identified based on the degree of melting of the binder and binding of successive layers in two separate sets of experiments. After finalizing the process parameters, a cylindrical shaped porous scaffold (10 mm in diameter and 20 mm in length) with a designed porosity of ~70% was successfully fabricated (shown in Figure 1.2.(b)). The fabricated scaffold was post-processed by placing it in a furnace and heating at a controlled rate to remove the binder and sinter the glass particles. The sintering

schedule was developed based on thermogravimetric analysis of the feedstock powder (bioactive glass+binder). The average compressive strength of the sintered scaffolds was 20.4 MPa, which is excellent for non-load bearing applications. The scaffolds were then cut into discs with a thickness of ~2 mm for *in vitro* assessment. MLO-A5 (mouse late osteoblasts early osteocyte) cells were used to confirm the feasibility of the scaffolds to support cell attachment and proliferation. An optical image of cell-seeded SLS scaffolds incubated with MTT during the last 4 hours of incubations of 2, 4, and 6 days is shown in Figure 1.2.(c). The relative intensity of purple formazan staining on these scaffolds increased directly (and dramatically after 6 days in comparison to commercially available bioresorbable 3D phosphate scaffolds) with the duration of incubation, an indication of metabolically active cells undergoing vigorous growth on the SLS scaffolds. Therefore, the results of the feasibility study have demonstrated successful use of the 13-93 glass to fabricate bone scaffolds for tissue engineering purposes using the indirect SLS process. The surface roughness, pore size and compressive strength achieved along with the vigorous cell growth on the scaffolds established the potential of SLS process for human trabecular bone repair.

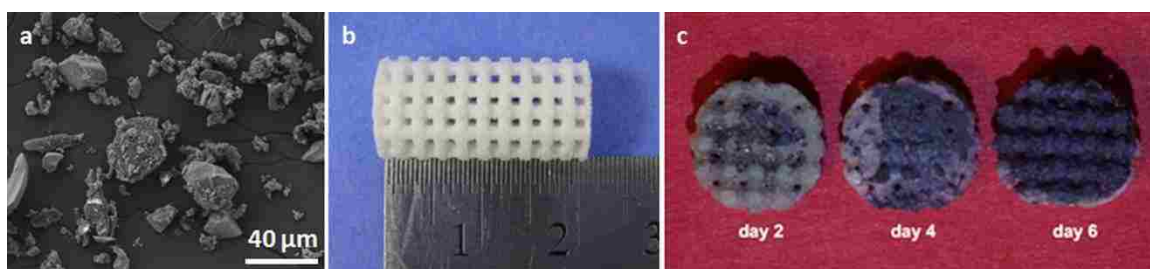


Figure 1.2. (a) SEM image of the 13-93 bioactive glass particles after ball milling with the stearic acid binder, (b) Green part fabricated with the established SLS process parameters, (c) MTT labeling of MLO-A5 cells on the scaffolds.

1.6. PURPOSE OF DISSERTATION

The purpose of this dissertation was to fabricate bioactive glass scaffolds for bone repair using the SLS process. Though the fabrication of porous ceramic parts with the SLS process has been explored in a couple of different approaches in the past, a thorough investigation of the fabrication parameters has not been performed. The first section of this dissertation focuses on systematic investigation of the effect of material and SLS process parameters. In the present work, an indirect method of fabricating scaffolds with designed porosity and interconnected pores was developed using the SLS process. The results obtained from the experimental investigation of the material and process parameters are broadly applicable to fabricating parts with any kind of ceramic/glass materials using the SLS process.

Porosity and pore geometry of the scaffold are two most important parameters in bone tissue repair and regeneration applications. With the advent of additive manufacturing technologies, the current breed of advanced machines should provide a tremendous opportunity to investigate the effects of scaffold pore geometry on mechanical properties and biological behavior *in vivo*. Unfortunately, researchers focusing on bioceramic scaffolds have utilized extrusion based 3D printers which have a limited functionality in investigating the effects of pore geometry on bone formation. On the other hand, researchers working on powder-bed based 3D printers have focused on either metal or polymer part fabrication for biomedical applications. The second section of this dissertation uses the silicate and borate based bioactive glasses to fabricate scaffolds with five different architectures and evaluate their mechanical and degradation properties.

The third and fourth sections of this dissertation work deal with the biological evaluation of the scaffolds fabricated using the SLS process and with different pore geometries. The effect of pore shape on cell proliferation and tissue growth has been receiving some attention lately and there have been some conflicting reports on the effects of pore geometry on new tissue growth in the literature. It is interesting to note here that most of the results are based on either polymer or metal scaffolds which re-emphasizes the mentioned fact on the focus of researchers working on powder-bed based 3D printers. *In vitro* assessment of scaffolds with five different pore geometries with an established osteoblastic cell-line has been performed and the MTT assay was used to measure the cell proliferation. Two architectures were selected based on the *in vitro* assessment results for further investigation of bone formation *in vivo* using a rat calvarial defect model. Histological evaluations were performed on the harvested samples along with the adjacent tissue to measure the new bone formation and evaluate the significance of pore geometry.

REFERENCES

1. Jee WSS, 2001. Integrated bone tissue physiology: Anatomy and physiology. In: Cowin SC (Ed.), *Bone Mechanics Handbook*, CRC Press, New York, pp. 1-50.
2. Carter DR and Hayes WC, 1976. Bone compressive strength: the influence of density and strain rate. *Science* 194:1174-76.
3. Hench LL, 2006. The story of bioglass. *J Mater Sci: Mater Med.* 17:967-978.
4. <https://www.stryker.com/en-us/products/Orthobiologicals/BoneRepair/Vitoss/index.htm#> Last accessed on 5/4/2014.
5. Rainer A, Giannitelli SM, Abbruzzese F, Traversa E, Licoccia S, Trombetta M, 2008. Fabrication of bioactive glass-ceramic foams mimicking human bone portions for regenerative medicine. *Acta Biomater.* 4:362-369.
6. Chen QZ, Thompson ID, Boccaccini AR, 2006. 45S5 Bioglass®-derived glass-ceramic scaffolds for bone tissue engineering. *Biomaterials.* 27:2414-2425.
7. Fu Q, Rahaman MN, Bal BS, Brown RF, D Day DE, 2008. Mechanical and in vitro performance of 13-93 bioactive glass scaffolds prepared by a polymer foam replication technique. *Acta Biomater.* 4:1854-1864.
8. Liu X, Rahaman MN, Fu Q, 2011. Oriented bioactive glass (13-93) scaffolds with controllable pore size by unidirectional freezing of camphene based suspensions: microstructure and mechanical response. *Acta Biomater.* 7:406-416.
9. Chen B, Zhang Z, Zhang J, Dong M, Jiang D, 2006. Aqueous gel-casting of hydroxyapatite *Mater Sci Eng A.* 435:198-203.
10. Hench LL, Anderson O, 1993. Bioactive glasses. In: Hench LL, Wilson J (Eds.), *An Introduction to Bioceramics*, vol. 1. World Scientific Publishing Co. Pte. Ltd., Singapore, pp. 41-62.
11. Rahaman M, Day D, Bal B, Fu Q, Jung S, Bonewald L, Tomsia A, 2011. Bioactive glass in tissue engineering. *Acta Biomater.* 7:2355-73.
12. Isaac J, Nohra J, Lao J, Jallot E, Nedelec JM, Berdal A, Sautier JM, 2011. Effects of strontium-doped bioactive glass on the differentiation of cultured osteogenic cells. *Eur Cell Mater.* 21:130-143.
13. Jung SB, 2010. Borate based bioactive glass scaffolds for hard and soft tissue engineering. PhD thesis, Missouri S&T, Rolla, MO.

14. Fu Q, Rahaman MN, Fu H, Liu X, 2010. Silicate, borosilicate, and borate bioactive glass scaffolds with controllable degradation rate for bone tissue engineering applications. I. Preparation and *in vitro* degradation. *J. Biomed. Mater. Res.* 95A:164-171.
15. Fu Q, Rahaman MN, Bal BS, Bonewald LF, Kuroki K, Brown RF, 2010. Silicate, borosilicate, and borate bioactive glass scaffolds with controllable degradation rate for bone tissue engineering applications. II. *In vitro* and *in vivo* biological evaluation. *J. Biomed. Mater. Res.* 95A:172-179.
16. Lin Y, 2012. *In Vivo* Evaluation of Microfibrous Bioactive Borate Glasses for Use in Wound Healing. MS thesis, Missouri S&T, Rolla, MO.
17. Hutmacher D, Schantz T, Zein I, Ng K, Teoh S, Tan K, 2001. Mechanical properties and cell cultural response of polycaprolactone scaffolds designed and fabricated via fused deposition modeling. *J Biomed Mater Res.* 55:203-216.
18. Matsuda T, Mizutani T, 2002. Liquid acrylate-endcapped biodegradable poly(ϵ -caprolactone-co-trimethylene carbonate) II computer-aided stereolithographic microarchitectural surface photo constructs. *J Biomed Mater Res.* 62:395-403.
19. Williams J, Das S, 2005. Bone tissue engineering using polycaprolactone scaffolds fabricated via selective laser sintering. *Biomaterials.* 26:4817-27.
20. Shor L, Guceri S, Chang R, Sun W, Gordon J, Kang Q, Hartstock L, An Y, 2009. Precision extruding deposition (PED) fabrication of polycaprolactone (PCL) scaffolds for bone tissue engineering. *Biofabrication.* 1:015003.
21. Melchels F, Feijen J, Grijpma D, 2009. A poly(D,L-lactide) resin for the preparation of tissue engineering scaffolds by stereolithography. *Biomaterials.* 30:3801-09.
22. Cooke M, Fisher J, Dean D, Rimnac C, Mikos A, 2003. Use of stereolithography to manufacture critical-sized 3D biodegradable scaffolds for bone ingrowth. *J Biomed Mater Res.* 64B:65-69.
23. Heintl P, Muller L, Korner C, Singer R, Muller F, 2008. Cellular Ti-6Al-4V structures with interconnected macro porosity for bone implants fabricated by selective electron beam melting. *Acta Biomater.* 4:1536-44.
24. <http://www.arcam.com/technology/electron-beam-melting/materials/> Last accessed on 4/20/2014.
25. Bartolo P, Kruth J, Silva J, Levy G, Malshe A, Rajurkar M, Mitsuishi M, Ciurana J, Leu M, 2012. Biomedical production of implants by additive electro-chemical and physical processes. *CIRP Ann-Manuf Techn.* 61(2):635-655.

26. Yves H, Wilkes J, Wilhelm M, Konrad W, Reinhart P, 2010. Net shaped high performance oxide ceramic parts by selective laser melting. *Physics Procedia*. 5:587-594.
27. Cesarano III J, Dellinger JG, Saavedra MP, Gill DD, 2005. Customization of load-bearing hydroxyapatite lattice scaffolds. *Int. J. Appl. Ceram. Technol.* 2:212-220.
28. Lewis J, Smay J, Stuecker J, Cesarano III J, 2006. Direct ink writing of three-dimensional ceramic structures. *J Am Ceram Soc* 89:3599–3609.
29. Fu Q, Saiz E, Tomsia A, 2011. Direct ink writing of highly porous and strong glass scaffolds for load-bearing bone defects repair and regeneration. *Acta Biomater.* 7:3547-54.
30. Liu X, Rahaman M, Hilmas G, Bal B, 2013. Mechanical properties of bioactive glass (13-93) scaffolds fabricated by robotic deposition for structural bone repair. *Acta Biomater.* 9(6):7025-34.
31. Doiphode N, Huang T, Leu M, Rahaman M, Day D, 2011. Freeze extrusion fabrication of 13-93 bioactive glass scaffolds for bone repair. *J Mater Sci: Mater Med.* 22:515–523.
32. Kolan KCR, Doiphode ND, Leu MC, 2010. Selective laser sintering and freeze extrusion fabrication of scaffolds for bone repair using 13-93 bioactive glass: A comparison. In: *Proceedings of the Solid Freeform Fabrication Symposium*. Austin, TX. 876-883.
33. <http://www.3dsystems.com/3d-printers/production/overview>. Last accessed on 5/4/2014.
34. Fielding GA, Bandyopadhyay A, Bose S, 2012. Effects of silica and zinc oxide doping on mechanical and biological properties of 3D printed tricalcium phosphate tissue engineering scaffolds. *Dent Mater.* 28(2):113-22.
35. Vorndran E, Klammert U, Klarner M, Grover LM, Barralet JE, Gbureck U, 2009. 3D printing of β -tricalcium phosphate ceramics. *Dent Mater.* 25(5):e18-e19.
36. Chu TMG, Halloran JW, Hollister SJ, Feinberg SE, 2001. Hydroxyapatite implants with designed internal architecture. *J Mater. Sci.: Mater. Med.* 12:471-478.
37. Bose S, Suguira S, Bandyopadhyay A, 1999. Processing of controlled porosity ceramic structures via fused deposition. *Scripta Materialia*. 41:1009–1014.
38. Goodridge RD, Dalgarno KW, Wood DJ, 2006. Indirect selective laser sintering of an apatite–mullite glass-ceramic for potential use in bone replacement applications. *Proc Inst Mech Eng H.* 220:57-68.

39. Kolan KCR, Leu MC, Hilmas GE, Velez M, 2010. Selective laser sintering of 13-93 bioactive glass. In: Proceedings of the Solid Freeform Fabrication Symposium. Austin, TX. 504-512.

PAPER**I. EFFECT OF MATERIAL, PROCESS PARAMETERS, AND SIMULATED BODY FLUIDS ON MECHANICAL PROPERTIES OF 13-93 BIOACTIVE GLASS POROUS CONSTRUCTS MADE BY SELECTIVE LASER SINTERING**

Krishna C. R. Kolan^a, Ming C. Leu^a, Gregory E. Hilmas^b, Mariano Velez^c

^a Department of Mechanical and Aerospace Engineering, Missouri University of Science and Technology, Rolla, MO 65409, USA

^b Department of Materials Science and Engineering, Missouri University of Science and Technology, Rolla, MO 65409, USA

^c Mo-Sci Corporation, Rolla, MO 65401, USA

ABSTRACT

The effect of particle size distribution, binder content, processing parameters, and sintering schedule on the microstructure and mechanical properties of porous constructs was investigated. The porous constructs were produced by indirect selective laser sintering (SLS) of 13-93 bioactive glass using stearic acid as a polymeric binder. The binder content and d_{50} particle size in the feedstock powders were simultaneously reduced from 22 to 12 weight percent and from 20 μm to 11 μm , respectively, to identify the minimum binder content required for the SLS fabrication. An average particle size of $\sim 16 \mu\text{m}$ with a binder content of 15 weight percent significantly reduced post-processing time and improved mechanical properties. Increasing the laser power and scan speed at the energy density of 1 cal/cm^2 maintained the feature sharpness of the parts during the fabrication of green parts and could almost double the mechanical properties of the sintered parts. Changes in the heating rates, ranging from 0.1 to 2 $^{\circ}\text{C/min}$, during the post-processing of the fabricated “green” scaffolds showed that the heating rate

significantly affects the densification and mechanical properties of the sintered scaffolds. The compressive strength of the scaffolds manufactured with the optimized parameters varied from 41 MPa, for a scaffold with a porosity of ~50%, to 157 MPa, for a dense part. The bioactive scaffolds soaked in simulated body fluids for durations up to 6 weeks were used to evaluate the change in mechanical properties *in vitro*.

Keywords: Selective laser sintering; Bioactive glass; Porous constructs; Scaffolds; Simulated body fluids.

1. INTRODUCTION

Scaffolds manufactured using synthetic polymers are mostly bio-inert and do not initiate an active response from the surrounding tissue to bond with the bone by providing appropriate mechanical strength and simultaneously supporting tissue regeneration and gene activation. 45S5 glass, developed by Hench L.L. in 1969 and popularly known as Bioglass®, was the first glass reported to chemically bond with bone (Hench and Anderson, 1993). Since then, several compositions have been developed based on this original formulation. The actively researched bioactive materials can be broadly divided into glasses, glass-ceramics and crystalline ceramics. Synthetic hydroxyapatite (HA) is a widely researched ceramic with interesting mechanical properties, but its main limitation lies in its slow resorption and conversion rates. The presence of a heat treatment controlled crystalline phase in glass-ceramic systems increases the mechanical properties of the scaffolds; however, it is reported that the presence of a crystalline phase could reduce the rate of mineralization after implantation (Rahaman et al., 2006). Alternatively, amorphous glasses offer excellent bioactive characteristics and an advanced ability to form an HA layer when exposed to body fluids from a few hours to several days, depending on their composition (Hench and Anderson, 1993). One of the major advantages of using the bioactive glass implants lies in the fact that they support vascularization and enzyme activity apart from adhesion, growth and differentiation of osteoblasts. It was reported by other researchers that during the conversion of the bioactive glasses to HA, the dissolution products play a key role in gene activation leading to greater tissue in-growth when compared to pure HA. (Rahaman et al., 2011; Rezwan et al., 2006). 13-93 glass, a silicate based bioactive glass, is used in our present

research work to prepare scaffolds intended for bone repair. A higher amount of SiO₂ content in 13-93 glass, compared to 45S5 glass, could slow down the reaction rates upon implantation. However, promising compressive strengths and elastic modulus values for 13-93 makes it a potential candidate for bone scaffolds, particularly for compressive load-bearing applications.

Several fabrication techniques have been used to manufacture porous bioactive scaffolds in non-load-bearing and recently, load-bearing applications. Scaffolds manufactured using a more traditional method such as foam replication, have shown an ability to mimic the trabecular bone architecture. However, these scaffolds have limitations in shape as well as their application in load-bearing bone repairs (Fu et al., 2008). The additive manufacturing (AM) techniques have an advantage of being able to tailor the shape and internal architecture of the scaffolds, providing an alternative approach for such biomedical applications (Kruth et al., 1998). The two AM methods that are widely used for bone tissue engineering are: (i) extrusion based, including Robocasting, Direct Ink Writing (DIW) and Freeze-form Extrusion Fabrication (FEF) (Cesarano et al., 2005; Doiphode et al., 2011; Fu et al., 2011; Lewis et al., 2006) and (ii) powder bed based, including Selective Laser Sintering (SLS), Selective Laser Melting (SLM) and 3D printing (3DP) (Goodridge et al., 2006; Liu et al., 2010; Marchelli et al., 2010; Seitz et al., 2005; Xiao et al., 2008; Kolan et al., 2011). Porous scaffolds made using extrusion based methods generally show higher compressive strength because of the smaller particle size used in the paste and the layer-by-layer deposition approach used to build the parts (Huang et al., 2011). However, fabricating scaffolds with internal

trabecular type architecture and an externally complex 3D shape would be relatively difficult with such processes.

SLS processes have not received much attention in direct processing of bioceramics, because of high sintering temperatures of ceramics and machine limitations in processing such materials (Kruth et al., 2003). Therefore, an indirect approach is generally adopted, wherein a binder is either used to fabricate a negative mold of the required porous structure or is mixed with the ceramic material to provide a feedstock for the machine. The feasibility of fabricating designed porosity scaffolds with 13-93 bioactive glass using indirect SLS process with stearic acid (SA) as the binder was reported in our previous work (Kolan et al., 2010). The scaffolds, after fabrication but before binder burnout, are generally called “green” scaffolds. Post processing of these green scaffolds becomes crucial for biomedical applications because the binder should be completely removed from the sintered scaffolds. Also, high density should be achieved in the supporting struts of the scaffolds to improve their mechanical properties. Some of the important parameters that need to be considered for the fabrication of functional scaffolds using such methods include the particle size of the starting material, the type and amount of binder, the SLS processing parameters, and the de-binding and sintering processes.

There are reports available in the literature regarding the SLS processing of ceramics with different particle sizes and using different thermoplastics as sacrificial binders (Goodridge et al., 2006; Kruth et al., 2003; Leu et al., 2008; Liu et al., 2007; Liu et al., 2010; Subramanian et al., 1995; Wolhert and Bourell, 1996). However, there is no previous report that show how to reduce the binder content and particle size together with a consideration towards fabrication and post-processing issues. The effect of varying SLS

process parameters has been studied for over a decade on fabrication of dense parts (Gibson and Shi, 1997). However, the effect of parameters for fabrication of porous parts, such as for biomedical applications, using a sacrificial binder has not been explored. The theory of de-binding has been researched for over two decades with results reporting the effects of parameters like the type of binder used, particle size, porosity and heating rate on the overall de-binding time (German, 1987; Lei et al., 2006; Lewis, 1997; Pinwill et al., 1992). Some models were also proposed to calculate the time required for de-binding process (Lombardo and Feng, 2003). However, several aspects, including the wide range of particle sizes used in the feedstock powder and the complexity of the parts made using the SLS process, make it difficult to use such models to determine the heating rate and time taken during the post-processing stage. In our work described in the present paper, we have used an experimental approach to investigate the effects of particle size distribution used in the SLS process during the fabrication of “green” porous constructs and their subsequent heat treatment in order to improve the densification of the sintered scaffolds.

2. MATERIALS AND METHODS

The four-pronged approach adopted in this work includes: (i) to prepare the feedstock powder with different particle size distributions and binder content, (ii) fabricate porous parts using the SLS process with the feedstock powders prepared so as to understand the effect of SLS parameters, (iii) post-processing of the green parts, i.e., binder burnout and sintering, to understand the effects of different heating rates on the sintered scaffolds and (iv) immersion of the sintered scaffolds in simulated body fluids to measure the variation of the compressive strength as a function of time *in vitro*.

2.1. PREPARATION OF POWDER

13-93 bioactive glass (Mo-Sci Corp., Rolla, MO) with a nominal chemical composition of 53% SiO₂, 4% P₂O₅, 20% CaO, 5% MgO, 6% Na₂O and 12% K₂O (in weight percentage) was used in this research. The details of the 13-93 glass preparation are available elsewhere in the literature (Kolan et al., 2011). Two sets of 13-93 glass particles were prepared before mixing with the stearic acid (SA) as binder (C₁₈H₃₆O₂, grade HS, Acros Organics, Morris Plains, NJ). The first set had a d₅₀ (50% of particles smaller than the indicated size) particle size of ~44 μm and the second set had a d₅₀ of ~0.7 μm. The first set of 13-93 glass particles were mixed with SA and dry ball-milled for 8 hrs with ZrO₂ grinding media to obtain the feedstock powder for the SLS machine. The feedstock composition consisted of 22% binder content in weight (hereafter referred to as B22). Then, a calculated amount of 13-93 glass from the first set (d₅₀ ~44 μm) was added to the B22 powder and dry ball-milled overnight to obtain the B18 powder. A similar procedure was then used to prepare the B15 powder from the B18 powder. However, reducing the d₅₀ particle size from 16 μm to 10 μm turned out to be time

consuming by dry ball-milling process because of several kilos of feedstock as required for the machine operation. Therefore, a pre ball-milled 13-93 glass powder (~0.7 μm) was added to B15 powder and ball-milled to obtain B12 powder. This served two purposes: (i) It reduced the overall particle size of the feedstock after only a few hours of ball-milling and (ii) It helped in determining the effect of sub-micron particles during the fabrication and post-processing stages as explained in Sections 3.2 and 3.3. All the calculations were based on the bulk densities of the powders (13-93 glass – 2.66 g/cc; stearic acid – 0.84 g/cc). Particle size distributions were obtained using a laser diffraction-based particle size analyzer (S3500, Microtrac Inc., Largo, FL). All the powders were examined by a differential thermal analysis (DTA) machine (Netzsch STA 409, Burlington, MA) to determine the heating rates and hold times during the post-processing stage.

2.2. SELECTIVE LASER SINTERING

The SLS fabrication experiments were carried out on a commercial DTM Sinterstation 2000 machine. The major SLS process parameters, namely, laser power, beam speed and scan spacing, determine the amount of heat input per unit area, i.e., energy density, on the part bed during the fabrication process. The above parameters are related in the formula: $ED = P/(BS * SS)$; where ED – Energy Density, P - Laser Power, BS - Beam Speed, and SS - Scan Spacing (Nelson, 1993). The feasible set of parameters conducive to fabricating scaffolds using the B22 powder has already been established in our previous studies (Kolan et al., 2011). The SS parameter was maintained at 0.23 mm, which corresponds to 50% overlap of the laser beam diameter (~0.46 mm) of the SLS machine, throughout the experiments. All the parts in the current work were fabricated

using a layer thickness of 76.2 μm . The part bed and part heater temperatures were maintained at 60°C, which is slightly below the melting point of SA (~69°C). This helps melt the SA at low laser powers and avoids unnecessary temperature gradients in the powder bed. The feed bin temperature was maintained at 35°C. An initial set of experiments was planned each time a powder with reduced binder content (B18, B15 or B12) was used as a feedstock to the SLS machine. The experiments included fabricating parts measuring 1 cm x 1 cm x 1 mm to aid in determining the behavior of the powder, and the appropriate SLS control parameters, while being scanned by the laser beam. The 1 mm thick parts were visually inspected for delaminations, and the workable SLS parameter settings were determined based on the best feature definitions of the 1 mm thick parts. The effects of SLS parameters are presented in Section 3.4 and discussed in Section 4.

2.3. FABRICATION AND POST-PROCESSING

Siemens NX commercial software was used to prepare the CAD models of the scaffolds with dimensions of 6 mm in length and 5 mm in radius. Figure 1(a) shows the CAD models of the porous scaffold (~60% porosity) and the hollow scaffold (wall thickness of 1.1 mm and 4 symmetric holes measuring 1.2 mm in diameter). The CAD file is then converted to an STL file recognizable by the software of DTM Sinterstation which then slices the file into many layers based on the input layer thickness. Figure 1(b) shows the representative green scaffolds fabricated using the B22 powder and the SLS machine. Hereafter, these scaffolds will be referred to as porous, hollow and solid scaffolds (as shown from left to right respectively, in Figure 1(b)). The fabricated green parts were post-processed in a three-stage programmable air furnace (Vulcan Benchtop

Furnace, York, PA). The average shrinkage values of ~20% in length and ~14% in diameter were observed among all the parts after sintering, which are similar to what we obtained in our previous study (Kolan et al., 2011). A crosshead speed of 0.5 mm/min was used on a mechanical load frame (Instron 4469 UTM, Norwood, MA) to determine the compressive strength of the sintered parts. The compressive strengths were calculated using the maximum amount of load carried by a sample divided by its cross-sectional area. Five samples in each set were used, and the results are reported as the average value and standard deviation. Scanning electron microscopy (SEM) (S-570, Hitachi Co., Tokyo, Japan) images of the sintered parts were obtained to analyze the micrographs of the fractured specimens.

2.4. IN VITRO ASSESSMENT

The sintered scaffolds were cleaned three times (3 minutes each) using distilled water followed by cleaning three times (3 minutes each) with pure ethanol using an ultrasonic cleaner (Crest CP 500T, Trenton, NJ). The scaffolds were then dried in an oven maintained at 65°C overnight. The samples were weighed and then kept in a simulated body fluid (SBF), which was prepared based on the Kokubo method [Kokubo and Takadama, 2006], where 100 ml of solution was used for every gram of scaffold. The SBF container with test scaffolds was kept in an incubator maintained at 37°C. The scaffolds were removed from the SBF and then dried in air before determining the crystalline nature of the material. Thin-film X-ray diffraction analysis (XRD) (Philips X-Pert, Westborough, MA) at a scanning rate of 1.8°/min in the 2 θ range from 10° to 70° using Cu K α radiation ($\lambda = 0.154056$ nm) was performed to analyze for the formation of a crystalline phase. The scaffolds were sputter-coated with Au/Pd and examined under

SEM (S-4700 FESEM, Hitachi Co., Tokyo, Japan) to observe the morphology of the surface.

3. RESULTS

3.1. FEEDSTOCK CHARACTERIZATION FOR THE SLS PROCESS

The particle size distribution for all the powders used in the study is shown in Figure 2 with reducing weight percentage of binder. A batch containing 22 wt.% of stearic acid binder was used in the B22 powder as a starting point, which was based on our previous study (Kolan et al., 2011). The increase in the overall particle size of B18 powder ($d_{30} \sim 12 \mu\text{m}$, $d_{95} \sim 96 \mu\text{m}$) when compared to B22 powder ($d_{30} \sim 9 \mu\text{m}$; $d_{95} \sim 66 \mu\text{m}$) is because of addition of 13-93 glass particles ($d_{50} \sim 44 \mu\text{m}$) to B22 powder to reduce the percentage of binder content. After overnight ball-milling, the distribution of B18 powder is similar to that of a bimodal distribution with broad peaks at $10 \mu\text{m}$ and $44 \mu\text{m}$ (Figure 2(b)). The preparation of the B15 from B18 powder involved addition of more 13-93 particles and ball-milling which gave a distribution as shown in Figure 2(c), which has a peak at $10 \mu\text{m}$ and a significant amount of particles greater than $20 \mu\text{m}$. 13-93 glass particles with an average particle size of $\sim 0.7 \mu\text{m}$ were added to the B15 powder and then dry ball-milled overnight to obtain the B12 powder. The B12 particle size distribution showed 30% of the particles less than $5 \mu\text{m}$ and 70% of the particles less than $20 \mu\text{m}$ (Figure 2(d)). The four different wt.% of the binder content of the powders and their d_{30} , d_{50} , d_{80} and d_{95} particle sizes are listed in Table 1.

3.2. EFFECT OF PARTICLE SIZE AND BINDER CONTENT

Figure 3(a) shows the TGA results of feedstock powders prepared with different amounts of stearic acid binder. The TGA curves show little or no weight change until about 250°C followed by rapid weight loss over much smaller temperature ranges (within next 100°C to 200°C), which is typical of thermoplastic binders (Lewis, 1997). As the

amount of binder content is reduced, the TGA curve shifts towards typical first-order binder decomposition (Jaw et al., 2001; Lombardo and Feng, 2003). The TGA curves for 22 wt.% and 18 wt.% do not follow a first-order decomposition trend, thus there is a requirement for longer heat treatment schedules with slower heating rates and longer hold times to carefully remove the binder without damaging the scaffolds. Figure 3(a) seems to suggest that 12 wt.% of stearic acid binder may be the best based on its simpler TGA curve, but the 12% binder was found to be insufficient to fabricate workable green parts because of the smaller particle size distribution for the B12 powder. The green scaffolds fabricated using B12 powders lacked sufficient strength to remove the unsintered powder from the pores. There was a low yield of about 20% during the fabrication for B12 parts, i.e., only 2 out of 10 parts fabricated could be successfully removed and cleaned from the part bed of the machine. Figure 3(b) shows representative porous scaffolds sintered at 700°C for 1 hr. The grey appearance of the B12 parts indicates the unsuccessful binder burnout and sintering of the parts. Therefore, further reduction of binder content was not considered and a minimum of 15 wt.% stearic acid was considered, as required for the SLS fabrication. The variation of compressive strengths of the porous, hollow and solid scaffolds made with the B22, B18 and B15 powders is shown in Table 2. Compressive strengths ranged from 18 to 22 MPa for the porous scaffolds, from 41 to 46 MPa for the hollow scaffolds and from 60 MPa to 115 MPa for the solid parts. As expected, increase in porosity resulted in a lower strength and the lowest binder content (B15) resulted in the highest compressive strengths for all of the three geometries.

3.3. EFFECT OF HEATING RATES

The heat treatment of the green scaffolds was completed in two phases: (i) a slower heating rate for de-binding the green scaffolds from room temperature to 550°C because the TGA results (Figure 3(a)) showed a complete decomposition of the stearic acid binder at ~550°C; (ii) a faster heating rate until reaching 700°C, with a 1 hour hold for sintering of the glass particles followed by a furnace cool to room temperature. The sintering temperature of 700°C was based on the glass transition temperature (~606°C) and the onset temperature of crystallization (~714°C) of the 13-93 glass (Fu et al., 2007). Two different sets of experiments were carried out to identify the best possible heating rates for the porous parts during de-binding and sintering phases. In the first set of experiments, the sintering heating rate was kept constant at 2°C/min, and the de-binding heating rate was varied from 0.5 to 2°C/min. In the second set of experiments, the effective de-binding heating rate of 1°C/min was chosen, and the sintering heating rate was varied from 2 to 16°C/min. Figure 4 graphically represents the variation of the compressive strengths of the sintered hollow scaffolds at different heating rates. The graphs indicate that the best possible heating rates for de-binding and sintering are 1°C/min and 4°C/min, respectively.

3.4. EFFECT OF SLS PARAMETERS

After determining the effects of heating rate, particle size and binder content, the scaffolds made with B15 powder were found to have the highest compressive strength and the least post-processing time when compared to other powders (B22, B18 and B12). Therefore, B15 powder was used to study the effect of SLS parameters, namely, laser power (P), beam speed (BS) and energy density (ED). The problem of delamination

exists at low ED and our previous study established that a minimum ED of 1 cal/cm^2 is required to achieve the sufficient melting to fuse successive layers (Kolan et al., 2011). An increase in ED beyond 1 cal/cm^2 improves the densification in the fabricated green part but results in dimensional inaccuracies, which make the fabrication of porous parts with required porosities and pore sizes almost impossible using our SLS machine (more discussion on this in Section 4). Therefore, we maintained the ED at 1 cal/cm^2 and studied the effects of varying P and BS .

Figure 5 shows the increase in the compressive strengths of the porous, hollow and solid scaffolds fabricated at the ED of 1 cal/cm^2 with varying P of 3W, 4W and 5W and corresponding BS of 305, 406 and 508 mm/s. The compressive strength of the porous parts almost doubled, from 22 MPa to 41 MPa, when the laser power was increased from 3W to 5W. Similar trends can also be seen for the hollow and solid scaffolds with compressive strengths increasing to 61.4 MPa and 157 MPa, respectively. The compressive elastic modulus values, measured from the slope of the stress versus strain curves, for the porous, hollow and solid parts were $4.4 \pm 0.7 \text{ GPa}$, $6.1 \pm 1.6 \text{ GPa}$ and $12 \pm 1 \text{ GPa}$, respectively. The modulus and strength values of the porous parts are higher than the human trabecular bone values (strength: $\sim 2\text{-}12 \text{ MPa}$ and modulus: $< 1 \text{ GPa}$), but are less than that of a typical human cortical bone (strength: $\sim 130\text{-}200 \text{ MPa}$ and modulus: $\sim 12\text{-}18 \text{ GPa}$ and higher) (Carter and Hayes, 1976; Karageorgiou and Kaplan, 2005; Keaveny, 2000; Rezwan et al., 2006). The strength and modulus values of the solid parts lie in the lower range of a human cortical bone.

3.5. SBF TESTS

Compression tests conducted on scaffolds soaked in simulated body fluid (SBF) provided mechanical strength degradation data of the scaffolds, and the scaffold surface conversion to an HA layer, over different time periods. The variation of the compressive strengths after soaking the scaffolds in the SBF for 1 to 6 weeks is shown in Figure 6. Detailed discussion of the behavior of 13-93 glass and its degradation in SBF can be found elsewhere in the literature (Fu et al., 2010). The main objective of our work was to study the variation of mechanical properties of the 13-93 glass scaffolds made using the SLS process after immersion in SBF. The scaffolds used for this study were fabricated using the B22 powder with the SLS parameters of 3W laser power and 305 mm/s beam speed.

The compressive strength of the porous scaffolds measured after 6 weeks was 11 MPa, an approximately 38% reduction over the baseline compressive strength before SBF immersion. This value is at the higher end of the compressive strength of a human trabecular bone (~2-12 MPa) (Carter and Hayes, 1976). The formation of HA crystals within one week of the scaffolds' immersion in SBF was observed, which is in line with other reports of the *in vitro* behavior of 13-93 glass (Fu et al., 2007, 2008). Figure 7 shows SEM images of a representative scaffold taken out of the SBF after 3 weeks. Figure 7(a) depicts the typical rough surface morphology of an SLS scaffold being converted to a smooth surface with a thick crystalline layer after 3 weeks of immersion. Figure 7(b) is a magnified image of the scaffold showing the surface cracks and a typical 'cauliflower' morphology, which represents an HA like crystalline surface. Figure 7(c) is a high magnification image of the region indicated in Figure 7(b) showing nano-sized

needle-like HA formations. Figure 8 provides a comparison of the XRD patterns of the as-sintered 13-93 glass, after immersion in the SBF for 3 weeks, and the reference synthetic HA (JCPDS 72-1243). The matching crystalline peaks of the three-week SBF sample are identified in the reference XRD pattern.

4. DISCUSSION

The amount of binder required to mix with the 13-93 glass particles in preparation of feedstock powder is determined through empirical tests in our study. An increased amount of binder not only causes more shrinkage in the final part but also leads to difficulties during the post-processing stages like formation of voids during de-binding and incomplete densification after sintering, which weakens the final part. The scaffolds made for bone repair applications must have at least 50% porosity and pore sizes greater than 100 μm (recommended $>300 \mu\text{m}$) for tissue in-growth and at the same time be capable of carrying high compressive loads (130–200 MPa) for a load-bearing human bone (Carter and Hayes, 1976; Karageorgiou and Kaplan, 2005; Murphy et al., 2010). Our previous results indicate that the SLS process can achieve pores in the range 300–800 μm and a compressive strength of ~ 20 MPa for a scaffold with a designed porosity of $\sim 50\%$ (Kolan et al., 2011). The mechanical properties of the scaffolds can be improved by increasing the densification of the glass particles in the solid region of a designed porous scaffold. This requires determining the smallest amount of binder required for the SLS fabrication and it relates to the particle size. A smaller particle size requires a larger amount of binder because of a larger surface area of the glass particles that needs to be wetted by the melted thermoplastic binder. But it was reported that a very small particle size in the feedstock caused non-uniform spreading, leading to warpage and cracks in the part during the initial layers of the SLS fabrication (Goodridge et al., 2006; Leu et al., 2010). Powders of larger particle size are easier to handle and require lower binder content because of relatively smaller surface areas. On the other hand, in terms of mechanical properties, using large particles could lead to poor mechanical properties

because of relatively large grains formed in the microstructure after sintering even if a full density is achieved. Smaller particles ($\sim 3 \mu\text{m}$) result in a finer grain size after sintering and improved mechanical properties. Therefore, a balance must be made between the particle size and the amount of binder used in SLS fabrication. The approach adopted in our preparation of feedstock powder was to decrease the binder content and the particle size simultaneously, so as to achieve effective particle size and binder content with fewer experiments and less waste of powder feedstock. Our results showed the trends of varying particle size, binder content and SLS process parameters on fabrication and mechanical properties of porous parts, which could provide useful insight in the SLS processing of glasses and ceramics.

The heating rate is critical for post-processing the green scaffolds because a slower heating rate increases the overall time taken to manufacture a scaffold. This decreases the attractiveness of the SLS process, which typically has a very short build time (for example, it takes 30 minutes to fabricate parts shown in Figure 1, excluding time taken for machine set-up, warm-up and cool-down stages). Our results showed that the strength of scaffolds increased up to a certain heating rate and then decreased after that. To confirm this, scaffolds were made with different dimensions and layer thickness and a similar trend was observed on the effect of heating rate. Figure 9 shows SEM images of the fracture surfaces of these scaffolds processed at different de-binding heating rates. Figure 9(a) clearly shows the voids in the microstructure of the fractured strut of a representative sintered part obtained after a de-binding heating rate of $0.5^\circ\text{C}/\text{min}$. Figure 9(b) shows the microstructure obtained at a heating rate of $1^\circ\text{C}/\text{min}$. Availability of larger surface area in the porous part combined with a better oxidative

decomposition of the SA binder could be the reason that even a porous part could be heated at a rate of $1^{\circ}\text{C}/\text{min}$ during the binder burnout phase. However, a further increase in the heating rate to $1.5^{\circ}\text{C}/\text{min}$ would rapidly melt the SA binder (melting point $\sim 70^{\circ}\text{C}$), causing the porous part to collapse. Even if the part survives the de-binding stage, the faster heating rate may cause void formation in the microstructures. Figure 9(c) shows voids in the microstructure, probably caused by trapped gases because of limited binder decomposition when heated at $1.5^{\circ}\text{C}/\text{min}$ and above. Such a microstructure reduces the mechanical properties of the scaffolds. Hence the use of heating rate during the binder removal from the porous parts is critical in obtaining effective densification, which improves the mechanical properties of the scaffolds. In our case, the parts with a de-binding heating rate of $1^{\circ}\text{C}/\text{min}$ provided the highest compressive strength values.

Our results also indicated that the strength of the scaffolds depends on the rate of heating in the sintering stage. A slower sintering rate could crystallize the silicate based 13-93 bioactive glass, affecting its bioactivity upon implantation. On the other hand, a higher sintering rate increases the temperature at which the glass particles sinter, which could result in incomplete densification (Panda and Raj, 1989). Also, a higher sintering rate forms bigger grains which negatively affect the overall mechanical properties of the sintered scaffold (Rahaman, 2006). This resulted in lower compressive strengths at higher sintering rates ($>4^{\circ}\text{C}/\text{min}$) as well as a high standard deviation in the compressive strength for the scaffolds sintered at $16^{\circ}\text{C}/\text{min}$ in this study.

The presence of micro porosity in the green part could be detrimental to achieve proper densification during the sintering process. Therefore, it is important to have a compact green part with little or no micro porosity other than the designed porosity in the

CAD model during the fabrication. One method of improving the mechanical properties of the parts fabricated using the SLS process is by increasing the energy density (ED) (Caulfield et al., 2007). A higher ED results in complete melting of SA binder, which not only wets the ceramic particles and bonds them together but also fills the voids between the particles. This improves the density in the green part which in turn increases the mechanical properties of the sintered part after post-processing. In our case, to understand the extent of melting of the binder, SA was spread on the part bed and scanned using a laser beam at different ED values ranging from 0.3 to 2.5 cal/cm². Figure 10 shows the degree of SA melting at ED of 2.5 cal/cm² compared to 1 cal/cm². A larger amount of SA melting along with an increased depth of the melt pool was observed with the higher ED . This gives a more compact green part and improved mechanical properties. However, it was also observed that the dimensions of the wetted area after the laser scanning increased with increasing ED . Such an effect increases the dimensions of the green part when compared to its CAD model and might affect the fabrication of porous parts as explained below.

The dimensional accuracy of the fabricated parts using SLS depends on process parameters. Figure 11(a) shows the effect of varying SLS parameters in terms of laser power (P) and energy density (ED) on the fabrication of square parts measuring 1 cm x 1 cm x 1 mm in dimensions. The ED was increased from 1 to 3 cal/cm² at laser powers of 3W, 4W and 5W by maintaining the scan spacing at 0.23 mm. The parts fabricated at the ED of 1 cal/cm², which is the minimum amount required for effective bonding of successive layers, maintained their shape and dimensions as shown in Figure 11(a). The sharpness of the features was lost and the dimensions increased for the square parts as

they became more rounded with increasing ED by reducing the scanning speed at a constant laser power. This is believed due to melting of the binder adjacent to the part's outline profile through conductive heat transfer as the laser beam is moved relatively slowly. Such dimensional inaccuracies would greatly affect the fabrication of designed porous scaffolds as shown in Figure 11(b), which shows the same scaffold design fabricated at different energy densities with a higher ED for the scaffold above and a lower ED for the scaffold below. The adjacent binder particles in the above scaffold even though not scanned by the laser, would melt at a higher ED thereby decreasing the effective pore size in the green part. This reduces the porosity and pore size in the fabricated scaffold when compared with the designed scaffold and even causes difficulty in removing the unsintered powder particles. Such problems were not observed in the porous parts fabricated with a laser power of 5W and ED of 1 cal/cm².

Our results indicate that improved mechanical properties can also be achieved by increasing P and BS and maintaining a constant ED . The improvement in mechanical properties can be attributed to the higher power laser beam causing the binder in the previously scanned layers to re-melt and distribute itself into any voids that were initially present, contributing to a reduction in micro porosity in the green part. This also provides a more uniform distribution of the binder in the green parts, leading to a better oxidative decomposition of the SA binder during the de-binding stage and thereby improving densification. Figure 12(a) shows the fractured surface of a green part fabricated at 3W laser power. Voids measuring up to ~200 μm in size are indicated in the SEM image. Figure 12(b) shows the fracture surface of the part after sintering. The voids that were present in the green scaffold (Figure 12(a)) are as expected, still clearly visible after

sintering. In contrast, no presence of such large voids can be observed in Figure 12(c), which is the fracture surface of a green part fabricated at 5W laser power. Figure 12(d) shows an improved microstructure after sintering for the scaffold fabricated at 5W laser power. Smaller voids ($\sim 20 \mu\text{m}$) that are difficult to see in this case are indicated using pointers. This improved microstructure almost doubled the mechanical properties from $\sim 20 \text{ MPa}$ to $\sim 40 \text{ MPa}$ for the porous scaffold. A similar improvement in mechanical properties was also observed for hollow and dense parts as reported in the results shown in Figure 5. Therefore, increasing P and BS by maintaining ED at a required minimum value not only offers better fabrication results in terms of dimensional accuracies but also improves the mechanical properties of the fabricated parts.

To our knowledge, other reports on manufacturing porous constructs for biomedical applications using indirect SLS process were given by Goodridge et al. (2006) and Xiao et al. (2008). Glass-ceramic was used in their work, and the porosity was not designed in the CAD model but was achieved after burning out the binder from a solid part, which would not provide highly interconnected pores. Such a method is not feasible for bone in-growth in large defects. The results obtained using 13-93 bioactive glass in our current study should be beneficial in fabrication of porous parts with ceramics, glass-ceramics and other glass compositions using the indirect SLS method. Our previous *in vitro* assessment showed vigorous growth of MLO-A5 line of mouse late-osteoblast, early-osteocyte cells on 13-93 scaffolds made using the SLS process (Kolan et al., 2011). Recently, it was also reported that the *in vivo* evaluation of 13-93 SLS scaffolds in a rat segmental defect showed partial bridging in 3 weeks and full bridging after 6 weeks of implantation (Velez et al., 2011). The scaffolds used in the

above mentioned studies had a compressive strength of ~20 MPa for ~50% porosity.

Therefore, it can be stated that with improved mechanical properties (~41 MPa for ~50% porosity) achieved in the current study, the indirect SLS process has a great potential for manufacturing highly interconnected porous structures and load-bearing scaffolds for bone repair applications using bioactive glasses.

5. CONCLUSIONS

The particle size distribution with d_{50} particle size of $\sim 16 \mu\text{m}$ with 15 wt.% binder content (B15 powder) offered the best fabrication results with much reduced micro porosity in green scaffolds made from 13-93 bioactive glass in this study. Our SLS processing and post-processing results with B12 (12 wt.% binder) powder indicates that the presence of submicron sized particles not only requires a higher binder content but also causes difficulty in fabrication. A significant improvement in the mechanical properties, $\sim 85\%$ increase in compressive strength, was measured when increasing the laser power and beam speed from 3W and 305 mm/s to 5W and 508 mm/s at a constant energy density of 1 cal/cm^2 . The compressive strengths of the sintered scaffolds in our study varied from 41 MPa for a scaffold with $\sim 50\%$ porosity to 157 MPa for a dense part. The compressive strength of the scaffolds after immersion in the SBF for 6 weeks decreased by 38% but was still higher than that of a human trabecular bone. X-ray diffraction analysis and scanning electron microscopy showed the formation of a crystalline hydroxyapatite layer on the surface of the scaffolds. The improved mechanical properties combined with the promising *in vitro* results show the high potential of scaffolds manufactured with 13-93 bioactive glass using the selective laser sintering process in load-bearing applications for bone repair.

ACKNOWLEDGEMENTS

This research was funded by the Office of Naval Research with an SBIR Phase I award N00014-11-M-0113 to Mo-Sci Corporation and by the Intelligent Systems Center at Missouri University of Science and Technology. The authors thankfully acknowledge the technical assistance of Xin Liu and Kevin Wu during various stages of this work.

Table 1. Powder characterization.

Binder (wt.%)	d ₃₀ (μm)	d ₅₀ (μm)	d ₈₀ (μm)	d ₉₅ (μm)
22	9	16	32	66
18	12	20	49	96
15	10	16	39	79
12	5	11	28	56

Table 2. Effect of particle size and binder content on compressive strength of the parts fabricated at 3W laser power and an energy density of 1 cal/cm².

Binder content (Wt.%)	Porous (MPa)	Hollow (MPa)	Solid (MPa)
22	18.3±5.8	40.9±6	60.1±24.7
18	19.4±5.4	43.7±12.2	76.9±22.5
15	22.1±3.8	45.9±6.3	115±28.4

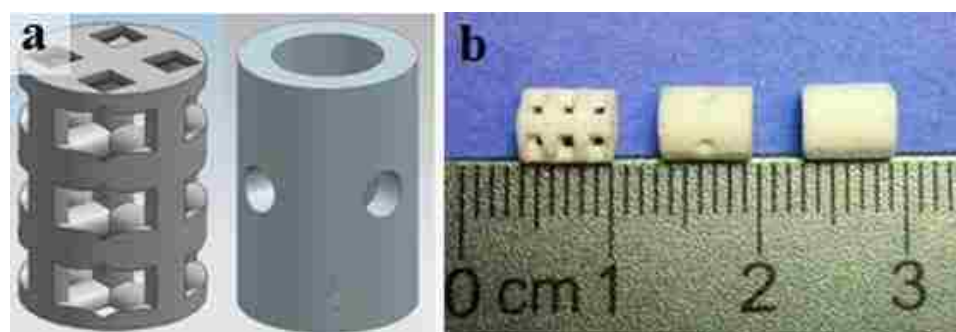


Figure 1. (a) CAD models of porous and hollow scaffold, (b) Fabricated 'green' scaffolds: porous, hollow and solid (from left to right).

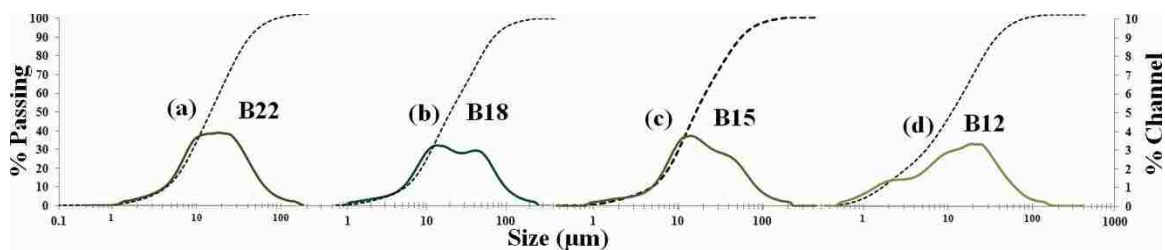


Figure 2. Particle size distributions for powders with different binder contents.

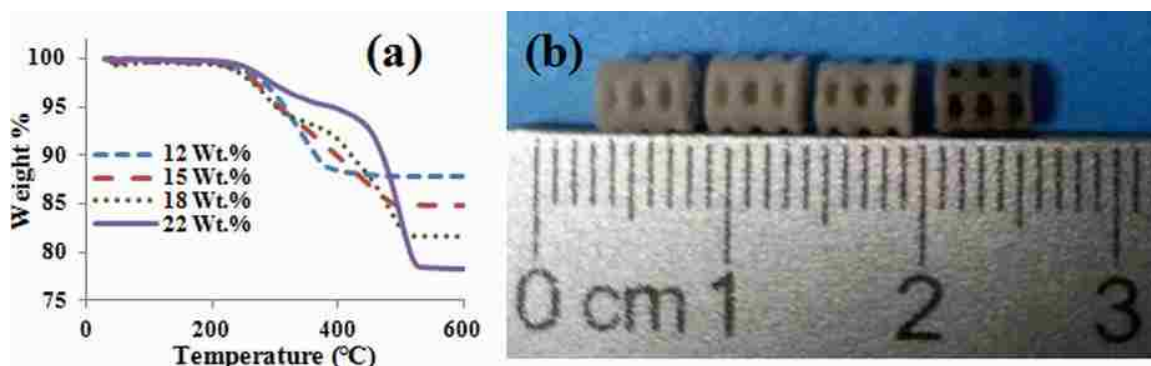


Figure 3. (a) TGA curves of powders with different amounts of stearic acid binder by weight percentage, (b) Sintered porous scaffolds made with B22, B18, B15 and B12 powders (from left to right).

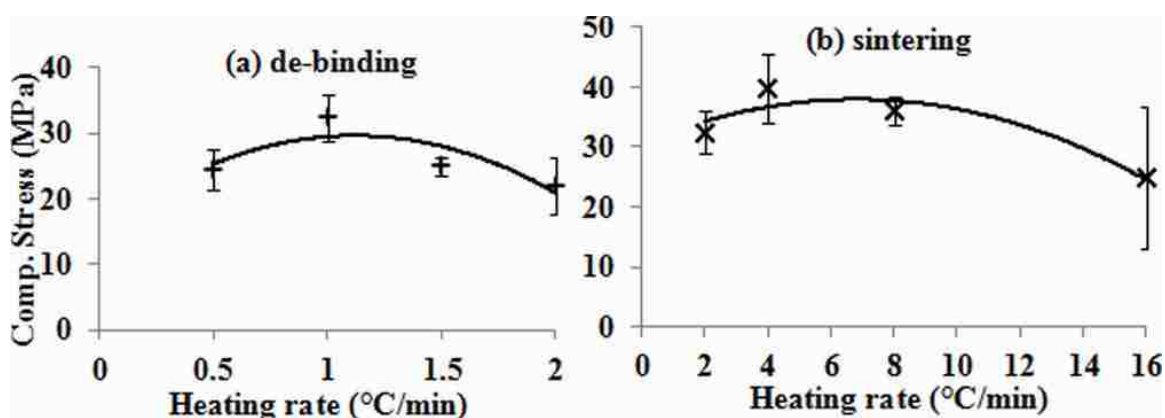


Figure 4. Variation of compressive strength for different heating rates during: (a) de-binding and (b) sintering for the parts made with B22 powder.

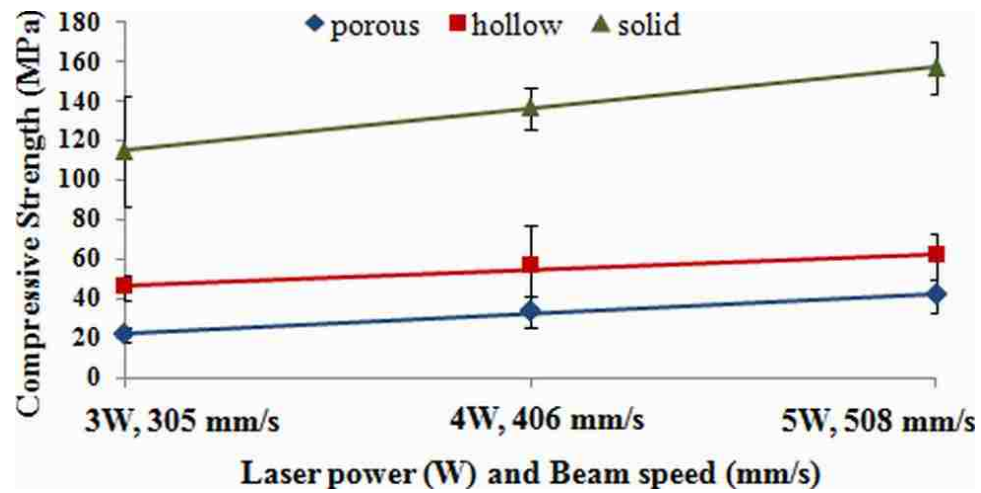


Figure 5. Effect of laser power and beam speed on the compressive strength of parts fabricated at the energy density of 1 cal/cm^2 .

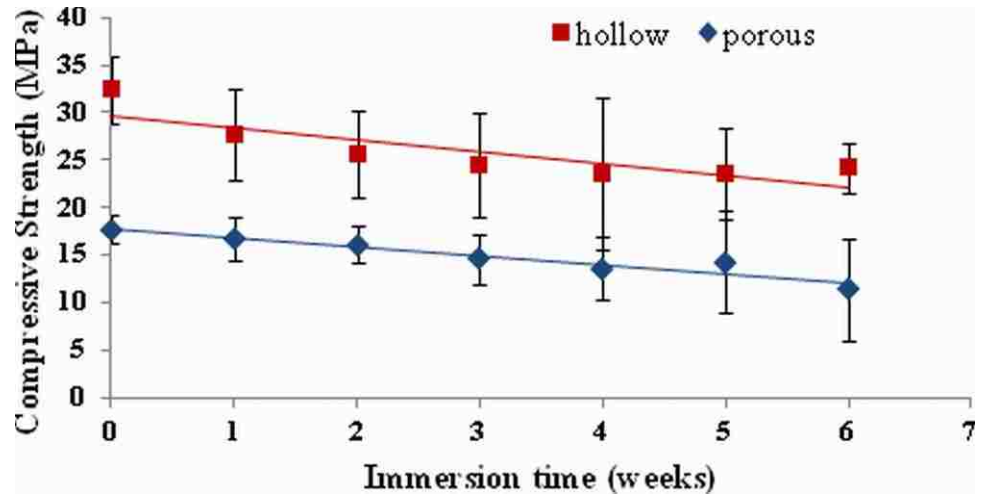


Figure 6. Variation of compressive strength of the samples immersed in the SBF.

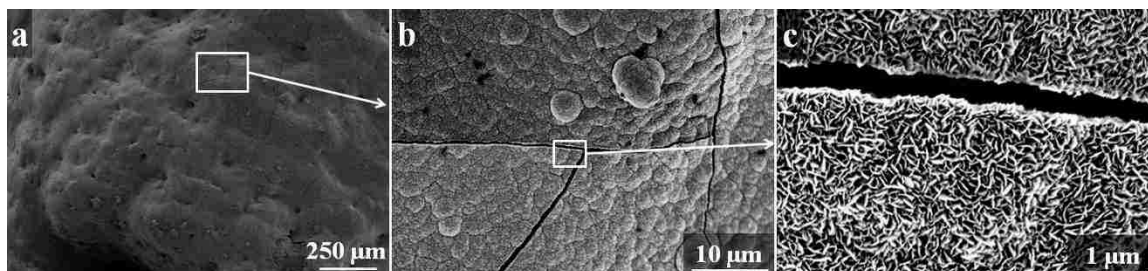


Figure 7. (a) surface morphology of SLS scaffold after immersion in SBF for 3 weeks, (b) magnified image showing surface cracks and 'cauliflower' like morphology, (c) high magnification image showing needle-like HA crystal formations.

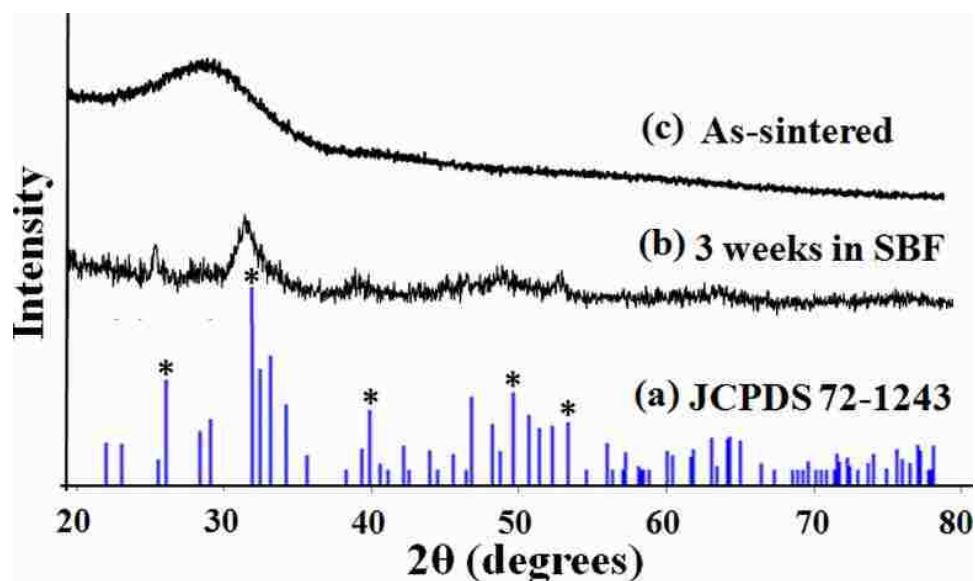


Figure 8. XRD patterns: (a) reference hydroxyapatite (JCPDS 72-1243), (b) scaffold after 3 weeks of immersion in the SBF, (c) as-sintered scaffold representing a typical amorphous pattern of a silicate based 13-93 glass.

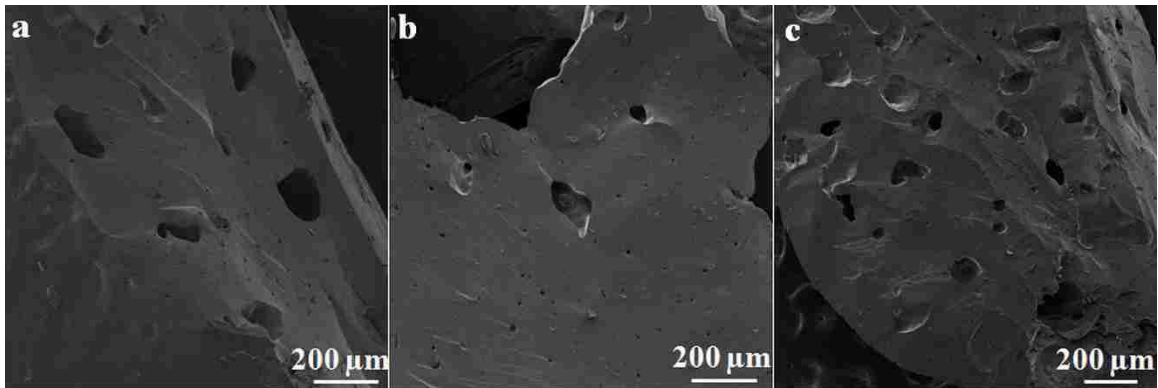


Figure 9. SEM images showing the effect of de-binding heating rates on microstructures of 13-93 bioactive scaffolds: (a) 0.5°C/min, (b) 1°C/min, and (c) 1.5°C/min.

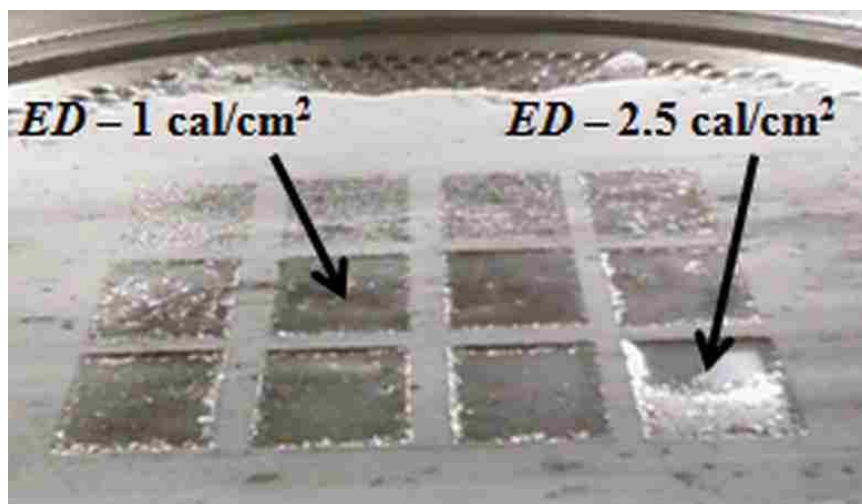


Figure 10. Degree of SA melting under the laser beam at different *EDs*. Higher *ED* resulted in increased outer contour dimensions and greater depths in melt pool.

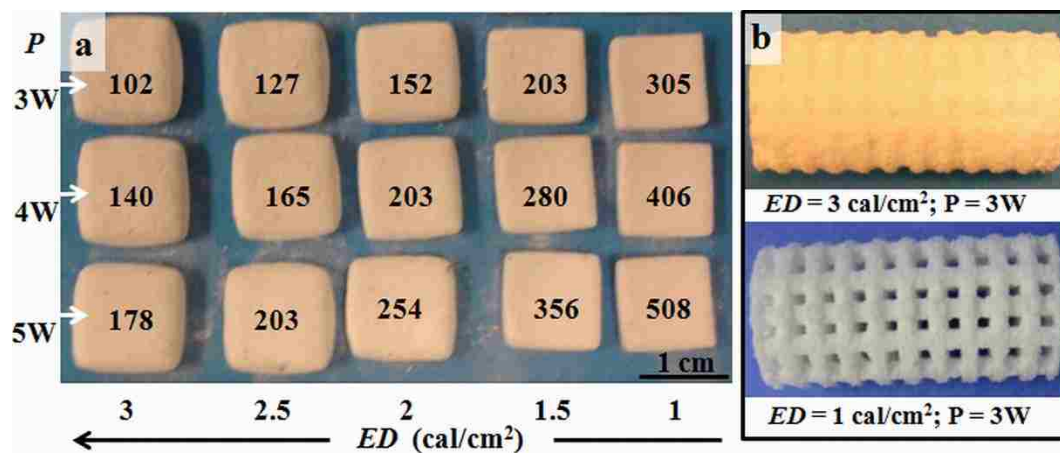


Figure 11. Effect of SLS parameters on the sharpness of features: (a) Fabricated green parts measuring 1 cm x 1 cm x 1 mm in dimensions. The numbers on the parts indicate the laser beam speed (*BS*) in mm/s, (b) Porous parts with the same design but fabricated at different energy densities.

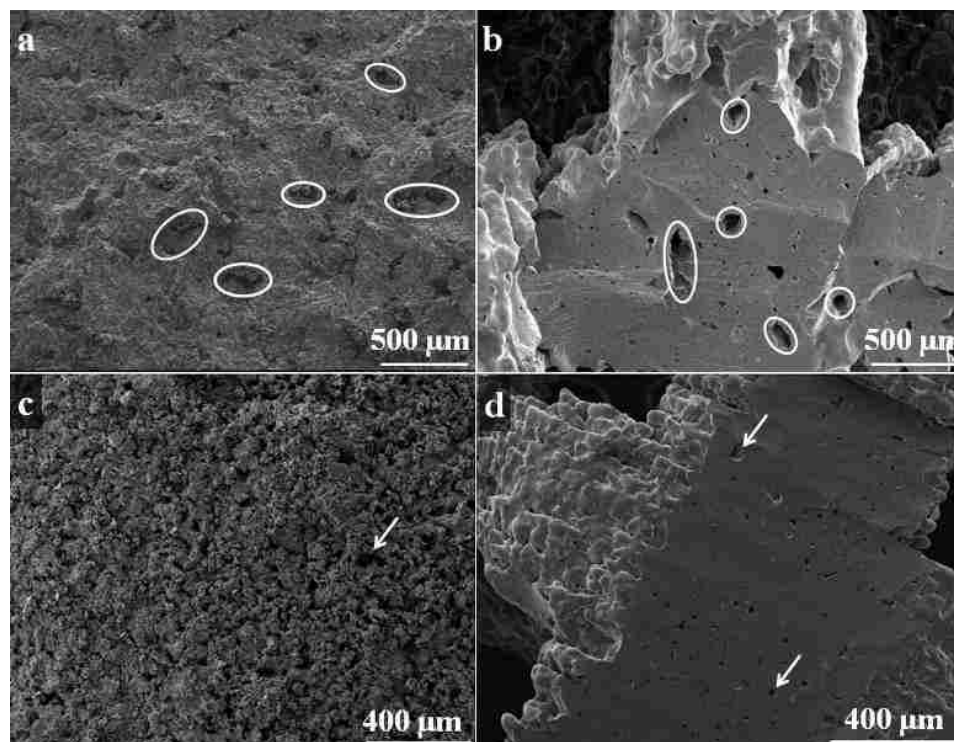


Figure 12. SEM images of the fractured surfaces: (a & b) green part fabricated at $P = 3W$, $ED = 1 \text{ cal/cm}^2$ and the corresponding sintered part, (c & d) green part fabricated at $P = 5W$, $ED = 1 \text{ cal/cm}^2$ and the corresponding sintered part.

REFERENCES

1. Carter, D.R., Hayes, W.C., 1976. Bone compressive strength: the influence of density and strain rate. *Science*. 194, 1174–1176.
2. Caulfield, B., McHugh, P.E., Lohfeld, S., 2007. Dependence of mechanical properties of polyamide components on build parameters in the SLS process. *J. Mater. Process. Technol.* 182, 477-488.
3. Cesarano III, J., Dellinger, J.G, Saavedra, M.P., Gill, D.D., 2005. Customization of load-bearing hydroxyapatite lattice scaffolds. *Int. J. Appl. Ceram. Technol.* 2, 212-220.
4. Doiphode, N.D., Huang, T.S., Leu, M.C., Rahaman, M.N., Day, D.E., 2011. Freeze extrusion fabrication of 13-93 bioactive glass scaffolds for bone repair. *J Mater Sci: Mater Med.* 22, 515–523.
5. Fu, Q., Rahaman, M.N., Huang, W., Day, D.E., Bal, B.S., 2007. Preparation and bioactive characteristics of a porous 13-93 glass, and its fabrication into the articulating surface of a proximal tibia. *J. Biomed. Mater. Res.* 82A, 222-229.
6. Fu, Q., Rahaman, M.N., Bal, B.S., Brown, R.F., Day, D.E., 2008. Mechanical and in vitro performance of 13–93 bioactive glass scaffolds prepared by a polymer foam replication technique. *Acta Biomater.* 4, 1854-64.
7. Fu, Q., Rahaman, M.N., Fu, H., Liu, X., 2010. Silicate, borosilicate, and borate bioactive glass scaffolds with controllable degradation rate for bone tissue engineering applications. I. Preparation and in vitro degradation. *J. Biomed. Mater. Res.* 95A, 164-171.
8. Fu, Q., Saiz, E., Tomsia, A.P., 2011. Direct ink writing of highly porous and strong glass scaffolds for load-bearing bone defects repair and regeneration. *Acta Biomater.* 7, 3547-54.
9. German, R.M., 1987. Theory of Thermal Debinding *Int. J. Powder Metall.* 23, 237-245.
10. Gibson, I., Shi, D., 1997. Material properties and fabrication parameters in selective laser sintering. *Rapid Prototyping J.* 3, 129-136.
11. Goodridge, R.D., Dalgarno, K.W., Wood, D.J., 2006. Indirect selective laser sintering of an apatite–mullite glass-ceramic for potential use in bone replacement applications. *Proc. Inst. Mech. Eng. H* 220, 57-68.
12. Huang, T.S., Rahaman, M.N., Doiphode, N.D., Leu, M.C., Bal, B.S., Day, D.E., Liu, X., 2011. Porous and strong bioactive glass (13-93) scaffolds fabricated by freeze extrusion technique. *Mater. Sci. Eng. C*31, 1482-1489.

13. Hench, L.L., Anderson, O., 1993. Bioactive glasses. In: Hench, L.L., Wilson, J. (Eds.), *An Introduction to Bioceramics*, vol. 1. World Scientific Publishing Co. Pte. Ltd., Singapore, pp. 41-62.
14. Jaw, K-S., Hsu, C-K., Lee, J-S., 2001. The thermal decomposition behaviors of stearic acid, paraffin wax and polyvinyl butyral. *Thermochinica Acta.* 367-368, 165-168.
15. Karageorgiou, V., Kaplan, D., 2005. Review: Porosity of 3D biomaterial scaffolds and osteogenesis. *Biomaterials.* 26, 5474-91.
16. Keaveny, T.M., 2000. Strength of trabecular bone. In: Cowin, S.C. (Ed.), *Bone Mechanics Handbook: Second Edition*, CRC press, New York, pp. 16-4.
17. Kolan, K.C.R., Leu, M.C., Hilmas, G.E., Velez, M., 2010. Selective laser sintering of 13-93 bioactive glass. In: Bourell, D.L., Crawford, R.H., Seepersad, C.C., Beaman, J.J., Marcus, H. (Eds.), *Proceedings of the 21st Annual International Solid Freeform Fabrication Symposium*, Austin, Texas, USA, pp. 504-512.
18. Kolan, K.C.R., Leu, M.C., Hilmas, G.E., Brown, R.F., Velez, M., 2011. Fabrication of 13-93 bioactive glass scaffolds for bone tissue engineering using indirect selective laser sintering. *Biofabrication.* 3, 025004.
19. Kruth, J-P., Leu, M.C., Nakagawa, T., 1998. Progress in additive manufacturing and rapid prototyping. *CIRP Ann. Manuf. Technol.* 47, 525-540.
20. Kruth, J.P., Wang, X., Laoui, T., Froyen, L., 2003. Lasers and materials in selective laser sintering. *Assembly Autom.* 23, 357-371.
21. Kukobo, T., Takadama, H., 2006. How useful is SBF in predicting in vivo bone bioactivity? *Biomaterials.* 27, 2907-2915.
22. Lei, Z., Chao, Z.K., You, L.Z., Yong Z.X., 2006. Degradation and the kinetics of binder removal. *Met. Powder Rep.* 61, 28-33.
23. Leu, M.C., Adamek, E.B., Huang, T., Hilmas, G.E., Dogan, F., 2008. Freeform fabrication of zirconium diboride parts using selective laser sintering. In: Bourell, D.L., Crawford, R., Seepersad, C.C., Beaman, J.J., Marcus, H. (Eds.), *Proceedings of the 19th Annual International Solid Freeform Fabrication Symposium*, Austin, Texas, USA, pp. 194-205.
24. Leu, M.C., Shashwatashish, P., Hilmas, G.E., 2010. Optimization of selective laser sintering process for fabrication of zirconium diboride parts. In: Bourell, D.L., Crawford, R., Seepersad, C.C., Beaman, J.J., Marcus, H. (Eds.), *Proceedings of the 21st Annual International Solid Freeform Fabrication Symposium*, Austin, Texas, USA, pp. 493-503.

25. Lewis, J.A., 1997. Binder removal from ceramics. *Annu. Rev. Mater. Sci.* 27, 147–73.
26. Lewis, J.A., Smay, J.E., Stuecker, J., Cesarano III, J., 2006. Direct ink writing of three-dimensional ceramic structures. *J. Am. Ceram. Soc.* 89, 3599–3609.
27. Liu, J., Zhang, B., Yan, C., Shi, Y., 2010. The effect of processing parameters on characteristics of selective laser sintering dental glass-ceramic powder. *Rapid Prototyping J.* 16, 138 – 145.
28. Liu, Z., Nolte, J., Packard, J., Hilmas, G., Dogan, F., Leu, M., 2007. Selective laser sintering of high-density alumina ceramic parts. In: Hinduja, S., Fan, K-C. (Eds.), *Proceedings of the 35th International Matador Conference*, Taipei, Taiwan, pp. 351-354.
29. Lombardo, S.J., Feng, J.C., 2003. Determination of the min time for binder removal and optimum geometry for 3d porous green bodies. *J. Am. Ceram. Soc.*, 86, 2087–92.
30. Marchelli, G., Storti, D., Ganter, M., Prabhakar, R., 2010. An introduction to 3D glass printing. In: Bourell, D.L., Crawford, R.H., Seepersad, C.C., Beaman, J.J., Marcus, H. (Eds.), *Proceedings of the 21st Annual International Solid Freeform Fabrication Symposium*, Austin, Texas, USA, pp. 95-107.
31. Murphy, C.M., Haugh, M.G., O'Brien, F.J., 2010. The effect of mean pore size on cell attachment, proliferation and migration in collagen–glycosaminoglycan scaffolds for bone tissue engineering. *Biomaterials*, 31, 461-466.
32. Nelson, J.C., 1993. Selective laser sintering: A definition of the process and an empirical sintering model. Dissertation (PhD), University of Texas, Austin.
33. Panda, P.C., Raj, R., 1989. Sintering and crystallization of glass at constant heating rates. *J. Am. Ceram. Soc.*, 72, 1564-66.
34. Pinwill, I.E., Edirisinghe, M.J., Bevis, M.J., 1992. Development of temp-heating rate diagrams for the pyrolytic removal of binder used for powder injection moulding. *J. Mater. Sci.* 27, 4381-88.
35. Rahaman, M.N., 2006. *Ceramic Processing*, Taylor and Francis, New York, pp. 387.
36. Rahaman, M.N., Brown, R.F., Bal, B.S., Day, D.E., 2006. Bioactive glasses for nonbearing applications in total joint replacement. *Semin. Arthroplasty.* 17, 102-112.
37. Rahaman, M.N., Day, D.E., Bal, B.S., Fu, Q., Jung, S.B., Bonewald, L.F., Tomsia, A.P., 2011. Bioactive glass in tissue engineering. *Acta Biomater.* 7, 2355-73.
38. Rezwan, K., Chen, Q.Z., Blaker, J.J., Boccaccini, A.R., 2006. Biodegradable and bioactive porous polymer/inorganic composite scaffolds for bone tissue engineering. *Biomaterials.* 27, 3413-31.

39. Seitz, H., Rieder, W., Irsen, S., Leukers, B., Tille, C., 2005. Three-dimensional printing of porous ceramic scaffolds for bone tissue engineering. *J. Biomed. Mater. Res. B Appl. Biomater.* 74B, 782-788.
40. Subramanian, K., Vail, N., Barlow, J., Marcus, H., 1995. Selective laser sintering of alumina with polymer binders. *Rapid Prototyping J.* 1, 24-35.
41. Velez, M., Jung, S., Kolan, K.C.R., Leu, M.C., Day, D.E., Chu, T-M.G., 2011. In vivo evaluation of 13-93 bioactive glass scaffolds made by selective laser sintering. In: *Next Generation Biomaterials Symposium, Ceramic Transactions Proceedings, Materials Science and Technology*, Columbus, Ohio, USA.
42. Wohlert, M., Bourell, D., 1996. Rapid prototyping of Mg/SiC composites by a combined SLS and pressureless infiltration process. In: Beaman, J.J., Barlow, J.W., Bourell, D.L., Crawford, R. (Eds.), *Proceedings of the 7th Annual International Solid Freeform Fabrication Symposium*, Austin, Texas, USA, pp. 79-87.
43. Xiao, K., Dalgarno, K.W., Wood, D.J., Goodridge, R.D., Ohtsuki, C., 2008. Indirect selective laser sintering of apatite-wollastonite glass-ceramic. *Proc. Inst. Mech. Eng. H* 222, 1107-1114.

II. EFFECT OF POROSITY AND PORE GEOMETRY OF LASER SINTERED BIOACTIVE GLASS SCAFFOLDS ON MECHANICAL PROPERTIES

Krishna C. R. Kolan¹, Ming C. Leu¹, Gregory E. Hilmas²

¹Department of Mechanical and Aerospace Engineering, Missouri University of Science and Technology, Rolla, MO 65409, USA

²Department of Materials Science and Engineering, Missouri University of Science and Technology, Rolla, MO 65409, USA

ABSTRACT

The pore geometry of the scaffolds intended for use in bone repair or replacement, is one of the most important parameters in bone tissue engineering. It affects not only the mechanical properties of the scaffolds but also the amount of bone regeneration after implantation. Scaffolds with five different pore geometries and four porosity levels were fabricated using borate bioactive glass (13–93B3) using the selective laser sintering (SLS) process. The pore size of the scaffolds varied from 400 to 1300 μm . The compressive strength of the scaffolds varied from 1.7 to 15.5 MPa for porosities ranging from 60 to 30%, respectively, for the different pore geometries. Scaffolds were soaked in a simulated body fluid (SBF) for one week, followed by measurements in the variation in mechanical properties and the amount of bioactive glass surface conversion. The results indicated that the degradation of the scaffolds can be controlled to a certain extent with an appropriate design of pore geometry and porosity of the scaffolds by selecting relevant bioactive glass for bone repair.

Keywords: Selective laser sintering, Bioactive glass scaffold, Bone repair, Porosity, Pore geometry

1. INTRODUCTION

The discovery of Bioglass[®] by Prof. Hench in 1969 has led to active research interest in the field of bioactive materials in the past four decades [1, 2]. Bioactive materials convert to Hydroxyapatite (HA), the main mineral constituent of bone, when exposed to body fluids thereby integrating with the surrounding tissue. Recently, interest has focused on developing bioactive glasses as they offer excellent biological characteristics when compared to glass-ceramics or ceramics. Borate based bioactive glasses not only bond to the surrounding hard tissue but are also known to bond with soft tissues [3, 4]. Table 1 shows the compositions of the borate based 13-93B3 bioactive glass in comparison to the silicate based 13-93 bioactive glass. The 45S5 glass composition is also included for comparison. The molar concentration of SiO₂ in 13-93 glass is replaced by B₂O₃ in the 13-93B3 glass. The borate glass is chemically less durable when compared to the silicate glass and therefore, it degrades at a faster rate and allows for faster bone formation in comparison to the silicate glass [3-5].

Recently, 13-93B3 glass scaffolds, with ~50% porosity, were fabricated with an organic based paste composition using the Robocasting technique [6, 7]. Although porosity and pore size can be controlled using Robocasting, the process has limited control over the pore geometry when fabricating scaffolds because of the layer-by-layer filament deposition. In comparison, powder based additive manufacturing (AM) techniques like the selective laser sintering (SLS) process provide flexibility in fabricating scaffolds with complex pore geometries as they do not require support structures during part fabrication. Therefore, the SLS process provides an opportunity to investigate the effects of porosity and pore geometry on the structural and cell

proliferation properties of the scaffolds. There have been some articles in the literature wherein researchers have proposed techniques to develop CAD models for scaffolds which closely mimic the architecture of human trabecular bone [8-10]. However, fabricating bioceramic scaffolds with such complex pores is still a challenge since not all AM techniques can be used to fabricate them at required pore sizes (~100 – 300 μm) [11]. To date, there are no commercial AM machines that can directly fabricate bioceramic scaffolds. The manufacturing process needs to go through an indirect approach viz., addition of a polymeric binder to make the shape followed by a binder removal step and then sintering of bioceramic particles. There are certain AM machines which can be used to manufacture anatomically challenging and complex shaped implants for large skeletal repair applications such as skull, etc., but with titanium alloy materials. For such metallic lattices, the effect of pore geometries on mechanical properties and cell growth were also reported [12-14]. Nevertheless, the bioactive glass degrades upon implantation thereby affecting the mechanical properties. Therefore, an investigation into the mechanical properties of the bioactive glass scaffolds and their degradation would provide relevant information regarding the choice of bioactive glass and pore geometry that is required to repair different locations in the bone. In this work, we compare bioactive glass scaffolds with different lattices including the traditional lattices formed via X-Y-Z oriented struts and also lattices formed based on the freeform surfaces. The aspect of manufacturability has been considered in the design and fabrication process of these scaffolds.

In our previous work, we have shown that bioactive glass scaffolds made by the SLS process provide good mechanical properties and preferable surface morphology for

cell proliferation [15, 16]. In the current work, we investigate the effects of pore geometry and porosity on the cell proliferation and mechanical properties of the scaffolds. Five different architectures were considered and the scaffolds were fabricated with each of these architectures at four designed porosity levels. The sintered scaffolds were immersed in simulated body fluid (SBF) for one week and the effects of pore geometry and porosity on the compressive resistance of the scaffolds were studied.

2. MATERIALS AND METHODS

2.1. FABRICATION OF SCAFFOLDS

13-93B3 (borate) bioactive glass (prepared by Mo-Sci Corp., Rolla, MO) was used in this research. The average size of the glass particles was measured $\sim 12 \mu\text{m}$ (d_{50}). Particle size distributions were obtained using a laser diffraction-based particle size analyzer (S3500, Microtrac Inc., Largo, FL). The bioactive glass particles were mixed with stearic acid as the binder ($\text{C}_{18}\text{H}_{36}\text{O}_2$, grade HS, Acros Organics, Morris Plains, NJ) and dry ball-milled for 8 hrs with ZrO_2 milling media to obtain the feedstock powder for the SLS machine. The fabrication experiments were carried out on a commercial DTM Sinterstation 2000 machine. The effect of SLS parameters on fabricating scaffolds using stearic acid binder and bioactive glass powder was investigated in our previous work [16], and the same set of parameters (laser power – 5 W, scan speed – 508 mm/s, scan spacing – 0.23 mm, layer thickness – 76.2 μm , 15% binder content) were adopted for the current study.

2.2. POST-PROCESSING AND PHYSICAL ASSESSMENT OF SCAFFOLDS

The fabricated green parts were post-processed in a three-stage programmable air furnace (Vulcan Benchtop Furnace, York, PA). The following heat treatment schedule was used for this study: an initial de-binding heating rate of $0.1^\circ\text{C}/\text{min}$ to 550°C , then increasing the heating rate to $1^\circ\text{C}/\text{min}$ until a final sintering temperature of 570°C with a 1 hour hold, and then turning the furnace off to allow material cooling to room temperature (at $\sim 15^\circ\text{C}/\text{min}$). Optical microscopy was used to measure the pore sizes of the sintered scaffolds. Archimedes method was used to measure the apparent porosity of the sintered scaffolds. Cubic shaped parts measuring 10 mm in length were used for the

purpose of measuring porosity, and parts measuring 5 mm in length were used for the purpose of mechanical testing and the SBF study. A cross-head speed of 0.5 mm/min was used on a mechanical load frame (Instron 4469 UTM, Norwood, MA) to determine the compressive strengths of the parts. Scans were run from 2θ values ranging from 10° to 80° using Cu K α radiation ($\lambda = 0.154056$ nm) for powder X-ray diffraction (XRD) analysis (Philips X-Pert, Westborough, MA) on the as-received bioactive glass powders, sintered scaffolds, and also on the dried scaffolds after removing them from the SBF to determine the changes in the crystalline/amorphous nature of the material. Five samples in each set were used for compressive testing of the sintered and dry scaffolds and the results were reported as the mean \pm one standard deviation (\pm SD).

2.3. SBF TESTS

The SBF solution was prepared using the Kokubo method [17]. All the samples were ultrasonically cleaned three times using ethanol and then dried in an oven overnight before being kept in the SBF solution (100 ml of solution was used for 1 g of the scaffold for soaking). The SBF solution container with scaffolds was kept in an incubator maintained at 37°C . All the compression tests were conducted on wet scaffolds to provide realistic data on the degradation of the scaffolds. Scanning electron microscopy (SEM) (S-570, Hitachi Co., Tokyo, Japan) was used to analyze the surface morphology of the scaffolds. At least three samples in each set were used for compression testing of the SBF soaked scaffolds and the results were reported as the mean \pm SD.

3. RESULTS

3.1. EFFECT OF FABRICATION AND SINTERING ON POROSITY

The CAD models of the repeatable units of the five architectures considered in this work are shown in Figure 1(a). The first, second, and third unit cubes are termed cubic, spherical, and X architectures, respectively. The porosity in the unit cubes of cubic and X architectures is a function of the size of the unit cell and the diameter of the struts. In the case of spherical architecture, the porosity is a function of diameter of the sphere subtracted from the cube. These three architectures are the typical and frequently used designs in most of the AM techniques to manufacture scaffolds. The fourth and fifth are “diamond” and “gyroid” architectures, which were intended to mimic the trabecular bone architecture. The surface was generated using open source software K3DSurf v0.6.2 [18]. The surface generated was modeled into a volume with the help of pre-processor software and then converted to a .STL file for fabrication using the SLS machine. The fabricated scaffolds after binder burnout and sintering are shown in Figure 1(b) as representative specimens for each of the architectures in the same order as shown in Figure 1(a). The CAD models of the scaffolds with each of these pore geometries were designed at 50, 60, 70, and 80% porosity levels. The measured apparent porosities using Archimedes principle (presented in Table 2) were observed to be ~20% lower in comparison to the porosities of their CAD models. Figure 1(c) shows the diamond architecture scaffolds of same size and different porosities. Therefore, it is noted that the difference in porosity factor should be accounted for while fabricating porous parts using the SLS process.

3.2. EFFECT OF POROSITY AND PORE GEOMETRY ON MECHANICAL STRENGTH

Figure 2 shows the variation in the compressive strengths of the scaffolds made with different architectures at measured porosity levels of ~30% to ~60%. The vertical error bars represent the standard deviation of the measured compressive strength and the horizontal error bars represent the standard deviation in the measured porosity of the scaffolds. The scaffolds with a cubic architecture and a porosity of ~33% provided the highest compressive strength among all of the scaffolds. The scaffolds with the X architecture showed the lowest compression strength among all the architectures (~4.5 MPa at ~35% porosity). Out of the two architectures designed to closely mimic trabecular bone, the gyroid offers a higher compressive strength than the diamond architecture because of the relatively thick struts (~1.3 mm for gyroid compared to ~0.9 mm for diamond) and their wavy nature. The compressive strengths of the scaffolds at the low porosity level (~30%) are near the high end of the range of compressive strengths for a human trabecular bone (~2 to ~12 MPa), whereas the strengths measured for the scaffolds at the high porosity level (~60%) are near the low range of the strength of human trabecular bone [19]. Though the scaffold with cubic architecture provides the highest compressive strength, its rate of strength reduction with respect to increase in porosity is the fastest among all the scaffolds with different architectures. The scaffolds with the spherical architecture exhibited the smallest reduction in compressive strength. The other three architectures, namely, X, diamond, and gyroid, have a similar rate of reduction in compressive strength with respect to porosity. A detailed discussion on the strength is provided in Section 4.

3.3. EFFECT OF SBF IMMERSION ON MECHANICAL STRENGTH

The scaffolds were mechanically tested in a wet state after immersion in SBF for one week. The compressive strength measured for each of the scaffolds was about 2 MPa or slightly less, which is near the low end of the range of compressive strength (2 – 12 MPa) of a human trabecular bone [19]. The only exceptions were the scaffolds with cubic and spherical pore geometries with measured porosities about ~32% (shown in Table 2), for which strengths were measured ~4 MPa. The reduction in strengths of the scaffolds with different pore geometries from ‘as-sintered dry state’ to ‘wet state’ after immersion in SBF for one week is shown in Figure 3. Among the scaffolds with higher porosity (~55% – 66%; see Table 2), irrespective of the pore geometry, the reduction in strength in the wet scaffolds is more than ~90% in comparison to the as-sintered, dry scaffolds.

After testing, the scaffolds were dried at room temperature, sputter coated with gold-palladium, and investigated using SEM. Specifically, SEM was used to look for any crystal-like formations on the surface, which were typically formed within one week after immersion of the scaffolds’ in SBF. Figure 4 shows SEM images of a representative “X” architecture scaffold taken out of the SBF after 7 days. The outer surface morphology of the SLS scaffold is shown in Figure 4(a). Figure 4(b) shows the fracture surface of the scaffold. The reacted surface of the scaffold with SBF can be clearly distinguished with an unconverted 13-93B3 glass core as indicated in the image. Figure 4(c) shows a higher magnification image indicating the rounded HA-like crystal formations, unlike needle-like crystal formations on a 13-93 glass, on the surface of the scaffold after reacting with the SBF which is similar to the observations made by other researchers with this glass [5, 16].

4. DISCUSSION

With the advent of AM technologies in the 1990's, several scaffold designs have been proposed by researchers for the purpose of bone tissue engineering [20-22]. However, only more recently have researchers revealed the requirements of scaffolds for bone tissue engineering in terms of pore size, porosity, etc. For example, the scaffolds for bone repair are recommended to have an average pore size of $\sim 300 \mu\text{m}$ for better cell proliferation and tissue growth [23]. Considering the above, and also the fact that none of the existing AM machines can directly fabricate bioceramic scaffolds without going through post-processing, the only fabrication route is an indirect method i.e., to mix the bioceramic with an organic binder, followed by binder burnout and sintering to densify the inorganic scaffold. Several parameters would come into picture via this route such as, (i) resolution of the machine (laser spot diameter and layer thickness), (ii) amount of binder content (higher the binder greater the shrinkage), (iii) particle size (smaller the size, better in removal of unsintered powder from pores and less deviation from actual design), and lastly, (iv) the design itself. The laser spot diameter of the DTM Sinterstation 2000 used in this study was $\sim 450 \mu\text{m}$. The laser would cause heating of the feedstock material on the powder bed adjacent to the scanning area of the part, effectively reducing the designed pore size in the green part. The pore size was limited by the DTM 2000 Sinterstation used in our study. The amount of binder content and the particle size were optimized for scaffold fabrication in our previous work and the same are used in the current work as well [16]. Therefore, the fourth and key aspect of designing the unit cells of all the scaffolds was made by considering the manufacturability. For example, in the scaffold designed with spherical pore, a reduction in porosity can be achieved by

decreasing the diameter of the sphere to be subtracted from the cube. However, decreasing the diameter of the sphere will decrease the pore diameter thereby limiting the removal of unsintered powder from fine pores after SLS fabrication, thus increasing the likelihood of damaging the scaffold structure. Therefore, the pore sizes of all the scaffolds were designed in such a way that the unsintered powder could be removed after scaffold fabrication. The average pore sizes measured using an optical microscope as presented in Table 3 provide a fair estimation of the pores achievable for the sintered scaffolds with different pore geometries.

The difference in compressive strength offered by the five architectures is significant at lower porosities and amongst them, the cubic architecture offers the highest compressive strength (see Figure 2). This can be attributed to the struts in the z-direction which can carry a majority of the load, whereas such a design feature is not present in any of the other architectures. The strength of scaffolds at higher porosities is ~ 3 MPa or less, which is either equal to or less than the lowest strength of trabecular bone. This indicates that the effect of pore geometry is not significant at the higher porosities from the strength perspective in repairing trabecular bones using bioceramics, although it may be significant for cell proliferation and new tissue regeneration. Thus, for load-bearing bone repair, the effect of pore geometry is significant only at the lower porosities and the scaffold architecture could play a key role when utilizing implants with lower porosities for load-bearing applications.

In order to comprehend the variation in compressive strength of the scaffolds with different pore geometries, the cross-sectional area of a unit cell is plotted with respect to the thickness (height) of the unit cell. Figure 5 shows the variation in the cross-sectional

area of a unit cell along the thickness, for all the unit cells. As the length of unit cell is not uniform among the different architectures, the z height is divided by the unit cell length to provide the z value, which varies from 0 to 1 corresponding to the start and end of the unit cell thickness. Similarly, the cross-sectional area values are also converted to ratios based on the maximum cross-sectional area for the corresponding unit cell (height x height). The minimum cross-sectional area offered by a particular unit cell in compression could be understood from the normalized cross-sectional area vs z value graphs. The structural failure of a porous ceramic part, in general, is attributed to flaws present in the microstructure. It is assumed that the failure occurs when the weakest link in a lattice structure (minimum cross-sectional area) fails because of the highest stress concentration. Therefore, it is essential to investigate the minimum cross-sectional area offered by the unit cell w.r.t. the height of the unit cell.

The area under the norm cross-sec area vs. z value graph will be in direct correlation to the volume of the unit cell. The percentage of this volume which is under the minimum cross-sectional area region (the area below the valley's in the graphs; as the porosity increases the shape of the valley broadens) corresponds to the volume of the material with minimum cross-sectional area. And the presence of flaws/voids in this zone could act as a weakest link in the structure with increased chances of failure. It can also be observed that the probability of occurrence of such weakest link increases with increase in the porosity. Also, the chances of failure are higher for gyroid and diamond architectures as most of the unit cell volume is under high stress concentration. Similarly, failure chances are relatively less for X architecture because of the sharp valleys of the norm cross-sec area vs. z value graphs of the X unit cell meaning the unit cell volume

which is under high stress concentration is less when compared to diamond or gyroid architectures. However, in reality, scaffolds with gyroid and diamond pore geometries have a higher compressive strength when in comparison to the scaffolds with X architecture. This shows that the current assumption that the failure of the scaffolds solely based on the minimum cross-sectional area is not sufficient to explain the differences amongst the scaffold designs though it explains the variation in strength for one scaffold type with respect to porosity.

There have been several models proposed to estimate the strength of a porous ceramic part based on the shape of the void. Ryshekewitch and Duckworth first proposed the failure trends which followed the exponential equation and states that the mechanical properties are dependent on the porosity and pore shape as per the following equation [24, 25]:

$$\sigma = \sigma_o e^{-BP} \quad \text{where, } \begin{array}{l} \sigma - \text{Strength of porous part; } \sigma_o - \text{Strength of dense part;} \\ B - \text{Pore shape factor; } P - \text{Porosity fraction;} \end{array}$$

The above model was later empirically developed for the basic pore shapes of oblate, elliptical and spherical [26]. Though the equation is developed for closed pores, it has been reported that the open porosity ceramic lattice structures also follow the equation when the pore shape and pore size are independently modified [27]. Whereas, the current scenario is different in two ways, firstly, the porosity is interconnected and secondly, the increase in porosity is because of the increase in pore volume. Therefore, the value of B in the equation could be a function of the both shape and size of the pore and the equation

could be modified by addition of another empirical constant. Figure 6 shows the compressive strength vs. porosity data for the scaffolds with different pore geometries fitted with the described model. The following are the equations representing the trends of the compressive strength of the scaffolds shown in Figure 6 with different pore shapes.

For cubic scaffold: $\sigma = 2.35\sigma_o e^{-5.3P} = \sigma_o e^{0.854-5.3P}$

For spherical scaffold: $\sigma = 0.72\sigma_o e^{-2.8P} = \sigma_o e^{-0.335-2.8P}$

For X scaffold: $\sigma = 1.34\sigma_o e^{-6.6P} = \sigma_o e^{0.293-6.6P}$

For gyroid scaffold: $\sigma = 3.02\sigma_o e^{-6.7P} = \sigma_o e^{1.105-6.7P}$

For diamond scaffold: $\sigma = 1.28\sigma_o e^{-5.3P} = \sigma_o e^{0.247-5.3P}$

It can be observed from the above fitted equations that the original exponential equation fitted for the bioactive glass scaffolds can be modified as follows:

$$\sigma = \sigma_o e^{A-BP} \quad \text{where, } A, B \text{ – Empirical constants; } P \text{ – Porosity fraction;}$$

All the curves with the exception of the spherical scaffold follow a similar trend reported in the literature for the increase in pore sizes and porosity. The negative value of A for the scaffold with spherical pore geometry can be understood from the Figure 5 which shows the profiles of the cross-sectional area vs. z value of the unit cells. When the volumetric region (area under the valley) representing the minimum cross-sectional for a spherical unit cell is calculated and plotted with respect to the porosity fraction, the graph has a negative slope which is quite opposite to the trends in other unit cells where the graphs have a positive slope. This objectively means that when the probability of failure

increases with increasing porosity for the scaffolds with other pore geometries, the probability of failure for the spherical scaffold decreases with increasing porosity. This exception is because of the design for manufacturability which is considered in this work while fabricating spherical scaffolds. The shape of the pores of spherical scaffold changes with increasing porosity whereas the shape of the pores of other scaffold types remains the same.

The rate of degradation of an implant depends not only on the material but also its geometric design. This is because the reduction in the compressive strength of a scaffold is related to the surface area it offers after immersion in SBF. It can be observed from Figure 3 that the scaffolds designed for the porosity of 80% had the highest reduction (~90%) in compressive strength. This could be due to the large pores measuring about ~1 mm in those scaffolds (see Table 3), thereby allowing the SBF to contact and react with the inside surface of the scaffold. As shown in Figure 3, among the scaffolds designed with lower porosities (50 – 60%), the spherical architecture exhibited the smallest reduction in compressive strength (57 – 65%), and the scaffolds with the diamond architecture exhibited the largest reduction in compressive strength (80 – 87%). For further comprehension, the percentage reduction in strength is plotted against the ratio of total surface area over volume offered by a scaffold, as shown in Figure 7. The surface area was calculated based on the CAD model, accounting for the shrinkage of the scaffold after post-processing. Note that the actual surface area should be higher if considering the surface roughness of the parts fabricated by the SLS process. Two groups of the data points can be seen in Figure 7. The data points for gyroid and diamond scaffolds form a distinguishable group from the traditional lattice structures of cubic,

spherical, and X scaffolds. For a given SA/volume ratio (e.g., 2), the gyroid and diamond scaffolds resulted in a greater reduction in strength compared to the traditional lattice structures. This indicates that the tortuosity and permeability offered by the pore geometries in the gyroid and diamond scaffolds, which mimic trabecular bone, has a pronounced effect on the degradation of the scaffold.

We have shown in this study that implants with complex internal architectures mimicking trabecular bone can be fabricated with bioactive glasses and ceramics using the SLS process. In contrast, such a capability is more limited for extrusion-based additive manufacturing processes like the Freeze-form Extrusion Fabrication [28], Robocasting [6], and Direct Ink Writing [29] at the present time. The degradation of SLS scaffolds is expected to be faster than scaffolds fabricated by extrusion-based processes because of the increased surface area as a result of increased part surface roughness associated with the SLS process. The compression tests of the scaffolds, after immersion in the SBF for one week, in our study indicate that the percentage reduction in strength (i.e., rate of degradation) for all scaffold types vary between 60 to 90%. This data can be used to select a particular design for repair of a defect site in a trabecular bone depending on the strength required to repair the defect site. The above result shows the potential of the SLS process for bone repair by utilizing the combination of pore geometry, porosity and the choice of biomaterial of the scaffolds. For example, diamond pore geometry could be the choice for an implant fabricated with a bioglass having a slower degradation rate as the diamond pore provides faster degradation by means of its design. Similarly, if the bone repair application requires more structural integrity for the implant over a period of time, a lower porosity and a cubic or spherical design could be the choice. Therefore,

for the trabecular bone repair, the SLS process could be used to manufacture bioactive glass scaffolds with controlled rates of strength degradation by selecting the appropriate geometric design and material combinations.

5. CONCLUSIONS

Our study has shown that among the borate-based bioactive glass scaffolds fabricated by the selective laser sintering (SLS) process, the cubic pore architecture provides the highest compressive strength at lower porosities (< 40%). However, scaffolds with the cubic architecture also exhibit the highest rate of reduction in the compressive strength with increased porosity among all the architectures considered. The effect of different architectures at higher porosities (> 65%) is not significant from a strength retention perspective for bone repair because all the scaffolds offer low compressive strengths, which are less than the lower range of the compressive strength of human trabecular bone. The simulated body fluid tests indicates that, for a same ratio of surface area to volume of the scaffold, the gyroid and diamond architectures, which mimic trabecular bones, have higher percentages of reduction in the compressive strengths in comparison to the traditional lattice structures because of their tortuosity and permeability. The study has shown that the SLS process could be used to fabricate scaffolds with controlled rates of strength degradation and bone regeneration by selecting appropriate architecture and bioactive glass in repairing a specific region of the trabecular bone.

ACKNOWLEDGEMENTS

The authors thankfully acknowledge the technical assistance of Taylor Comte during this work and Mo-Sci Corp., Rolla, MO., for supplying the bioactive glass used in this work.

Table 1. Compositions (in wt.%) of 13-93 and 13-93B3 glasses compared to 45S5 glass.

	SiO ₂	P ₂ O ₅	CaO	MgO	Na ₂ O	K ₂ O	B ₂ O ₃
45S5	45	6	24.5	-	24.5	-	-
13-93	53	4	20	5	6	12	-
13-93B3	-	3.7	18.5	4.6	5.5	11.1	56.6

Table 2. Differences in porosities: designed in CAD vs. measured after sintering.

Architecture	Porosity in %			
	50	60	70	80
Cubic	33.38	39.91	53.88	65.76
Spherical	31.53	42.04	49.02	60.58
X	27.79	34.59	43.17	54.98
Diamond	33.85	39.87	46.73	61.37
Gyroid	34.31	40.91	49.4	59.46

Table 3. Pore sizes of the sintered scaffolds at various porosities.

Architecture	Pore sizes (in μm) at respective measured porosities (in %)			
	~32%	~40%	~49%	~62%
Cubic	500	700	950	1300
Spherical	500	650	800	900
X	400	550	700	1200
Diamond	800	900	1000	1200
Gyroid	800	900	1000	1100

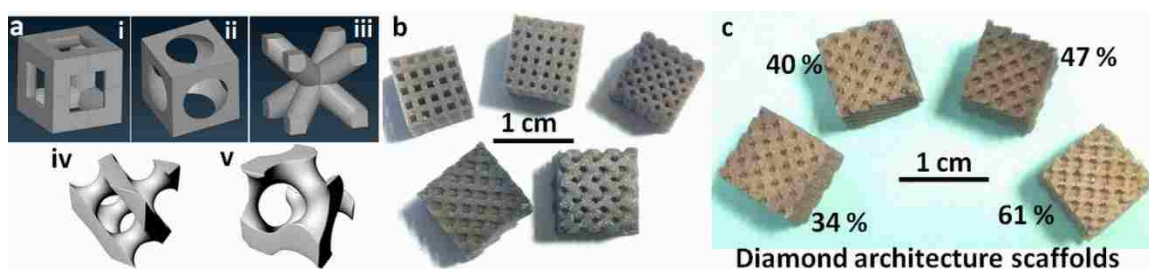


Figure 1. (a) CAD models of the repeatable units of five architectures: (i) cubic, (ii) spherical, (iii) X, (iv) diamond, and (v) gyroid; (b) 13-93B3 scaffolds with different architectures after sintering; (c) Diamond architecture scaffolds at four different porosities.

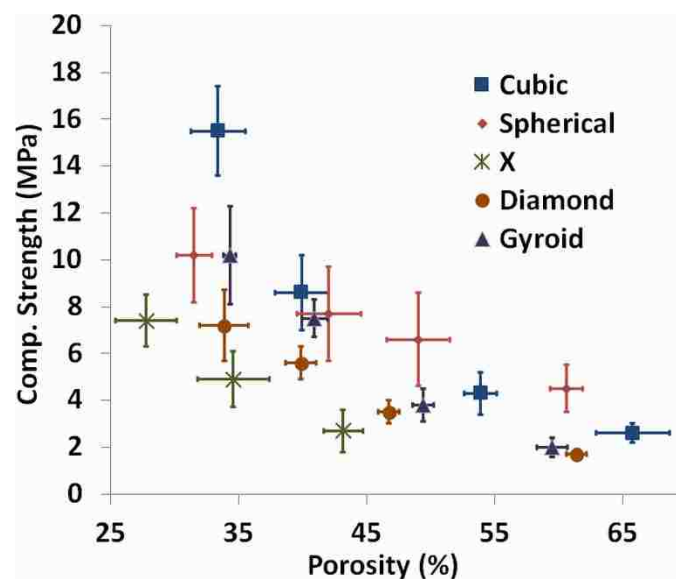


Figure 2. Compressive strengths for 13-93B3 scaffolds with five different pore geometries and at different porosities. Vertical and horizontal error bars represent the SD of the measured compressive strength and porosities, respectively.

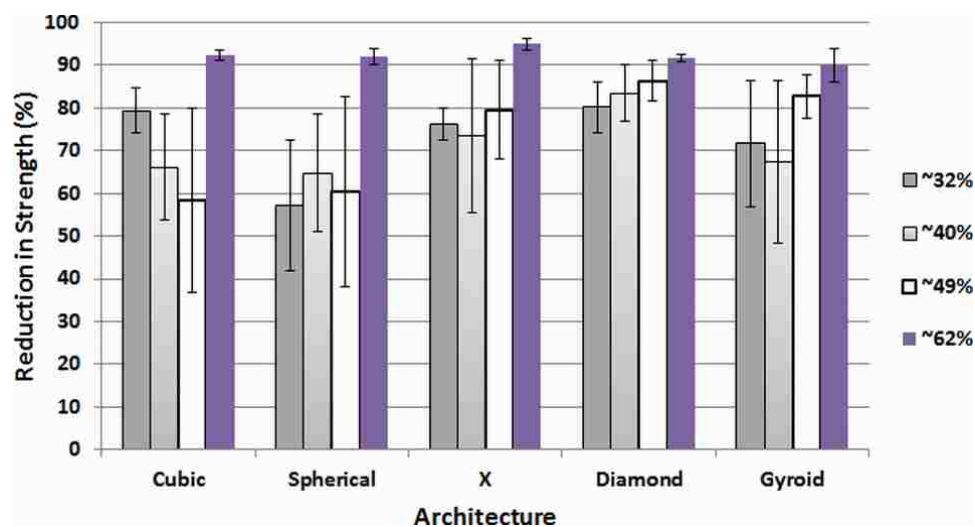


Figure 3. A comparison of the reduction in compressive strengths of scaffolds with different pore geometries and porosities after immersion in SBF for 7 days.

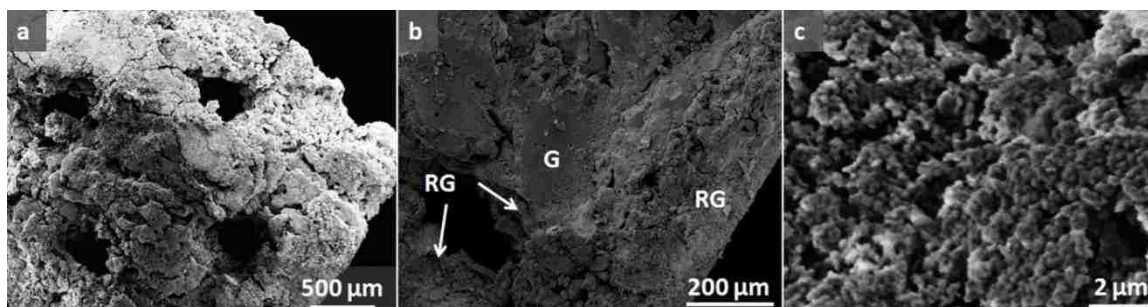


Figure 4. SEM images of a scaffold after immersion in SBF for 7 days: (a) outer surface morphology, (b) fracture surface of the scaffold indicating the reacted glass (RG) on the outer surface and unconverted glass (G), (c) higher magnification image of RG showing HA-like rounded crystal formations on the surface of the scaffold.

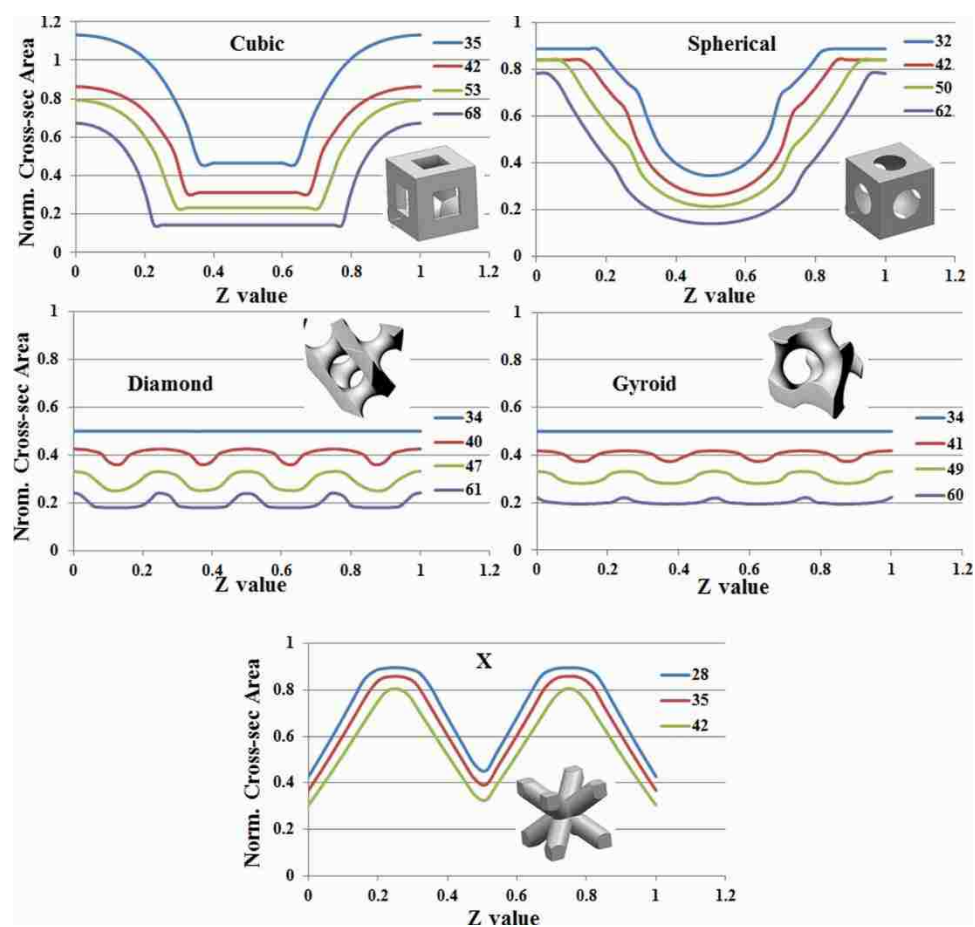


Figure 5. Normalized cross-sectional area vs. Z value graphs for the unit cells at different porosities.

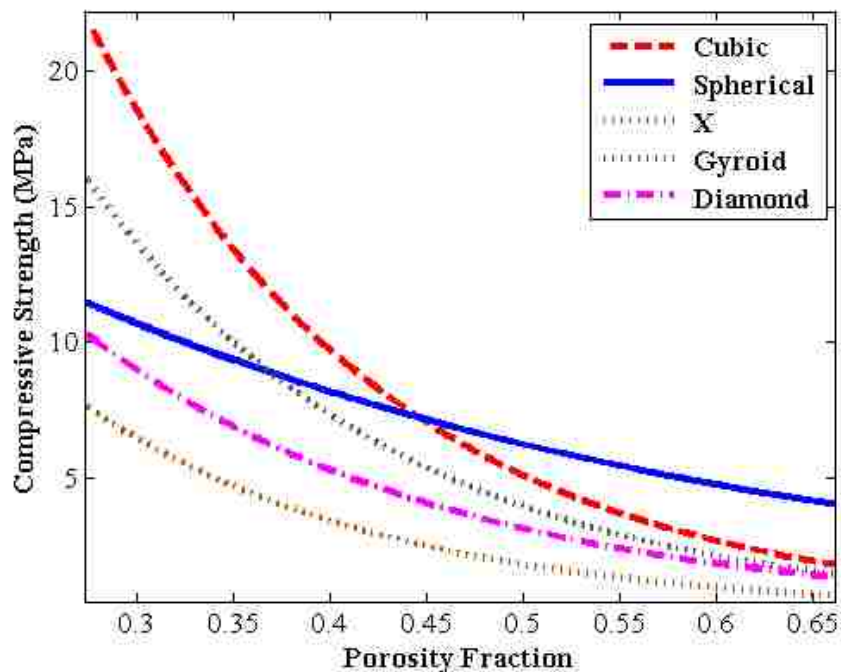


Figure 6. Compressive strength (MPa) vs. Porosity fraction of scaffolds with different pore geometries fitted with exponential functions (all with R^2 value of 0.98 and above).

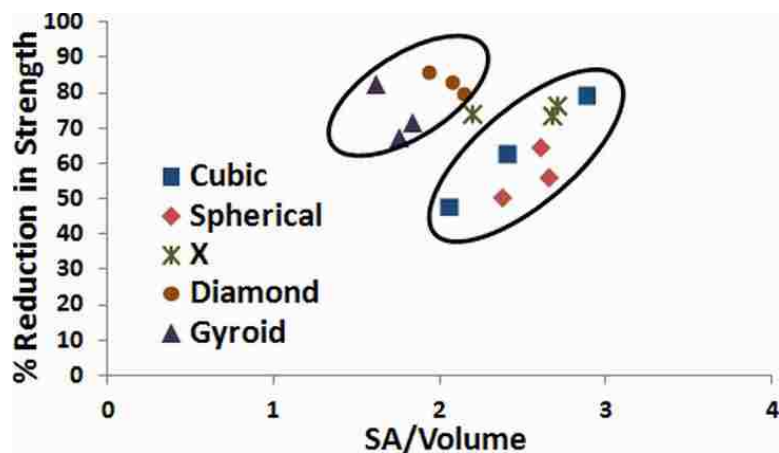


Figure 7. Percentage reduction in compressive strength of a scaffold vs. ratio of total surface area (SA) offered by the scaffold in its cubic volume space.

REFERENCES

1. Hench LL, Wilson J. An Introduction to Bioceramics. Singapore: World Scientific Publishing Co. Pte. Ltd; 1993. p 47.
2. Hench LL. The story of bioglass. *J Mater Sci Mater Med* 2006;17:967–978.
3. Rahaman MN, Day DE, Bal BS, Fu Q, Jung, SB, Bonewald LF. Bioactive Glass in Tissue Engineering. *Acta Biomater* 2011;7:2355-2373.
4. Lianxiang B, Jung S, Day D, Neidig K, Dusevich V, Eick D, Bonewald L. Evaluation of bone regeneration, angiogenesis, and hydroxyapatite conversion in critical-sized rat calvarial defects implanted with bioactive glass scaffolds. *J Biomed Mater Res Part A* 2012;100A:3267-3275.
5. Fu Q, Rahaman MN, Fu H, Liu X. Silicate, borosilicate, and borate bioactive glass scaffolds with controllable degradation rate for bone tissue engineering applications. I. Preparation and in vitro degradation. *J Biomed Mater Res* 2010;95A:164-171.
6. Deliormanli A, Rahaman MN. In vitro evaluation of silicate and borate bioactive glass scaffolds prepared by robocasting of organic based suspensions. *Cer Eng Sci Proc* 2012;33(6):11-20.
7. Deliormanli A, Liu X, Rahaman MN. Evaluation of borate bioactive glass scaffolds with different pore sizes in a rat subcutaneous implantation model. *J Biomater Appl* 2012; doi:10.1177/0885328212470013.
8. Cai S, Xi J. A control approach for pore size distribution in the bone scaffold based on the hexahedral mesh refinement. *Computer-Aided Design* 2008;40:1040-1050.
9. Challis VJ, Roberts AP, Grotowski JF, Zhang L-C, Sercombe TB. Prototypes for bone implant scaffolds designed via topology optimization and manufactured by solid freeform fabrication. *Adv Eng Mater* 2010;12:1106-1110.
10. Melchels FPW, Bertoldi K, Gabbriellini R, Velders AH, Feijen J, Grijpma DW. Mathematically defined tissue engineering scaffold architectures prepared by stereolithography. *Biomaterials* 2010;32:2878-2884.
11. Guo N, Leu MC. Additive manufacturing: technology, application and research needs. *Front Mech Eng* 2013;
12. Speirs M, Humbeeck JV, Schrooten J, Luyten J, Kruth JP. The effect of pore geometry on the mechanical properties of selective laser melted Ti-13Nb-13Zr scaffolds. *Procedia CIRP* 2013;5:79-82.
13. Ahmadi SM, Campoli G, Yavari SA, Sajadi B, Wauthle R, Schrooten J, Weinans H, Zadpoor AA. Mechanical behavior of regular open-cell porous biomaterials made of diamond lattice unit cells. *J Mech Behav Biomed Mater* 2014;34:106-115.

14. Van Bael S, Chai YC, Truscello S, Moesen M, Kerckhofs G, Van Oosterwyck H, Kruth JP, Schrooten J. The effect of pore geometry on the in vitro biological behavior of human periosteum-derived cells seeded on selective laser-melted Ti6Al4V bone scaffolds. *Acta Biomaterialia* 2012;8:2824-34.
15. Kolan KCR, Leu MC, Hilmas GE, Brown RF, Velez M. Fabrication of 13-93 bioactive glass scaffolds for bone tissue engineering using indirect selective laser sintering. *Biofabrication* 2011;3:025004.
16. Kolan KCR, Leu MC, Hilmas GE, Velez M. Effect of material, process parameters, and simulated body fluids on mechanical properties of 13-93 bioactive glass porous constructs made by selective laser sintering. *J Mech Behav Biomed Mater* 2012;13:14-24.
17. Kokubo T, Takadama H. How useful is SBF in predicting in vivo bone bioactivity? *Biomaterials* 2006;27(15):2907-2915.
18. Taha A. K3DSurf [Internet]. [cited 2014 Jan 30]. Available from: <http://k3dsurf.sourceforge.net/>.
19. Carter DR, Hayes WC. Bone compressive strength: the influence of density and strain rate. *Science* 1976;194:1174-1176.
20. Sun W, Starley B, Nam J, Darling A. Bio-CAD modeling and its applications in computer-aided tissue engineering. *Computer-Aided Design* 2005;37:1097-1114.
21. Sun W, Darling A, Starley B, Nam J. Computer-aided tissue engineering: overview, scope and challenges. *Biotechnol Appl Bioc* 2010;39:29-47.
22. Hutmacher D, Sittinger M, Risbud M. Scaffold-based tissue engineering: rationale for computer-aided design and solid free-form fabrication systems. *Trends Biotechnol* 2004;22:354-362.
23. Murphy CM, Haugh MG, O'Brien FJ. The effect of mean pore size on cell attachment, proliferation and migration in collagen-glycosaminoglycan scaffolds for bone tissue engineering. *Biomaterials* 2010;31:461-466.
24. Ryshkewitch R. Compression strength of porous sintered alumina and zirconia. *J Am Ceram Soc* 1953;36(2):65-68.
25. Duckworth W. Discussion of Ryshkewitch's paper. *J Am Ceram Soc* 1953;36(2):68.
26. Rice RW. Comparison of stress concentration versus minimum solid area based mechanical property-porosity relations. *J Mater Sci* 1993;28:2187-90.
27. Hattiangadi A, Bandyopadhyay A. Strength degradation of nonrandom porous ceramic structures under uniaxial compressive loading. *J Am Ceram Soc* 2000;83(11):2730-36.

28. Doiphode ND, Huang T, Leu MC, Rahaman MN, Day DE. Freeze extrusion fabrication of 13-93 bioactive glass scaffolds for bone repair. *J Mater Sci: Mater Med* 2011;22:515-523.
29. Fu Q, Saiz E, Tomsia AP. Direct ink writing of highly porous and strong glass scaffolds for load-bearing bone defects repair and regeneration. *Acta Biomater* 2011;7:3547-3554.

III. *IN VITRO* ASSESSMENT OF LASER SINTERED BIOACTIVE GLASS SCAFFOLDS WITH DIFFERENT PORE GEOMETRIES

Krishna C. R. Kolan^a, Albin Thomas^a, Ming C. Leu^a, Gregory E. Hilmas^b

^aDepartment of Mechanical and Aerospace Engineering, Missouri University of Science and Technology, Rolla, MO 65409, USA

^bDepartment of Materials Science and Engineering, Missouri University of Science and Technology, Rolla, MO 65409, USA

ABSTRACT

Purpose: The pore geometry of scaffolds intended for use in bone repair is one of the most important parameters used to determine the rate of bone regeneration. The purpose of this paper is to utilize the selective laser sintering (SLS) process to fabricate scaffolds with complex pore shapes and investigate the effects of pore geometry *in vitro*.

Design/Methodology/Approach: Scaffolds with five different architectures, having ~50% porosity, were fabricated with silicate (13–93) and borate (13–93B3) based bioactive glasses using the SLS process. An established late-osteoblasts/early-osteocytes cell line was used to perform cell proliferation tests on the scaffolds. The cell-seeded scaffolds were incubated for 2, 4, and 6 days followed by MTT assay to quantify the metabolically active cells.

Findings: The results indicated that the cells proliferate significantly more on the scaffolds which mimic the trabecular bone architecture compared to traditional lattice structures. The surface roughness of the SLS fabricated scaffolds drives the initial cell proliferation which is followed by curvature-driven cell proliferation.

Originality/Value: There have been very few studies on the effects of pore geometry on tissue growth and the existing reports do not provide clear indications. Instead of using

bio-polymer or titanium based scaffolds, we use bioactive glass scaffolds. The results obtained from our study add to the understanding of the effect of pore geometry on cell proliferation, which is based on the experimental data and analysis of the scaffolds' surface curvature.

Keywords: Selective laser sintering, Bioactive glass, Scaffold, Bone repair, Biological analysis and testing

1. INTRODUCTION

The discovery of Bioglass[®] by Prof. Hench in 1969 has led to active research interest in the field of bioactive materials in the past four decades (Hench and Wilson, 1993; Hench, 2006). Bioglass[®] is a commercially available bioactive glass containing mainly SiO₂, Na₂O, and CaO. Over the years, other beneficial elements were added to the base ternary system and the weight percentage of the elements has changed to develop new glasses which offer excellent bioactive characteristics compared to glass-ceramics or ceramics (Rahaman *et al.*, 2011). 13-93 glass is a silicate based bioactive glass which is FDA approved and has a relatively high SiO₂ content compared to 45S5 glass. Although the rate of degradation decreases due to the higher SiO₂ content, 13-93 glass has been shown to have superior mechanical properties, promote growth and differentiation of osteoblasts *in vitro* and bone growth *in vivo* for repair of a critical size bone (Brown *et al.*, 2008; Velez *et al.*, 2012; Liu *et al.*, 2013). The molar concentration of SiO₂ in 13-93 glass has also been replaced by B₂O₃ in the 13-93B3 glass formulation. Borate based glasses are chemically less durable than silicate based glasses, and therefore degrade at a faster rate and allows faster bone formation (Jung, 2012). Borate based bioactive glasses not only bond to the surrounding hard tissue but are also known to bond with soft tissues (Jung, 2012). Table 1 shows the compositions of borate based 13-93B3 bioactive glass versus silicate based 13-93 bioactive glass. The original Bioglass[®] formulation by Prof. Hench, termed 45S5 glass, is also presented for comparison.

Porosity, pore size, and pore geometry are some of the important aspects of a scaffold for bone repair and they affect material degradation and mechanical properties. Although porosity and pore size can be controlled using extrusion based additive

manufacturing (AM) processes, such as Freeze-form Extrusion Fabrication (Doiphode *et al.*, 2011) or Robocasting (Michna *et al.*, 2005; Fu *et al.*, 2011; Liu *et al.*, 2013), these processes provide only limited control over the pore geometry in fabricating porous parts because of their layer-by-layer filament deposition procedures. In comparison, powder-bed based AM techniques such as selective laser sintering (SLS) or selective laser melting (SLM) provide flexibility in fabricating porous parts with complex pore geometries and lattice structures as they do not require support structures during part fabrication, which allows for better control of part geometry at a microstructural level (10's of microns). It has been previously shown that 13-93 glass scaffolds fabricated by the SLS process provide good mechanical properties and preferable surface morphology for cell proliferation (Kolan *et al.*, 2011; 2012). Investigation of the effects of pore geometry on the mechanical properties of scaffolds, and their degradation behavior when immersed in simulated body fluid, suggested that pore geometry significantly affects the scaffold's mechanical properties at lower porosities compared to at higher porosities (Kolan *et al.*, 2013). The technical literature contains only limited studies on the effect of pore geometry on cell proliferation. Some of the studies indicate that the cells react to the local curvature of the pore and the permeability of the implant *in vivo* (Rumpler *et al.*, 2008; Mitsak *et al.*, 2011). Additionally, more recent studies have indicated that a complex pore geometry for the scaffold aids in achieving good cell seeding efficiency (Melchels *et al.*, 2010; Sobral *et al.*, 2011). Overall, it is still unclear to the scientific community as to how pore geometry affects tissue growth. Therefore, AM processes provide an opportunity to investigate the effects of scaffold pore geometry *in vitro*.

In the current work, we investigated the effects of pore geometry in the bioactive glass scaffolds on cell proliferation in a static cell culture. Scaffolds made with 13-93 and 13-93B3 glasses were fabricated with ~50% porosity using five different pore geometries. The fabricated scaffolds were seeded with bone cells and incubated at ~37°C for 2, 4, and 6 days followed by MTT assays to quantify the metabolically active cells. Section 2 describes the materials and methods used for this study. Section 3 presents and discusses the cell proliferation results obtained for the 13-93 and 13-93B3 scaffolds.

2. MATERIALS AND METHODS

2.1. FABRICATION OF SCAFFOLDS

13-93 and 13-93B3 bioactive glasses (prepared by Mo-Sci Corp., Rolla, MO) with an average particle size of 12 μm (d_{50} – 50% of the particles are less than 12 μm) and d_{90} of 30 μm were used in this research. Particle size distributions were obtained using a laser diffraction-based particle size analyzer (S3500, Microtrac Inc., Largo, FL). The glass particles were mixed with stearic acid as the sole binder ($\text{C}_{18}\text{H}_{36}\text{O}_2$, grade HS, Acros Organics, Morris Plains, NJ) and dry ball-milled for 8 hrs with ZrO_2 milling media to obtain the feedstock powder for the SLS machine. A binder content of 15% by weight was used for this purpose as this quantity provides the best possible results and is based on a previous study of SLS using 13-93 bioactive glass (Kolan *et al.*, 2012). The fabrication experiments were carried out on a commercial DTM Sinterstation 2000 machine. The effect of SLS parameters on fabricating scaffolds using stearic acid binder and bioglass powder has been investigated in our previous work. The same set of parameters (laser power – 5 W, scan speed – 508 mm/s, scan spacing – 0.23 mm, layer thickness – 0.076 mm) were adopted for the current study. The fabricated green parts were post-processed in a three-stage programmable air furnace (Vulcan Benchtop Furnace, York, PA). The following heat treatment schedule was used for this study: de-binding at a heating rate of 0.1°C/min to 550°C; heating rate increased to 1°C/min until a final sintering temperature of 570°C with a 1 hour hold for 13-93B3 scaffolds (700°C and 1 hour hold for 13-93 scaffolds) and then the furnace was turned off and allowed to cool naturally to room temperature. Optical microscopy was used to measure the pore sizes and dimensions of the sintered scaffolds. Scaffolds measuring 1 cm x 1 cm and ~3 mm

thick containing at least two rows of the lattice unit were used in the experiments so that the effect of pore geometry could be investigated. The scaffolds were ultrasonically cleaned in distilled water 3 times for 5 minutes each, followed by a similar cleaning procedure using ethyl alcohol. 13-93B3 scaffolds were only cleaned with ethyl alcohol as they are known to be highly reactive with water. The scaffolds were then dry-heat sterilized overnight at $\sim 200^{\circ}\text{C}$ before using them for cell proliferation tests.

2.2. CELL PROLIFERATION TESTS

The established MLO-A5 line of mouse late-osteoblast, early-osteocyte cells was used as a model for the *in vitro* tests to determine cell growth (Kato *et al.*, 2001). The cells were cultured in phenol red free α -MEM medium supplemented with 5% fetal bovine serum and 5% new born calf serum (Life Technologies, Grand Island, NY). Scaffolds were placed on a sterilized teflon sheet and seeded with 80,000 MLO-A5 cells suspended in 40 μl of complete medium. After a 2 h incubation to allow cell attachment, the scaffolds with attached cells were transferred to a 12-well plate with 2 ml of complete medium per well and incubated at 37°C in a humidified atmosphere of 5% CO_2 . The media was replaced every two days during the incubation period. The cell-seeded scaffolds were placed in a medium containing the tetrazolium salt MTT (50 μg per 250 μl of medium) for the last 4 h of incubation to permit visualization of metabolically active cells. The samples were rinsed with phosphate buffered saline (PBS) at the conclusion of the incubation period and blotted dry. The insoluble purple formazan, which is the product of mitochondrial MTT metabolism, was then extracted from the scaffolds with 2.0 ml of ethyl alcohol and measured at a wavelength of 570 nm using a spectrophotometer (Evolution 300 UV-Vis, Thermo Scientific, Bannockburn, IL).

2.3. STATISTICAL ANALYSIS

At least three samples in each set (2, 4, and 6 days) were used for cell proliferation tests, and the absorbance data collected from the spectrophotometer is reported as the mean \pm SD. Analysis for differences in absorbance after the incubation period and among different architectures was performed using one-way ANOVA with Tukey's post hoc test. Differences were considered significant for $P < 0.05$.

3. RESULTS AND DISCUSSION

3.1. DESIGN AND FABRICATION OF 13–93 AND 13–93B3 SCAFFOLDS

The CAD models of the repeatable units of the five architectures considered in this work are shown in Figure 1(a). The first unit cube, termed as a “cubic” architecture, is modeled using solid tubular structures which are perpendicular to each other and running in the x, y, and z directions. The second unit cube is formed by subtracting a sphere from a solid cube and is termed as a “spherical” pore architecture based on the geometry of the pore formed in the design. The third unit cube is formed by diagonally joining the corners of a unit cube with tubular structures and is termed the “X” architecture. These three architectures could be termed as typical and frequently used designs in most of the AM techniques to manufacture scaffolds. The fourth and fifth are “diamond” and “gyroid” architectures, which are based on the freeform surface and try to mimic the trabecular architecture of bone. More about the scaffold architectures, fabrication, and their mechanical properties can be found elsewhere in the literature (Kolan *et al.*, 2013). The fabricated scaffolds, after binder burnout and sintering, are shown in Figure 1(b) as representative specimens from each of the five architectures in the same order as shown in Figure 1(a). All the scaffolds shown in Figure 1(b) have a measured porosity of ~50%. The scaffolds were cut to about ~3 mm thick such that at least two rows of repeatable unit cells would be available to investigate the cell proliferation using the *in vitro* assessment.

3.2. CELL PROLIFERATION ON 13–93 SCAFFOLDS

Figure 2(a) shows a schematic of the static cell seeding on the scaffolds and how they were maintained in a 12-well cell culture plate. At the time of cell seeding, all of the

cell suspension volume applied to the scaffolds adhered to the samples since no suspension was observed on the teflon sheet after the scaffolds were aseptically transferred to the 12-well plate. Optical images of cell-seeded scaffolds with the five different architectures, and incubated with MTT during the last 4 hours of incubation for intervals of 4 and 6 days, are shown in Figure 2(b). The relative intensity of purple formazan staining on these scaffolds was found to increase with the duration of incubation. This is an indication of metabolically active cells undergoing vigorous growth on the scaffolds. The higher cell density (based on the purple color intensity) on the scaffolds with gyroid and diamond architectures, in comparison to the scaffolds with cubic, spherical and X architectures, can be observed from the optical images of the scaffolds after 4 days of incubation. The scaffolds with the diamond architecture were completely covered with metabolically active cells after 6 days of incubation. To quantify the results, the measured absorbance of the amount of formazan product of mitochondrial metabolism that was recovered from the cell-seeded scaffolds labeled with MTT is plotted in Figure 3.

The absorbance values plotted in Figure 3 for different scaffolds after 2, 4, and 6 days of incubation indicate the number of metabolically active cells on the scaffold, thereby directly corresponding to the amount of cell proliferation. To understand the cell proliferation trends from 2 to 4 days, it can be observed from Figure 3 that all the scaffolds provide significant cell proliferation except the scaffold with the X architecture. Further, the diamond and gyroid scaffolds show higher significance ($p < 0.005$) in comparison to the cubic and spherical scaffolds. Whereas the cell proliferation from 4 to 6 days was significant for the gyroid and diamond architecture scaffolds ($p < 0.01$), the

increase in cell proliferation for the other scaffolds was not significant. These results indicate that although the cubic and spherical scaffolds provide significant growth up to 4 days, the gyroid and diamond scaffolds provide significant growth up to 6 days of incubation, and the scaffold designed with the X architecture provides the least amount of cell growth. To interpret the results among the scaffolds with different architectures based on their incubation period, no significant difference was noticed after 2 days of incubation as the scaffolds have similar values of absorbance. However, the differences were observed after 4 and 6 days of incubation. After 4 days of incubation, the scaffolds having the diamond and gyroid architectures offered significantly higher cell proliferation ($p < 0.05$) in comparison to the X scaffolds. However, this difference was not significant in comparison to the cubic and spherical scaffolds. After 6 days of incubation, the cell proliferation on the diamond and gyroid scaffolds further improved in significance in comparison to the X scaffolds (from $p < 0.05$ after 4 days to $p < 0.005$ after 6 days). Also, the cell proliferation on the diamond scaffolds was significantly higher than the cubic and spherical scaffolds (with no significant difference among them after 4 days, changing to significant with $p < 0.05$ after 6 days).

3.3. CELL PROLIFERATION ON 13–93B3 SCAFFOLDS

The average absorbance value of the formazan extracted after 2 days of incubation from the 13-93B3 scaffolds was ~0.3 without any significant difference among the scaffolds with different architectures. In comparison, the absorbance values representing the cell growth on 13-93 scaffolds after 2 days was ~0.4 (Figure 3). The cell proliferation results on the 13-93B3 scaffolds indicate that the amount of formazan recovered from the scaffolds after 4 and 6 days of incubation was decreasing, which was

in sharp contrast to the result observed with the 13-93 scaffolds. Figure 4 shows the comparison of the absorbance values of the formazan product recovered from 13-93 and 13-93B3 scaffolds. The absorbance values in almost all the cases after 4 and 6 days were measured to be ~ 0.2 or less, which is too low for the result to be significant.

The results of *in vitro* assessment of borate based glasses reported in the literature are mixed. There have been some reports on the cytocompatibility of the borate glass and the osteogenic differentiation of the human mesenchymal stem cells (Marion *et al.*, 2005). There have been other studies which reported a reduction in the absorbance value with an increase in the boron ion concentration in the cell culture media (Fu *et al.*, 2009). The reduction of metabolically active cells after 4 and 6 days in our study (Figure 4) may be due to the fact that an increase in the boron ion concentration leads to an increase in the pH value of the culture media (pH ~ 9). Such an environment could drastically affect the growth of cells. It should be noted that this result was observed even after replacing the media every day for the 13-93B3 scaffolds in order to reduce the likelihood of a change in pH. In comparison, the media for 13-93 scaffolds was replaced every other day. Though the *in vitro* assessment of the 13-93B3 scaffolds showed poor cell survival rates, because of the toxicity attributed to boron ion release and its concentration, the results could be regarded as a false negative based on the *in vivo* assessment of the borate glasses which has been shown to demonstrate markedly faster bone growth and healing, as reported in the literature (Jung, 2012). In fact, borate glasses have also been shown to even promote angiogenesis and healing in difficult-to-treat soft tissue wounds in diabetic patients (Jung, 2012). The investigation of the effect of pore geometries in bone growth using the 13-93B3 scaffolds *in vivo* will be a subject of our future work.

3.4. EFFECT OF PORE GEOMETRY ON CELL PROLIFERATION

Apart from the differences in the cell proliferation based on the material used to fabricate the scaffolds, the surface roughness of the scaffolds, which is a characteristic of the SLS process and is irrespective of the geometry, could also affect the way cells proliferate on the scaffolds. Our *in vitro* assessment results indicated that during the initial 2 days of incubation, the difference in the amount of cell proliferation among the scaffolds with different pore geometries did not exist and became significant only after 4 and 6 days. This could be due to the rough surface of all of the scaffolds fabricated by the SLS process. Figure 5a shows a scanning electron microscopy (SEM) image of a strut with rough edges due to the layer-by-layer fabrication process. Another SEM image of the surface area surrounding a pore on the scaffold, irrespective of the material and scaffold pore geometry, is shown in Figure 5b. This amount of surface roughness could provide a favorable attachment surface for seeded cells on SLS-based scaffolds. In fact, at the time of cell seeding, all of the cell suspension volume applied to the scaffolds adhered to the samples and no suspension was observed on the teflon sheet after the scaffolds were aseptically transferred to the 12-well plate (100% seeding efficiency). Therefore, during the initial days of incubation, the cells would proliferate on the rough surface of the scaffold as shown in the schematic in Figure 5c. This could be the reason for not having any significant differences among the different architectures after seeding all the scaffolds with an equal number of cells and 100% seeding efficiency. The effects of pore geometry would start to prevail only after the rough surface is covered by the cells, i.e., after 4 and 6 days.

The effect of pore geometry on tissue growth and the biochemical signals between cells, as well as how the cells react to the radius of curvature of the scaffold, is still a subject of investigation to the scientific community (Rumpler *et al.*, 2007; 2008; Ripamonti *et al.*, 2012; Van Bael *et al.*, 2012). While some studies have reported that tissue growth relates to curvature, other studies found no effect of curvature on tissue growth; and most of the studies are speculative in nature. In order to comprehend the differences in cell proliferation among the scaffolds in this study, the internal surface area per unit volume was calculated for the scaffolds with different pore geometries, based on their CAD files, since a larger surface area translates to more area for cells to proliferate on the surface. The value for the X architecture (0.7 mm^{-1}) was much lower in comparison to the other architectures (1.4 for cubic, 1.9 for gyroid, and 1.5 for spherical and diamond), and it reflects in the cell proliferation results as the X scaffold offered no significant cell growth (Figure 3). However, the internal surface area per volume alone does not explain the differences in the cell proliferation among all of the scaffolds. Though the scaffolds with spherical and diamond architecture have the same value of internal surface area per volume, the cell proliferation results are in sharp contrast in that the cells seeded on the scaffolds with the diamond architecture proliferate significantly more in comparison to the spherical scaffolds. Therefore, the perimeter of a unit cell is plotted with respect to the thickness (height) of the unit cell to understand the changes in the surface area of a unit cell rather than the overall surface area. Figure 6 shows the variation in the perimeter of the cross section of a unit cell along the thickness, for all five architectures. As the length of unit cell is not uniform among the different architectures, the z height is divided by the unit cell length to provide the z value, which varies from 0

to 1 corresponding to the start and end of the unit cell thickness. Similarly, the perimeter values are also converted to ratios based on the maximum perimeter value for the corresponding unit cell. The curvature of the internal surface could be understood from the variation of the perimeter of the unit cell for different architectures. Among the scaffolds, the perimeter profile of the diamond architecture resembles a trigonometrical function (sine/cosine) with more frequent changes in sign (positive to negative and vice versa) to the slope of the curve whereas the changes to the slope of the curve are not drastic for the other architectures. Such frequent and drastic changes to the slope of the perimeter profile suggest a larger curvature for the unit cell, which offers a higher cell proliferation, as observed from our results (Figure 3).

The change in slope of the perimeter ratio vs. z-value graph qualitatively indicates the curvature of the unit cell. For an inclusive interpretation, and in an effort to quantify the results, the profile graphs for each of the scaffold types shown in Figure 6 were fit with smoothing splines (Matlab) to quantify the variation of slope and curvature of the unit cells. Figure 7 shows the curvature graphs for each of the scaffold types, calculated using the following equation:

$$\kappa = \frac{f''}{(1 + (f')^2)^{3/2}} \quad (1)$$

κ - curvature; f'' - second derivative; f' - first derivative;

A relatively slow change in slope or a constant slope of the perimeter profile would suggest small or no curvature which appears to be less beneficial for cell proliferation,

especially in a static cell culture condition where the nutrient flow is limited and the only external stimulus for the cells to proliferate could be the curvature. In the case of diamond and gyroid architectures, a frequent change in curvature might allow for better cell proliferation in the static cell culture conditions. Among the latter two, the diamond architecture provides a high curvature in comparison to the gyroid architecture (the highest curvature of ~ 400 vs. ~ 100) and this could be the reason for the diamond architecture providing the highest cell proliferation among all the scaffold types. A table with the summation of the absolute values of the curvature for all scaffold types is also shown in Figure 7. Therefore, it can be stated that a preferable porous scaffold for tissue engineering applications should provide the necessary surface roughness for initial cell attachment, and a high surface curvature for improved cell proliferation.

4. CONCLUSIONS

The *in vitro* assessment in this study indicates that bioactive glass scaffolds fabricated by the selective laser sintering process provide the necessary surface roughness for the initial phase of incubation for cell attachment. The cell proliferation study shows the effectiveness of SLS produced gyroid and diamond architectures in providing sustained cell proliferation for 6 days of incubation compared to other scaffold architectures (cubic, spherical, and X architectures) which did not provide significant cell growth after 4 days of incubation. Our static cell culture experimental results and analysis indicate that a frequent change in the surface curvature of the scaffold combined with a higher surface curvature allows for improved cell proliferation *in vitro*.

Table 1. Compositions (in wt.%) of 13-93 and 13-93B3 glasses compared to 45S5 glass.

	SiO ₂	P ₂ O ₅	CaO	MgO	Na ₂ O	K ₂ O	B ₂ O ₃
45S5	45	6	24.5	-	24.5	-	-
13-93	53	4	20	5	6	12	-
13-93B3	-	3.7	18.5	4.6	5.5	11.1	56.6

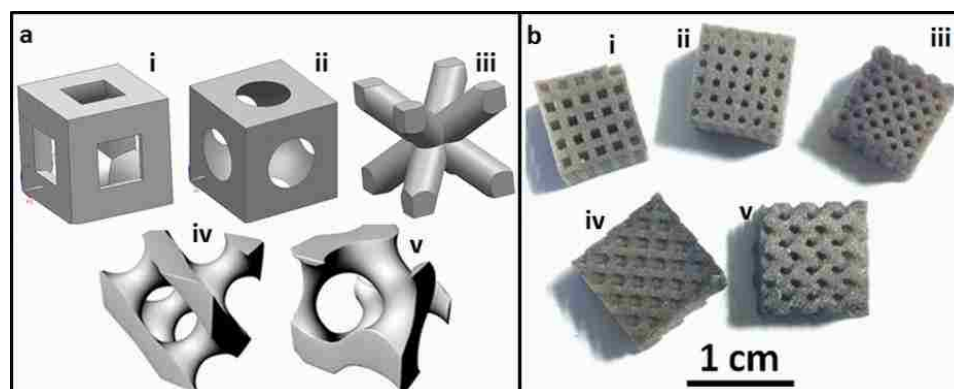


Figure 1. (a) CAD models of the repeatable units of five architectures: (i) cubic, (ii) spherical, (iii) X, (iv) diamond, and (v) gyroid; (b) 13-93B3 scaffolds produced from the five different architectures, after sintering.

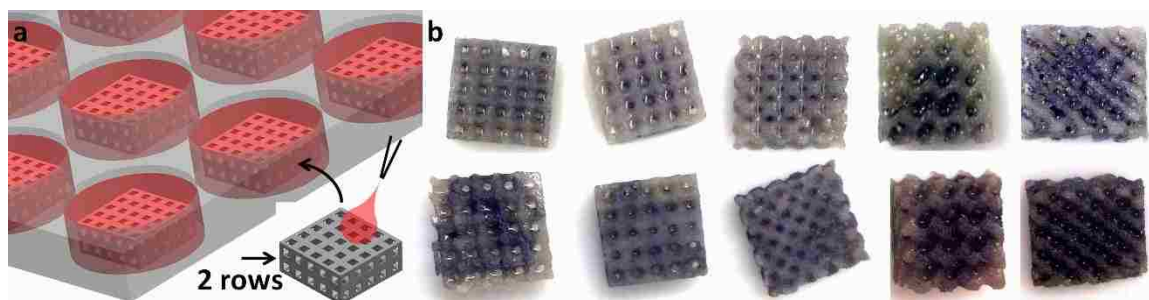


Figure 2. (a) Schematic of the static cell seeding on the scaffold with at least two rows of repeating units. The cell seeded scaffolds were later transferred to a 12-well cell culture plate, (b) Optical images showing the MTT labeling of MLO-A5 cells on the scaffolds (L-R: cubic, spherical, X, gyroid and diamond) after cell culture intervals of 4 days (top row) and 6 days (bottom row).

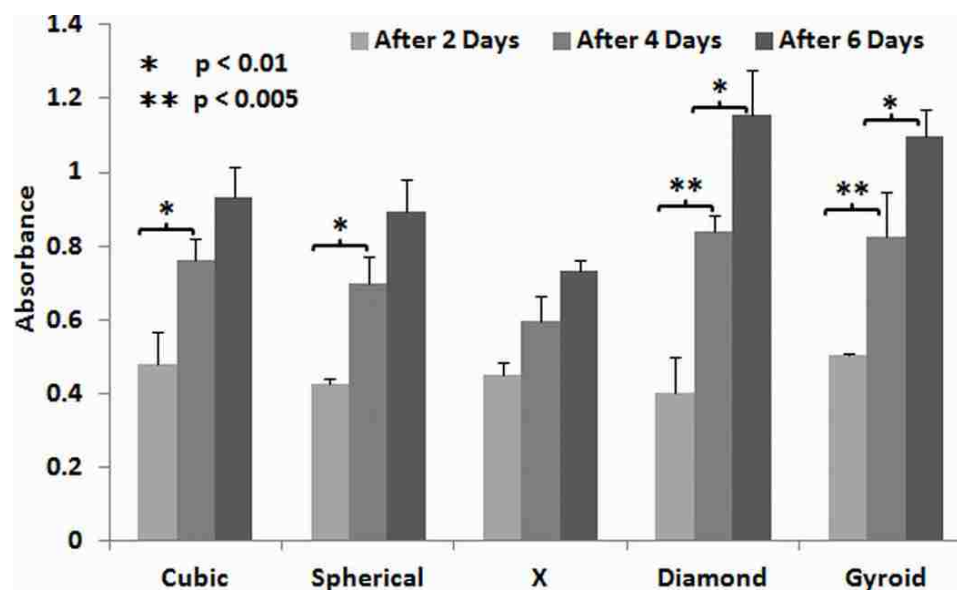


Figure 3. The absorbance values representing the measurement of cell growth plotted for all the scaffolds after 2, 4, and 6 days of incubation. Diamond and gyroid architectures show better overall cell proliferation compared to the other architectures.

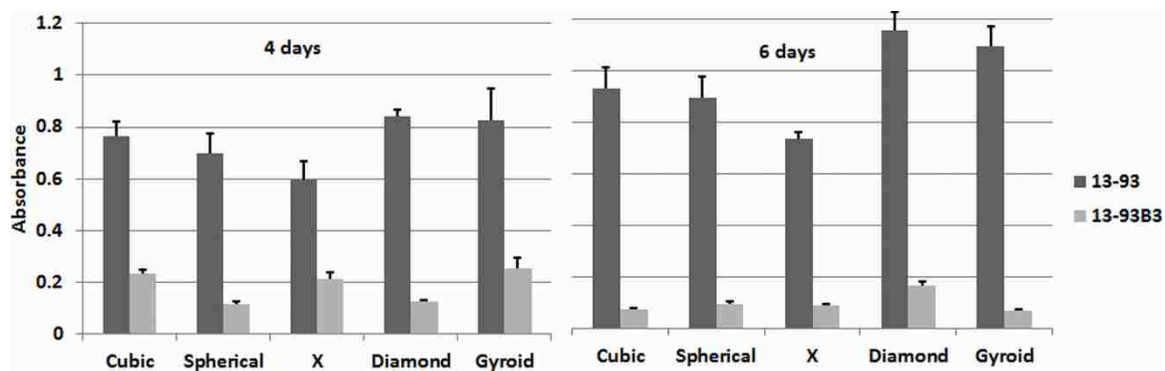


Figure 4. Comparison of the absorbance values for 13-93 and 13-93B3 scaffolds after 4 and 6 days of incubation. The graphs indicate the reduced number of metabolically active cells on the 13-93B3 scaffolds compared to the 13-93 scaffolds.

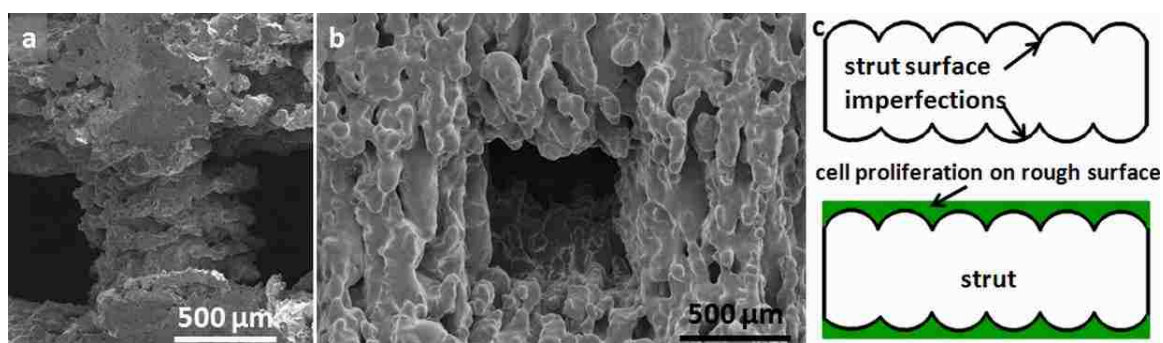


Figure 5. (a) The surface of the strut exhibiting layered fabrication in the SLS process, (b) a typical surface of the SLS scaffold, (c) schematic showing the proliferation of cells on the rough surface during the initial incubation period.

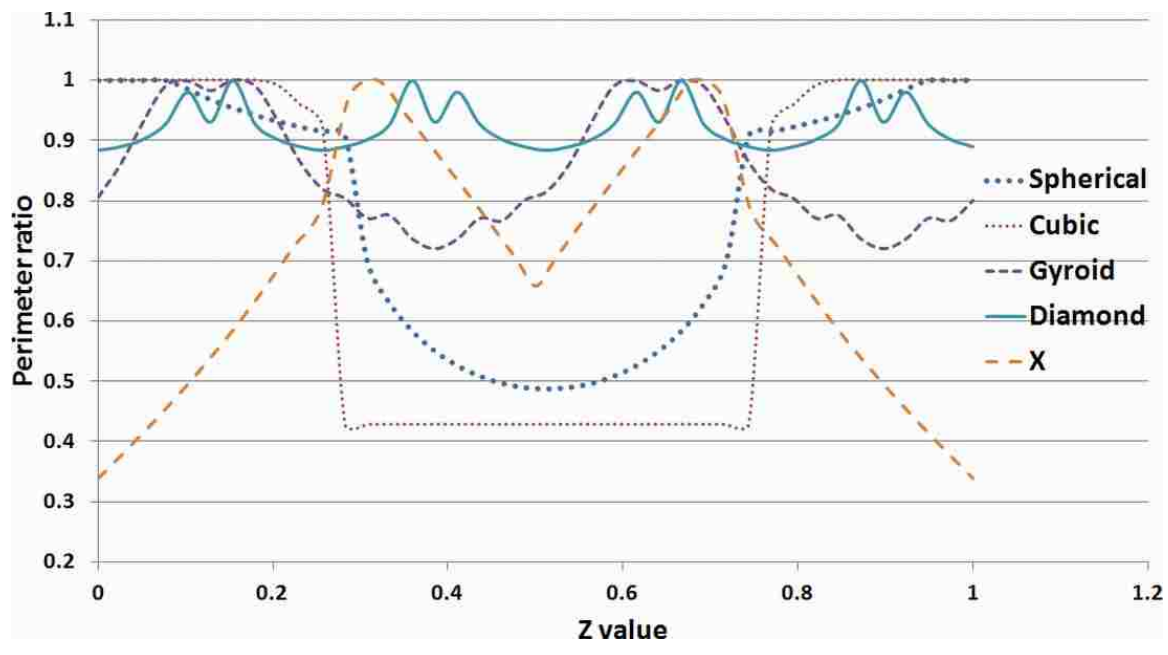


Figure 6. The variation of the perimeter through the length of the unit cell.

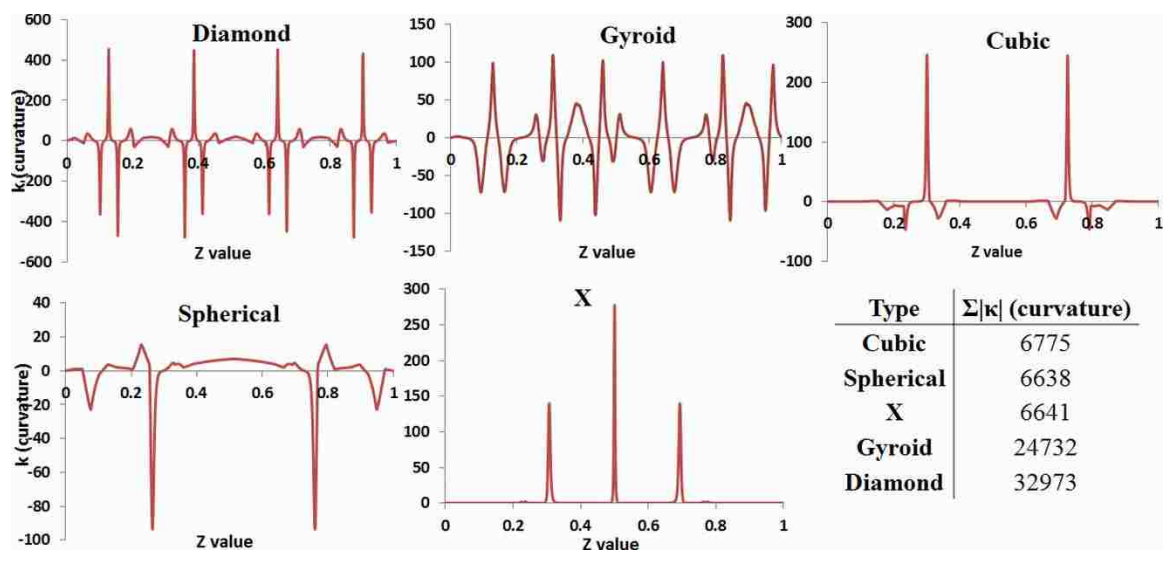


Figure 7. The curvature plots of the perimeter ratio vs. z-value graphs for different architectures and the summation of the absolute values of the curvature.

REFERENCES

- Brown, R.F., Day, D.E., Day, T.E., Jung, S., Rahaman, M. and Fu, Q. (2008), "Growth and differentiation of osteoblastic cells on 13–93 bioactive glass fibers and scaffolds", *Acta Biomaterialia*, Vol. 4 No.1, pp. 387-396.
- Doiphode, N., Huang, T., Leu, M., Rahaman, M. and Day, D. (2011), "Freeze extrusion fabrication of 13-93 bioactive glass scaffolds for bone repair", *Journal of Materials Science: Materials in Medicine*, Vol. 22, pp. 515-523.
- Fu, H., Fu, Q., Zhou, N., Huang, W., Rahaman, M.N., Wang, D. and Liu, X. (2009), "In vitro evaluation of borate-based bioactive glass scaffolds prepared by a polymer foam replication method", *Materials Science and Engineering C*, Vol. 29 No.7, pp. 2275–2281.
- Fu, Q., Saiz, E. and Tomsia, A.P. (2011), "Direct ink writing of highly porous and strong glass scaffolds for load-bearing bone defects repair and regeneration", *Acta Biomaterialia*, Vol 7 No.1, pp. 3547-3554.
- Hench, L.L. and Wilson, J. (1993), *An Introduction to Bioceramics*, World Scientific Publishing Co. Pte. Ltd., Singapore, pp 47.
- Hench, L.L. (2006), "The story of bioglass", *Journal of Materials Science: Materials in Medicine*, Vol. 17, pp. 967–978.
- Jung, S.B., (2012), "Borate bioactive glasses", in Jones, J., and Clare, A.G. (Eds.), *Bioglasses: An introduction*, John Wiley & Sons, Inc., NJ, USA, pp. 75.
- Kato, T., Boskey, A., Spevak, L., Dallas, M., Hori, M. and Bonewald, L. (2001), "Establishment of an osteoid preosteocyte-like cell MLO-A5 that spontaneously mineralizes in culture", *Journal of Bone and Mineral Research*, Vol. 16, pp. 1622-1633.
- Kolan, K.C.R., Leu, M.C., Hilmas, G.E., Brown, R.F. and Velez, M. (2011), "Fabrication of 13-93 bioactive glass scaffolds for bone tissue engineering using indirect selective laser sintering", *Biofabrication*, Vol. 3, pp. 025004.
- Kolan, K.C.R., Leu, M.C., Hilmas, G. and Comte, T. (2013), "Effect of architecture and porosity on mechanical properties of borate glass scaffolds made by selective laser sintering" in *Proceedings of the 24th Annual International Solid Freeform Fabrication Symposium*, Austin, pp. 816-826.
- Kolan, K.C.R., Leu, M.C., Hilmas, G.E. and Velez, M. (2012), "Effect of material, process parameters, and simulated body fluids on mechanical properties of 13-93 bioactive glass porous constructs made by selective laser sintering", *Journal of the Mechanical Behavior of Biomedical Materials*, Vol. 13, pp. 14-24.

- Liu, X., Rahaman, M.N. and Fu, Q. (2013), "Bone regeneration in strong porous bioactive glass (13-93) scaffolds with an oriented microstructure implanted in rat calvarial defects", *Acta Biomaterialia*, Vol. 9 No. 1, pp. 4889-4898.
- Liu, X., Rahaman, M., Hilmas, G. and Bal, S. (2013), "Mechanical properties of bioactive glass (13-93) scaffolds fabricated by robotic deposition for structural bone repair", *Acta Biomaterialia*, Vol. 9 No.1, pp. 7025-7034.
- Marion, N.W., Liang, W., Liang, W., Reilly, G.C., Day, D.E., Rahaman, M.N. and Mao, J.J. (2005), "Borate glass supports the in vitro osteogenic differentiation of human mesenchymal stem cells", *Mechanics of advanced materials and structures*, Vol. 12 No. 3, pp 239-246.
- Melchels F, Barradas A, Blitterswijk C, Boer J, Feijen J and Grijpma D (2010), "Effects of the architecture of tissue engineering scaffolds on cell seeding and culturing", *Acta Biomaterialia*, Vol. 6, pp. 4208-4217.
- Michna, S., Wu, W. and Lewis, J. (2005), "Concentrated hydroxyapatite inks for direct-write assembly of 3-D periodic scaffolds", *Biomaterials*, Vol. 26, pp. 5632-5639.
- Mitsak, A., Kemppainen, J., Harris, M. and Hollister, S. (2011), "Effect of polycaprolactone scaffold permeability on bone regeneration in vivo", *Tissue Engineering Part A*, Vol. 17, pp. 1831-1839.
- Rahaman, M.N., Day, D.E., Bal, B.S., Fu, Q., Jung, S.B. and Bonewald, L.F. (2011), "Bioactive Glass in Tissue Engineering", *Acta Biomaterialia*, Vol. 7, pp. 2355-2373.
- Ripamonti U, Roden L, Renton L, Klar R and Petit J-C (2012), "The influence of geometry on bone: formation by autoinduction", *Science in Africa*.
- Rumpler, M., Woesz A, Varga F, Majubala I, Klaushofer K and Fratzl P (2007), "Three-dimensional growth behavior of osteoblasts on biomimetic hydroxylapatite scaffolds", *Journal of Biomedical Material Research Part A*, Vol. 81 No. 1, pp. 40-50.
- Rumpler, M., Woesz, A., Dunlop, J.W.C., Dongen, J.T. and Fratzl, P. (2008), "The effect of geometry on three-dimensional tissue growth", *Journal of Royal Society Interface*, Vol. 5, pp. 1173-1180.
- Sobral J M, Caridade S G, Sousa R A, Mano J F and Reis R L (2011), "Three-dimensional plotted scaffolds with controlled pore size gradients: Effect of scaffold geometry on mechanical performance and cell seeding efficiency", *Acta Biomaterialia*, Vol. 7, pp. 1009-1018.

- Van Bael, S., Chai, Y.C., Truscetto, S., Moesen, M., Kerckhofs, G., Van Oosterwyck, H., Kruth, J.-P. and Schrooten, J. (2012), "The effect of pore geometry on the in vitro biological behavior of human periosteum-derived cells seeded on selective laser-melted Ti6Al4V bone scaffolds", *Acta Biomaterialia*, Vol. 8, pp. 2824-34.
- Velez, M., Jung, S., Kolan, K.C.R., Leu, M.C., Day, D.E. and Chu, T-M.G. (2012), "In-vivo evaluation of 13-93 bioactive glass scaffolds made by selective laser sintering", in *Biomaterials Science: Processing, Properties and Applications II: Ceramic Transactions*, Vol. 237, John Wiley & Sons, Inc., NJ, USA.

SECTION

2. *IN VIVO* EVALUATION OF LASER SINTERED BORATE BIOACTIVE GLASS SCAFFOLDS WITH CUBIC AND DIAMOND PORE GEOMETRIES

2.1. INTRODUCTION

It is long known that the bioactive glasses such as 45S5 glass bond with hard and soft tissues [1]. Over the past decades, researchers have developed bioactive glasses with different chemical compositions and degradation rates suitable for repairing both hard and soft tissues [2]. Silicate based bioactive glasses have been shown to degrade slowly even *in vivo* because of the chemically durable SiO₂ network. In fact, a recent long-term *in vivo* evaluation of scaffolds made with a silicate based 13-93 bioactive glass reported that about half of the scaffold (unconverted glass) still remained in the defect region after 6 months [3]. Alternately, a faster degradation was reported in a recent *in vivo* study of the borate based (13-93B3) bioactive glass with most of the glass degrading in 12 weeks and a significant amount new bone formation in comparison to silicate based bioactive glasses and 45S5 glass [4]. The study also reported that the release of boron ions had no adverse effect such as inflammation and necrosis in systemic organs. The compositions of above mentioned bioactive glasses are provided in Table 2.1.

The advent of additive manufacturing (AM) technologies provides an opportunity to evaluate the performance of scaffolds made with different bioactive glasses. Some of the most widely used AM techniques for this purpose are robocasting [5], direct ink writing (DIW) [6, 7], 3D Printing (3DP) [8], and selective laser sintering (SLS) [9, 10]. Robocasting and DIW methods are extrusion based fabrication methods and provide dense filaments during the layer-by-layer fabrication process. Therefore, the mechanical

Table 2.1. Compositions (in wt.%) of 13-93 and 13-93B3 glasses in comparison to 45S5 glass.

	SiO ₂	P ₂ O ₅	CaO	MgO	Na ₂ O	K ₂ O	B ₂ O ₃
45S5	45	6	24.5	-	24.5	-	-
13-93	53	4	20	5	6	12	-
13-93B3	-	3.7	18.5	4.6	5.5	11.1	56.6

properties of the glass scaffolds, especially compressive strength, are typically similar to that of the human cortical bone and the scaffolds are suitable to repair a load-bearing bone [5, 7, 11]. Whereas 3DP and SLS processes being powder-bed based AM fabrication methods, the ceramic parts fabricated using these methods are relatively less dense and, thereby, inferior mechanical properties in comparison to ceramic parts fabricated by extrusion based methods [12-14]. However, these powder-bed based AM methods have the advantage of fabricating scaffolds with complex pore geometries which mimic the trabecular bone architecture. The degradation of an implant is typically dependent on the choice of bioactive glass utilized in the fabrication process. However, recent studies indicate that the pore geometry could also potentially affect the degradation rate of the scaffold when they are fabricated with the same bioactive glass [15]. The effects of pore size and permeability of the scaffolds on new tissue growth *in vivo* have been studied in the past [16, 17]. Though there does not seem to have a common opinion on the optimum pore size, the results indicate that a smaller pore size and larger pore volume increases the pore closure and new tissue formation [18, 19]. The pore geometry of the implant is getting attention lately as it has been shown to influence cell

proliferation [20-22]. However, there are only a few studies and hence limited knowledge on the influence of pore geometry on new tissue formation.

In the present study, porous scaffolds made with borate based (13-93B3) bioactive glass using the SLS process having two different pore geometries were implanted in a rat calvarial defect model. The objective of the study was to investigate the difference in bone growth among the scaffolds with different architectures, namely, cubic and diamond. The scaffolds are implanted for a time period of 6 weeks and the new bone formation in the implants was evaluated using the histomorphometric analysis.

2.2. EXPERIMENTS

2.2.1. Scaffold Preparation. 13-93B3 bioactive glass (Mo-Sci Corp., Rolla, MO) with an average particle size of 12 μm (d_{50} – 50% of the particles are less than 12 μm) were used in this research. Particle size distributions were obtained using a laser diffraction-based particle size analyzer (S3500, Microtrac Inc., Largo, FL). The glass particles were mixed with stearic acid as the sole binder ($\text{C}_{18}\text{H}_{36}\text{O}_2$, grade HS, Acros Organics, Morris Plains, NJ) and dry ball-milled for 8 hrs with ZrO_2 milling media to obtain the feedstock powder for the SLS machine. The fabrication experiments were carried out on a Sinterstation 2000 (DTM) machine, as described in our previous work [12]. The same set of parameters (laser power – 5 W, scan speed – 508 mm/s, scan spacing – 0.23 mm, layer thickness – 0.076 mm, binder content – 15% by weight) were adopted for the current study. The fabricated green parts were post-processed in a three-stage programmable air furnace (Vulcan Benchtop Furnace, York, PA). Following the fabrication, scaffolds were heated slowly (0.1°C/min) to 550°C to burnout the polymer binder, and then sintered for 1 h at 570°C (heating rate – 1°C/min), and then the furnace

was turned off and allowed to cool naturally to room temperature. The sintered scaffolds were grinded to required dimensions (~1.5 mm thick and 4.6 mm in diameter), ultrasonically washed thrice (5 minutes each) with acetone and followed by ethanol, dried in air and then heat sterilized overnight at 250°C. The scaffolds used for implantation are shown in Figure 2.1 along with the corresponding CAD models and their unit cells.

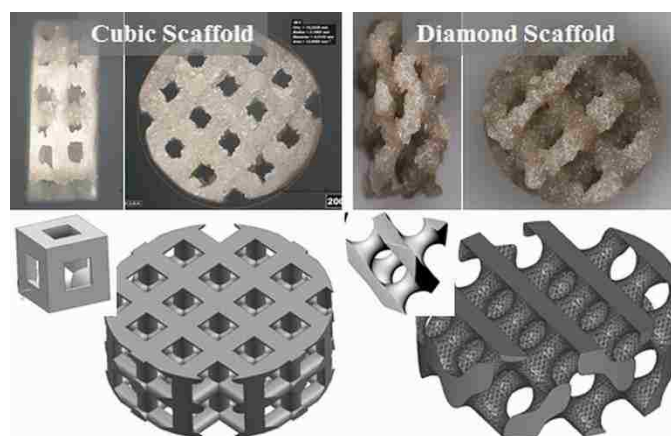


Figure 2.1. Cubic and Diamond scaffold types (top and side views) and their CAD models.

2.2.2. Animals and Surgical Procedure. All animal experimental procedures were approved by the Missouri S&T Institutional Animal Care and Use Committee. Six 12-week-old male Sprague-Dawley rats, ~350 g in body weight, were maintained in the animal care facility for 2 weeks to become acclimated to diet, water, and housing under a 12 h/12 h light/dark cycle. The rats were anesthetized with 4 ml KX mixture (Ketamine/Xylazine with 200 mg K and 20 mg X per 4 ml) at 70% of full dose (0.17 ml per 100g rat weight). The surgical area was shaved and scrubbed with sterile gauze soaked with betadine before using sterile instruments and aseptic techniques to make an

approximately 1 cm cranial skin incision on the anterior to posterior direction along the midline. The subcutaneous tissue, musculature and periosteum were dissected and reflected to expose the calvaria. A full-thickness defect measuring 4.6 mm in diameter was created in the central area of each parietal bone. A Dremel hand drill (Racine, WI) with a commercially available bit of 4.6 mm in outside diameter (ACE Surgical Supply Co. Inc, Brockton, MA) was used to create the calvarial defects under constant irrigation with 1x sterile phosphate-buffered saline (PBS) to prevent overheating of the bone and to remove the bone debris. The duramater was not disturbed. A sample size of $n = 6$ is considered for the experiments and the bone defect distribution among the two scaffold designs is shown in Table 2.2 (D – Diamond scaffold; C – Cubic scaffold).

Table 2.2. Experimental plan showing scaffold placement in rat calvarial defect.

Animal #	Left Side	Right Side
1	D	D
2	D	D
3	D	C
4	C	D
5	C	C
6	C	C

After the implantation, the skin was closed with Autoclip® wound closing system (Braintree Scientific, Inc., Braintree, MA). All animals were given 0.2 ml of penicillin

subcutaneously and ketoprofen (3 mg per kg) intramuscularly post-surgery. Animals were allowed to recover by placing them on a warm table. The condition of the surgical wound, animal activity, signs of infection and/or neurological compromise were monitored regularly. After 6 weeks, animals were sacrificed by means of CO₂ inhalation and the defect sites with surrounding bone were harvested for subsequent examination.

2.2.3. Histological Processing. The harvested samples were fixed in 10% buffered formaldehyde for ~3 days and then soaked in DI water overnight, and cut in half. One half is decalcified in Cal-Ex II simultaneous Fixative/Decalcifier (Fisher Chemical) solution and the other half is stored in 70% ethyl alcohol solution for von Kossa staining. The decalcifying solution is changed every two day during the first week and once in every 4 days for about ~4 weeks. The samples were dehydrated with a series of ethanol solutions by a microwave dehydration technique (EBSciences H2850 Microwave Processor). The microwave was set to 70% power and the sample temperature was set to ~37°C. The samples were heated for about 2.5 minutes in the microwave followed by a 12.5 minutes of idle time. The samples were then soaked in xylene solution before soaking in fluid paraffin mounting wax at 45°C overnight. After mounting the samples in wax using a paraffin mounting system (Leica EG 1150H), 5 µm thin sections of the specimens were cut and floated in a water bath at 37°C before mounting on a glass slide. Slides were stained with hematoxylin and eosin (H&E) to determine the amount of new bone tissue. Optical images of the stained sections were taken with an Olympus BX 50 microscope connected to a camera (DP70, Olympus, Japan).

2.2.4. Histomorphometric Analysis. Histomorphometric analysis was carried out using the stitched optical images (Image composite editor software) of the stained sections and the ImageJ software. The percent of the new bone formed in the defects was evaluated from the optical images. The defect area is considered as the region between two boundaries formed during the drilling process including the unconverted glass and the tissue within. The newly formed bone fibrous tissue within the defect area is outlined and measured. The area is expressed as a percentage of the total defect area.

2.2.5. Statistical Analysis. The results are presented as mean value \pm std. dev. Analysis of differences in new bone between the two scaffold groups was performed using one-way analysis of variance with Tukey's post-hoc test considering the differences to be significant for $p < 0.05$.

2.3. RESULTS AND DISCUSSION

2.3.1. New Bone Formation. Optical images of the as-harvested section from an animal implanted with cubic scaffolds along with the von Kossa and H&E stained sections are shown in Figure 2.2. Figure 2.2.(a) shows the harvested specimen (~0.5 mm thick section) after 6 weeks of implantation in rat calvarial defects. It can be observed that the bone-like tissue and fibrous tissue has completely filled in to the pores of the scaffold and the scaffold has been integrated with the surrounding bone tissue. In almost all the cases, the unconverted glass in the 13-93B3 scaffolds was observed to maintain its dark color which was seen in the as-sintered scaffolds. Interestingly, the scaffold and the actual bone region turned black after the von Kossa staining as shown in Figure 2.2.(b). The reason for this could be the faster reaction phenomenon of the 13-93B3 glass [4]. It

is known that 13-93B3 glass releases the boron and calcium ions at a higher rate in comparison to 13-93 glass, but the release of ions would also mean the presence of phosphate ions which could react with the silver nitrate solution and turn black during the von Kossa staining procedure. Also, this phenomenon could be only at the surface of the scaffold because in the H&E staining performed on the 5 μm thin section, the unconverted glass in the scaffold, fibrous tissue and the new bone can be clearly distinguished (see Figure 2.2.(c)). The magnified image shown in Figure 2.2.(i) shows the new bone formed within the scaffold. The integration of the scaffold and the boundary of the defect can be clearly observed in the magnified image shown in Figure 2.2.(ii) of the H&E staining of the section. The fibrous tissue surrounding the new bone is largely matured and have osteocytes. The purple color surrounding the glass suggests the high presence of osteoblasts which is then surrounded by the maturing fibrous tissue and eventually new bone. Interestingly, pockets of bone-marrow like features are observed inside the new bone region. As there are two different types of scaffolds made with same glass, similar porosity, and dimensions are utilized in this study, the new bone formation is calculated w.r.t the total defect area. The amount of new bone formed after 6 weeks of implantation in the cubic scaffolds was $8.6 \pm 2\%$ and in the diamond scaffolds was $9.5 \pm 1.8\%$ (results are shown in Table 2.3). The statistical analysis of the result indicated no significant difference in new bone growth based on the scaffold types considered in this study. In comparison, the new bone growth w.r.t. the total defect area (calvarial) after 12 weeks of implantation for thermally bonded 13-93B3 short fiber scaffolds was $\sim 15\%$ which was reportedly significant to that of $\sim 8\%$ for a 13-93 fiber scaffold [4]. The bone growth observed in our work is similar to the above mentioned study.

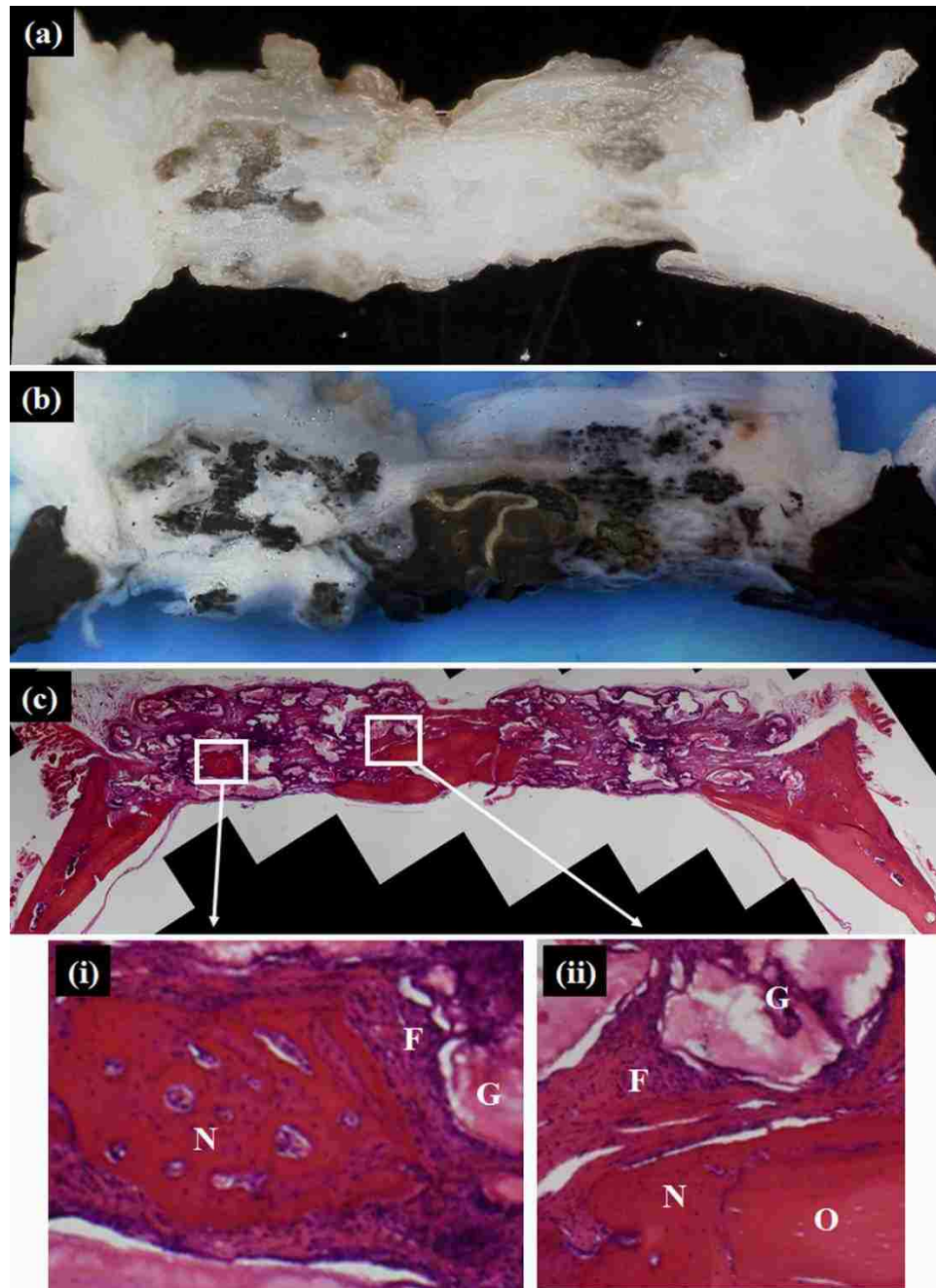


Figure 2.2. (a) Optical image of the specimen cut from the harvested specimen, (b) after von Kossa staining of the specimen, (c) after H&E staining of the specimen; also shown in inset are the magnified images of the (i) new bone formed within the scaffold, and (ii) at the boundary of the defect region; N – new bone, O – original bone, G – glass, F – fibrous tissue which is about to mature. Percentage of new bone growth w.r.t. the defect area in cubic and diamond scaffold types is shown in the graph.

Table 2.3. New bone area (in %) with respect to defect area measured from H&E stained sections for cubic and diamond scaffolds.

Sample #	Cubic	Diamond
1	11.02	11.55
2	6.3	8.92
3	8.15	6.42
4	7.1	10.96
5	9.58	6.72
6	9.45	9.63
7	5.97	10.11
8	11.86	10.9
9	7.54	9.94

Interestingly, a higher amount of bone growth of $32 \pm 13\%$ was reported for the 13-93 scaffolds fabricated using the Robocasting technique [19]. The pore size of the Robocasting printed scaffolds ($\sim 100\text{-}150\ \mu\text{m}$) was much less in comparison to the pore size of the SLS scaffolds ($\sim 500\text{-}800\ \mu\text{m}$) used in the present study and even for the fiber scaffold ($\sim 50\text{-}500\ \mu\text{m}$). It is reported by several researchers that smaller pores of $\sim 100\text{-}300\ \mu\text{m}$ in size might be favorable for an accelerated bone growth at 4 weeks of bone formation but the effect to pore size plays a limited role at 8 weeks [23]. The limitation of fabricating scaffolds with small pore sizes (less than $500\ \mu\text{m}$) using the DTM 2000 machine is owed to the laser spot diameter and is discussed elsewhere in the literature.

The objective of this study was to investigate the effects of the pore geometry on bone growth using the SLS scaffolds fabricated with the DTM Sinterstation 2000 machine. Though the difference in new bone formation is not significant between the two scaffold types, the qualitative analysis of the matured fibrous tissue (future bone) is performed for conclusive results.

2.3.2. Fibrous Tissue Formation. The common aspect of new bone formation in both scaffold types lies in the fact that the new bone formation started from the end of the defect region and then grew into the center of the scaffold region. This can be clearly observed in magnified images of H&E staining sections of diamond (Figure 2.3.(a)) and cubic (Figure 2.3.(b)) scaffolds. Apart from that, although the difference in new bone growth was not significant for cubic and diamond scaffolds, the presence of fibrous tissue (soft tissue) was remarkably different. This is shown in magnified images of the central region of stained sections (Figure 2.3). The difference was observed in the level of maturity of the fibrous tissue. While the fibrous tissue in the diamond scaffold appears to have oriented osteocytes almost about to transform to new bone, the fibrous tissue from the central region of the cubic scaffold appears more like the soft tissue similar to that of the tissue outside the defect region. This indicates that the new bone formation within the cubic scaffold would take longer time in comparison to the bone formation in the diamond scaffold. The reason for faster maturation of the fibrous tissue in the diamond could be attributed to the curved profile of the pore (magnified central region of Figure 2.3.(a)) which drives the fibrous tissue and thereby osteoblasts and osteocytes to orient and adapt to the pore geometry. Such a phenomenon was not observed in cubic scaffolds,

at least in the case of SLS scaffolds with relatively larger pore sizes ($\sim 500\text{-}800\ \mu\text{m}$) such as the ones fabricated for this study.

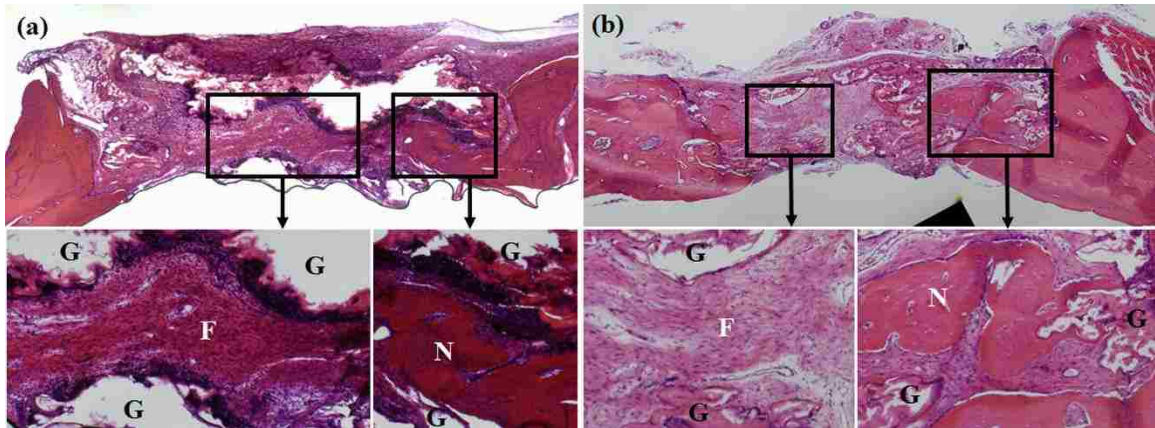


Figure 2.3. H&E stained sections of (a) Diamond scaffold, and (b) Cubic scaffold. The inset figures show almost matured fibrous tissue (about to become bone) in the defect area implanted with a diamond scaffold.

2.4. CONCLUSIONS

Scaffolds ($\sim 50\%$ porosity, $\sim 500\text{-}800\ \mu\text{m}$ pores) made with borate based 13-93B3 bioactive glass with two different pore geometries, namely, cubic, and diamond, fabricated using the selective laser sintering process showed the scope of bone formation in rat calvarial defects. The new bone formation w.r.t. complete defect area was $\sim 8.6\%$ for cubic scaffold and $\sim 9.5\%$ for diamond scaffold with no significant difference in bone growth between the scaffold types after 6 weeks of implantation. However, a higher percentage of matured fibrous tissue has been observed in the pore space of the defects implanted with diamond scaffolds in comparison to the young fibrous (soft) tissue in the cubic scaffold.

REFERENCES

1. Hench LL and Wilson J, 1993. An Introduction to Bioceramics, World Scientific Publishing Co. Pte. Ltd., Singapore, pp 47.
2. Rahaman MN, Day DE, Bal BS, Fu Q, Jung SB, Bonewald LF, 2011. Bioactive Glass in Tissue Engineering. *Acta Biomaterialia*, 7:2355-2373.
3. Lin Y, Xiao W, Liu X, Bal BS, Bonewald LF, Rahaman MN, 2015. Long-term bone regeneration, mineralization and angiogenesis in rat calvarial defects implanted with strong porous bioactive glass (13-93) scaffolds. *J. Non-Crystalline Solids*.
4. Jung SB, PhD Dissertation, Chapter 4. 2010. Missouri University of Science and Technology, Rolla, MO.
5. Liu X, Rahaman M, Hilmas G, Bal S, 2013. Mechanical properties of bioactive glass (13-93) scaffolds fabricated by robotic deposition for structural bone repair. *Acta Biomaterialia*, 9(1):7025-7034.
6. Lewis JA, Smay JE, Stuecker J, Cesarano III J, 2006. Direct ink writing of three-dimensional ceramic structures. *J Am Ceram Soc*, 89:3599-3609.
7. Fu Q, Saiz E, Tomsia AP, 2011. Direct ink writing of highly porous and strong glass scaffolds for load-bearing bone defects repair and regeneration. *Acta Biomaterialia*, 7:3547-3554.
8. Bose S, Vahabzadeh S, Bandyopadhyay A, 2013. Bone tissue engineering using 3D printing. *Mater Today*. 16(12):496-504.
9. Goodridge RD, Dalgarno KW, Wood DJ, 2006. Indirect selective laser sintering of an apatite-mullite glass-ceramic for potential use in bone replacement applications. *Proc Inst Mech Eng H*. 220:57-68.
10. Kolan KCR, Leu MC, Hilmas GE, Brown RF, Velez M, 2011. Fabrication of 13-93 bioactive glass scaffolds for bone tissue engineering using indirect selective laser sintering. *Biofabrication*. 3:025004.
11. Doiphode N, Huang T, Leu M, Rahaman M, Day D, 2011. Freeze extrusion fabrication of 13-93 bioactive glass scaffolds for bone repair. *J Mater Sci: Mater Med*. 22:515-523.
12. Kolan KCR, Leu MC, Hilmas GE, Velez M, 2012. Effect of material, process parameters, and simulated body fluids on mechanical properties of 13-93 bioactive glass porous constructs made by selective laser sintering. *J Mech Behav Biomed Mater*. 13:14-24.

13. Shirazi SFS, Gharekhani S, Mehrali M, Yarmand H, Metselaar HSC, Kadri NA, Osman NAA, 2015. A review on powder-based additive manufacturing for tissue engineering: selective laser sintering and inkjet 3D printing. *Sci. Technol. Adv. Mater.* 16(3):033502.
14. Farzadi A, Solati-Hashjin M, Asadi-Eydivand M, Osman NA, 2014. Effect of layer thickness and printing orientation on mechanical properties and dimensional accuracy of 3D printed porous samples for bone tissue engineering. *PLoS One.* 9(9):e108252.
15. Kolan KCR, Thomas A, Leu MC, Hilmas GE, 2015. In vitro assessment of laser sintered bioactive glass scaffolds with different pore geometries. *Rapid Prototyping J.* 21(2):152-158.
16. Murphy CM, O'Brien FJ, 2010. Understanding the effect of mean pore size on cell activity in collagen-glycosaminoglycan scaffolds. *Cell Adh migr.* 4(3):377-381.
17. Mitsak A, Kemppainen J, Harris M, Hollister S, 2011. Effect of polycaprolactone scaffold permeability on bone regeneration in vivo. *Tissue Engineering Part A.* 17:1831-1839.
18. Van Bael S, Chai YC, Truscetto S, Moesen M, Kerckhofs G, Van Oosterwyck H, Kruth J-P, Schrooten J, 2012. The effect of pore geometry on the in vitro biological behavior of human periosteum-derived cells seeded on selective laser-melted Ti6Al4V bone scaffolds. *Acta Biomaterialia.* 8:2824-34.
19. Liu X, Rahaman MN, Fu Q, 2013. Bone regeneration in strong porous bioactive glass (13-93) scaffolds with an oriented microstructure implanted in rat calvarial defects. *Acta Biomaterialia.* 9(1):4889-4898.
20. Rumpler M, Woesz A, Varga F, Majubala I, Klaushofer K, Fratzl P, 2007. Three-dimensional growth behavior of osteoblasts on biomimetic hydroxylapatite scaffolds. *J Biomed Mater Res A.* 81(1):40-50.
21. Rumpler M, Woesz A, Dunlop JWC, Dongen JT, Fratzl P, 2008. The effect of geometry on three-dimensional tissue growth. *J Royal Soc Interface.* 5:1173-1180.
22. Melchels F, Barradas A, Blitterswijk C, Boer J, Feijen J, Grijpma D, 2010. Effects of the architecture of tissue engineering scaffolds on cell seeding and culturing. *Acta Biomaterialia.* 6:4208-4217.
23. Roosa SM, Kemppainen JM, Moffitt EN, Krebsbach PH, Hollister SJ, 2010. The pore size of polycaprolactone scaffolds has limited influence on bone regeneration in an in vivo model. *J Biomed Mater Res A.* 92(1):359-368.

3. CONCLUSIONS

A significant improvement in the mechanical properties, ~85% increase in compressive strength, was measured when increasing the laser power and beam speed from 3W and 305 mm/s to 5W and 508 mm/s at a constant energy density of 1 cal/cm². The compressive strengths of the sintered scaffolds varied from 41 MPa for a scaffold with ~50% porosity to 157 MPa for a dense part. The compressive strength of the scaffolds after immersion in the simulated body fluid for 6 weeks decreased by 38% but was still higher than that of a human trabecular bone. The improved mechanical properties combined with the promising *in vitro* results show the high potential of scaffolds manufactured with 13-93 bioactive glass using the selective laser sintering process in load-bearing applications for bone repair.

Among the bioactive glass scaffolds fabricated with different architectures, the cubic pore architecture provides the highest compressive strength at lower porosities (< 40%). The effect of different architectures at higher porosities (> 65%) is not significant from a strength retention perspective for bone repair because all the scaffolds offer low compressive strengths, which are less than the lower range of the compressive strength of human trabecular bone. The simulated body fluid tests indicate that, for a same ratio of surface area to volume of the scaffold, the gyroid and diamond architectures have higher percentages of reduction in the compressive strength in comparison to the traditional lattice structures such as cubic because of their pore geometries which mimic trabecular bone. The results indicate that the SLS process could be used to fabricate scaffolds and control the rate of degradation by not only the selection of bioactive glass but also with

the choice of scaffold architecture. This demonstrates the potential of the SLS process for repair and regeneration of different regions of the bone.

The *in vitro* assessment indicates that bioactive glass scaffolds fabricated by the SLS process provide the necessary surface roughness for the initial phase of incubation for cell attachment. The results show the effectiveness of scaffolds with gyroid and diamond pore geometries in providing sustained cell proliferation for 6 days of incubation compared to other scaffold architectures (cubic, spherical, and X architectures) which did not provide significant cell growth after 4 days of incubation. The static cell culture experimental results and analysis indicate that a frequent change in the surface curvature of the scaffold combined with a higher surface curvature allows for improved cell proliferation *in vitro*.

The *in vivo* evaluation of the borate based 13-93B3 bioactive glass scaffolds with cubic and diamond pore geometries in a rat calvarial defect model for 6 weeks indicates potential of SLS scaffolds for bone repair. The bone growth in SLS scaffolds was comparable to that of the bone growth of thermally bonded short fiber scaffolds even with relatively large pores (~500-800 μm vs ~50-500 μm). Though there was no significant difference in the percentage of new bone formation with respect to the defect area (cubic-8.5% and diamond-9.5%), the presence of matured fibrous tissue within the diamond scaffold and absence of the same in the cubic scaffold indicates that provided an extended implantation time, diamond scaffolds could provide faster new bone formation.

4. RECOMMENDATIONS FOR FUTURE WORK

Further *in vivo* evaluation of the scaffolds with different pore geometries is required to collect more data on the effects of pore geometry on new bone formation. Long-term implantation (3 to 6 months) of bioactive glass scaffolds with different pore geometries with assessing bone growth at least two different time periods would provide a detailed bone growth profile for scaffolds with different pore geometries. This would establish an important aspect of selecting the appropriate architecture in treating bone repair and regeneration.

To date, there are several contradicting studies in the literature regarding the effects of pore shape especially when studies are coupled together with the pore size. The availability of the latest generation powder bed based laser sintering machines with higher resolution now makes it easier to fabricate scaffolds with specific pore sizes (~50 to ~300 μm) which was not feasible with the machine used in this study. Fabrication of scaffolds with different pore geometries at these pore sizes would also provide more data on cell proliferation and bone growth. Collection of such data would aid in finding new solutions for not only bone but also other tissue regeneration.

The addition of a small dose of BMP-2 to scaffolds with different pore geometries could be another possible approach to investigate the effectiveness of pore geometry on bone formation. BMP-2 is known to kick-start the bone formation and effect the initial phase of tissue growth. Therefore, investigation of bone formation would have another parameter $f(\text{new bone}) = f(\text{pore shape})$ would become $f(\text{new bone}) = f(\text{pore shape}, \text{BMP-2}, \text{pore shape} * \text{BMP-2})$.

The scaffold design in this study had non-conformal lattice structures. Conformal lattice structures as scaffolds for bone repair would be more beneficial during the *in vitro* and *in vivo* evaluation as conformity increases the permeability of the scaffold.

VITA

Krishna Chaitanya Reddy Kolan was born on September 29, 1983 in Hyderabad, Telangana, India. He received his B. Tech. degree in Mechanical Engineering from Jawaharlal Nehru Technological University, Hyderabad in 2006. After completing his Bachelor's, he worked as a Project Engineer in Engineering Design Services division of WIPRO Technologies Ltd, Hyderabad. Krishna joined the VRAM lab in fall 2008, and started working on bioactive glasses for bone repair in fall 2009. In 2011, he received his M.S. degree in Mechanical Engineering from Missouri S&T.

Krishna Kolan won the first place award for the paper entitled, "Selective laser sintering of bioglass bone scaffolds for tissue engineering" at the Intelligent Systems Center (ISC) Graduate Research Symposium on April 21, 2010 at S&T. He also received the first place award for his poster entitled, "Borate bioactive (13-93B3) glass scaffolds made by the selective laser sintering process" at the ISC Poster Presentation on November 19, 2013. His paper entitled, "In vitro assessment of laser sintered bioactive glass scaffolds with different pore geometries" was selected as one of the 12 best papers presented at the 25th International Annual Solid Freeform Fabrication Symposium held at Austin, TX, on August 13, 2014. He was presented with the Graduate Teaching Award from the Academy of Mechanical and Aerospace Engineers at S&T on October 9, 2014.

In September 2015, he received his Ph.D. under the guidance of Drs. Ming C. Leu and Gregory E. Hilmas in Mechanical Engineering from Missouri S&T, Rolla, Missouri, USA.